ULTRA-LOW POWER MICROBRIDGE GAS SENSOR

A Thesis
Presented to
The Academic Faculty

by

Ricardo Aguilar

In Partial Fulfillment
of the Requirements for the Degree
Master of Science in the
School of Mechanical Engineering

Georgia Institute of Technology
May, 2012

ULTRA-LOW POWER MICROBRIDGE GAS SENSOR

Approved by:

Dr. Peter Hesketh, Advisor
School of Mechanical Engineering
Georgia Institute of Technology

Dr. Todd Sulchek
School of Mechanical Engineering
Georgia Institute of Technology

Dr. Mostafa Ghiaasiaan
School of Mechanical Engineering
Georgia Institute of Technology

Date Approved: April 2nd, 2012

ACKNOWLEDGEMENTS

I owe this project and all the work that went into it to God first of all, as well as to several people, whose constant encouragement and support helped me in my research.

I will always be grateful to my advisor, Professor Peter Hesketh, who not only gave me the opportunity to broaden my knowledge base, pushed me when I needed to be pushed, and supported me in my graduate research and studies, but also was a good friend outside the academic setting. There is an abundance that I have learned from him; I couldn't have gone as far as I did in my research work if it wasn't for him. I am truly proud to have him as my advisor; I wouldn't have it any other way.

I would like to thank my colleagues in my research group for keeping me sane through those long hours and days in the lab and in the cleanroom. Not only did they keep the atmosphere a lively one, but they also challenged me on my project and asked the hard questions during the research meetings, which in turn helped me get further in my work. A special thanks goes out to Zhengchun Peng, for fabricating the original devices. Without his previous work, I would not have had such a wonderful project to work on as a graduate student.

I am also thankful to the MiRC cleanroom staff for proving guidance and advice when I was in dire need of it. Not only did they provide a learning and safe environment, they were also there whenever I had any questions pertaining to my work. Special thanks go to Eric Woods, Janet Cobb-Sullivan, Devin Brown and Caitlin Chapin for training me on the tools I needed for my process and for having the patience to deal with all of my questions. Also thanks to Gary Spinner for providing guidance, helping in expediting the

timetable for fixing the cleanroom tools and bringing them back up and for allowing us to grow the 10 μm of oxide needed for my wafers (which took 8 days). I am also indebted to Mikkel Thomas, who not only helped me tremendously on my process, but also acted as a pseudo advisor, always giving me advice both in and out of the cleanroom, pushing me to write and finish my thesis, and teaching me the "ways of the cleanroom". I've made a great friend in him, and for that I am truly thankful.

I want to thank Gary Hunter and NASA for providing the initial ideas and funding for this project. I also want to thank Joe Stetter, Mel Findlay, and KWJ Engineering for supporting the project both financially and intellectually.

I want to thank my friends and family for believing in me and cheering for me through all these years. I want to thank my parents especially for it is through them that all of this has been possible. I am truly blessed to have such supportive and loving parents; I thank God every day for them. Their love and support for me has led me this far, and I'm always forever grateful for that. I'd like to thank my brothers as well for bringing me back down to earth when it was needed, and well, for all the laughs which always lightened my mood when I was in need of it.

Lastly, I would like to thank my cat Jack for being such a great companion and keeping me company during those long nights by sleeping on my lap or on my bed while I worked, and also Amber Pizzo who was one of the main driving forces during my graduate career. She helped me as an undergraduate on my project and ever since then she has been there supporting me in what I do, both in and out of the lab. She has helped me stay focused on my work, and has been there with and for me through everything.

TABLE OF CONTENTS

LIST OF TABLES

LIST OF FIGURES

SUMMARY

This Thesis describes the fabrication, testing, and characterization of a miniature, ultra-low power, and sensitive, microbridge-based thermal conductivity gas sensor. The batch fabrication of the sensors was realized by CMOS compatible processes and surface micromachining techniques. Doped polysilicon was used as the structural material of the bridge with critical dimensions of 1 μm and 0.5 μm. These different size sensors have been tested with nitrogen, carbon dioxide, helium, hydrogen, and methane. Heat loss from constant voltage application was observed to be a function of the thermal conductivity of the gas ambient, resulting in different magnitude of resistance change. The response time of each of these sensors was found to be rather fast, while their stability was excellent. Finally, the results for the different sized microbridges were compared to show overall sensitivity, while having low power consumption.

CHAPTER 1

MOTIVATION AND INTRODUCTION

1.1 Motivation

The motivation for this Thesis originally came from the need for a small, low power gas sensor that could detect helium leaks in space stations. Even though this is a much focused application, the motivation to reach out to other kinds of applications with this project was evident from the very beginning. In fact, there is currently an increasing demand and variety of applications for miniaturized gas sensors. Because of this, many different types of gas sensors have been researched and developed over the years, a large amount of them using MEMS technology and micro fabrication techniques in order to become realized in the laboratory setting, and later in industry [1] [2].

Some of the more conventional gas detectors today include the widely utilized, relatively small pellistors. They are the most common form of microcalorimetric sensor which are used for the detection and estimation of flammable gases in air [3]. They work on the principle that by measuring the heat of combustion, detection of the gases is possible [4]. They typically require large power consumption (hundreds of milli-Watts to Watts) and have slow response time (tens of seconds). Advancement in microfabrication processing has led to pellistors which require lower power consumption than most, and are able to sense flammable gases such as butane and propane. These pellistors have been shown to safely sense within the lower explosion limit, requiring a power of about 49 mW, on the high side. Figure 1.1 shows an SEM image of the pellistor elements [5]. Furthermore, with MEMS technology, microhotplates have been built and are capable of reaching operating temperatures of 500°C in 20 ms at a power level of 100 mW [6].

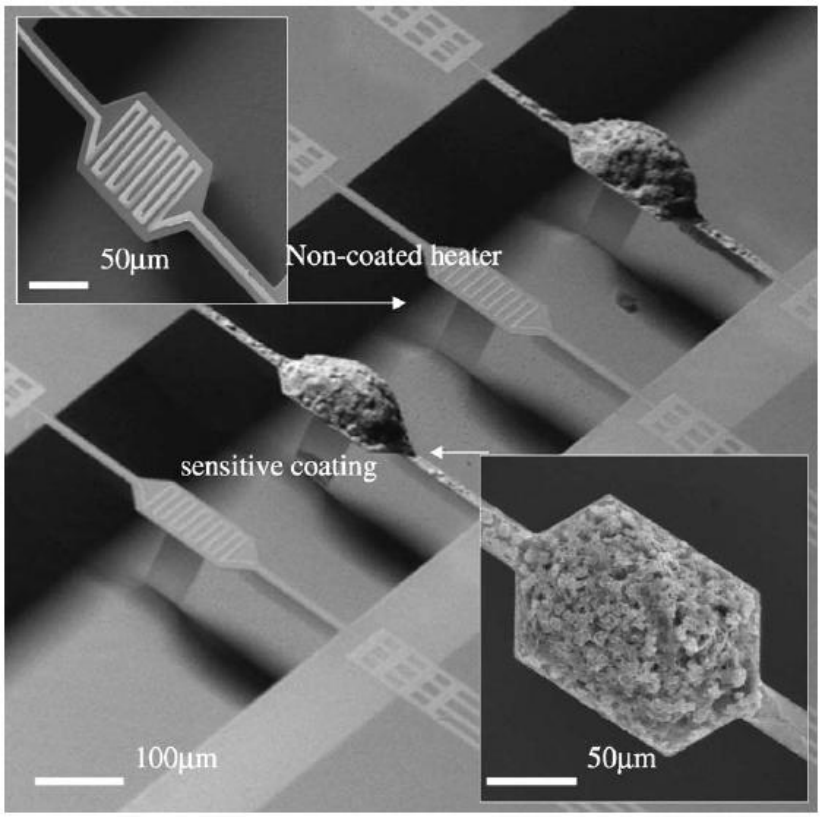

Figure 1.1: SEM image of pellistor elements with a gap of 60 to 80 µm

There is a growing interest in the development of sensors that have low power operation, along with low cost. Another type of sensors which tries to meet these goals is the family of metal oxide gas sensors, or MOX gas sensors. In industry today, current MOX gas sensors require a power consumption of 38-50 mW in order to reach the needed temperatures that activate the metal oxide sensing films [7]. Thus development of low power MOX sensors is an ongoing research area. One key advantage of these sensors is their selectivity to certain gases. The way the metal oxide films detect the target gas is through a chemical reaction which happens when the metal oxide film is hot enough and so it reacts with the gas present. Sensors have been developed and reported that can detect ammonia through the use of an indium tin oxide film [8] as well as the use of tin oxide nanorods [9]. Figure 1.2 shows an SEM image of a tin oxide gas sensor array, which displayed a power consumption of 15.5 mW for a 300°C operating temperature [10].

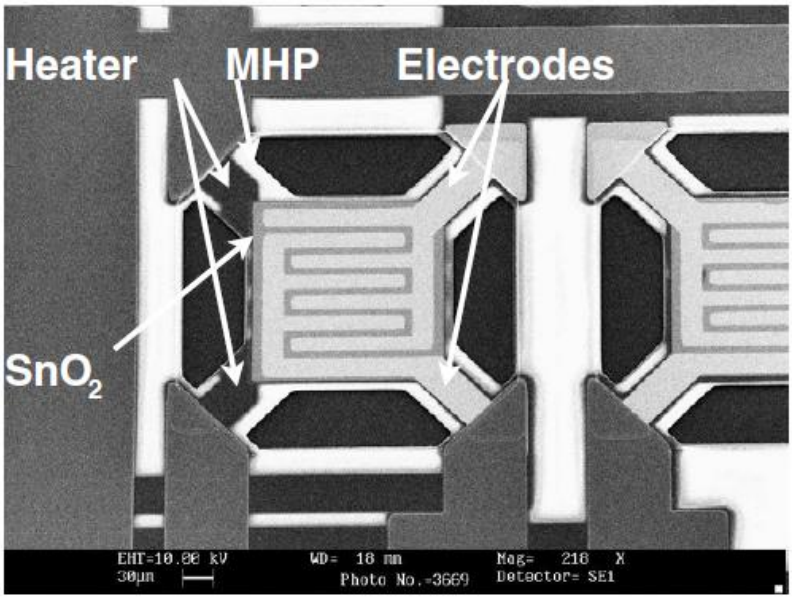

Figure 1.2: SEM of tin oxide gas sensor array where MHP denotes the microhotplate

As is evident, the field of gas sensing is not only wide ranged in terms of types of sensors, but it also poses many obstacles which need to be overcome. Low power, low cost, and fast time response are but a few of the many characteristics which all of these different types of gas sensors try to achieve and optimize. Yet there is another type of gas sensors which also focus on meeting the same criteria, as is further explored below.

1.2 Introduction to Thermal Conductivity Detectors

One set of gas sensors found today which are also being extensively studied are those which use the thermal conductivity of the gas in order to detect the gas composition. These are called thermal conductivity detectors, or TCD's. Such sensors are ideal for gas sensing due to the mechanical nature of the principle behind detection. Many types of TCD's have been fabricated with different sensing goals in mind. Hydrogen sensors have been reported which use the thermal conductivity of hydrogen in order to detect it within a mixture. These were used in conjunction with fuel cells in order to measure the hydrogen concentration. The sensors operate at temperatures

between 30°C and 90°C, having a response time of about 2 seconds [11]. Figure 1.3 shows a diagram of one such hydrogen sensor.

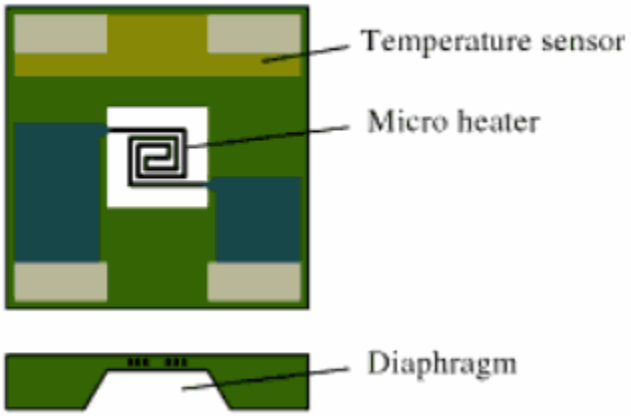

Figure 1.3: Diagram of hydrogen TCD

Microfabricated thermal resistive bridges used for catalyst heater and resistance thermometer have also been reported with 0.2 ms response time at even lower power level [12]. Compared with the calorimetric gas sensing principle used in the previous work, electrothermal sensing mechanism based on the thermal conductivity of gases does not rely on gas adsorption and reaction with catalyst films. Therefore, the response speed can be more rapid, and the sensor can be operated in a continuous manner and be repeatedly used without memory effect. Miniature thermal conductivity sensors have been developed for gas chromatography systems [13] and demonstrated for methane determination in natural gas [14]. Chemical sensor platforms based on thermal conductivity sensors have also been recently summarized [15] [16].

In this Thesis, the work focused on achieving ultra-low power microbridges gas sensors. In order to amplify the effect of gas thermal conductivity on heat loss from a heated bridge by increasing the surface-to-volume ratio of the sensing element, the thermal resistive microbridges were miniaturized in this work using MEMS technology. CMOS compatible technology, nanolithography, and polysilicon surface micromachining are some of the processes which were employed for the microbridge fabrication. As a

result, it was possible to lower the power consumption, shorten the response time, and enhance the sensitivity. Other groups have investigated nanoscale bridge type gas sensors using chemically synthesized carbon nanotubes [17], nanowires [18], and nanobelts [19], and a recent review by G. Di Francia *et al* [20] has been published. Although superior sensitivity was reported from these devices, using CMOS compatible batch fabrication processes allows highly reliable sensors to be inexpensively produced in volume.

1.3 Thermal Conductivity Detector Principle

Thermal conductivity gas sensors work on the principle that their resistance changes depending on the thermal conductivity of the target gas. When activated, the sensor is heated up, indicated by a certain resistance on the temperature sensor. Because of conduction however, the heat from the sensor dissipates out into the ambient, changing the temperature and hence the resistance. By keeping a constant power on the sensor, the heating effect is then kept constant. When another gas is introduced however, the heat from the sensor will dissipate at a different rate. This will produce a different temperature and change in resistance in the sensor from the previous gas. By taking the inherent resistance of the sensor and subtracting it from the resistance observed when the sensor is activated with a target gas present, the goal of gas sensing using the thermal conductivity of the gases is possible. The principle of a thermal conductivity detector was the driving force in the design of the microbridge gas sensor, which is the focus of this Thesis. Figure 1.4 shows a general schematic of what happens during operation of the microbridge.

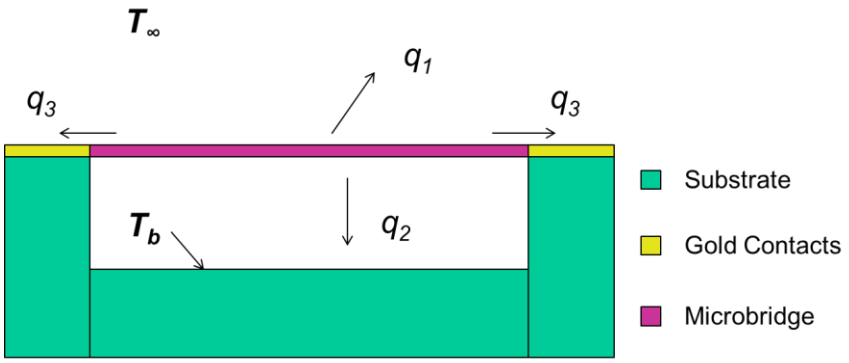

$$q_{tot} = \int q_1 + \int q_2 + 2q_3$$

Figure 1.4: General schematic of thermal conductivity microbridge gas sensor

The heat loss through the target gas is due to the thermal conductivity of the gas. This means that the heat dissipation will vary depending on what gas is present at the time. This is how the microbridge sensor works; it can "sense" what gas is present by the fact that the gas itself will induce a certain amount of heat loss from the microbridge, thus generating a certain resistance change that is only inherent of the said gas.

This Thesis will explore the ultra-low power microbridge in further detail. Several different microbridge designs are considered, both old and new, of six different geometries. The fabrication will be investigated, paying close attention to all the process steps, as well as all the complications and obstacles that were encountered during the actual fabrication. Testing on both the old and new sensors was conducted and is reported, including single gas, mixture, performance and selectivity testing of the sensors. Ending this Thesis is the discussion which considers all of the results and data reported. In the following chapters, the ultra-low power microbridge thermal conductivity gas sensor is fully explored.

CHAPTER 2

DESIGN, FABRICATION, AND PACKAGING

The original microbridge sensors which were used for the experiments described later were designed by KWJ Engineering and were fabricated in the Georgia Tech cleanroom in 2008. The original design had three different size microbridges: 100x2 µm, 50x1 µm, and 100x2 µm with a 50x1 µm center. Each die in this design was fabricated to have a total of 16 released microbridges. An extensive amount of experiments were conducted on these sensors, the majority of which were done on the 50x1 µm sensor. Thus, most of the data collected and presented in this thesis comes from experiments done on this sensor. Figure 2.1 shows an optical image of a typical die with 100x2 µm microbridges.

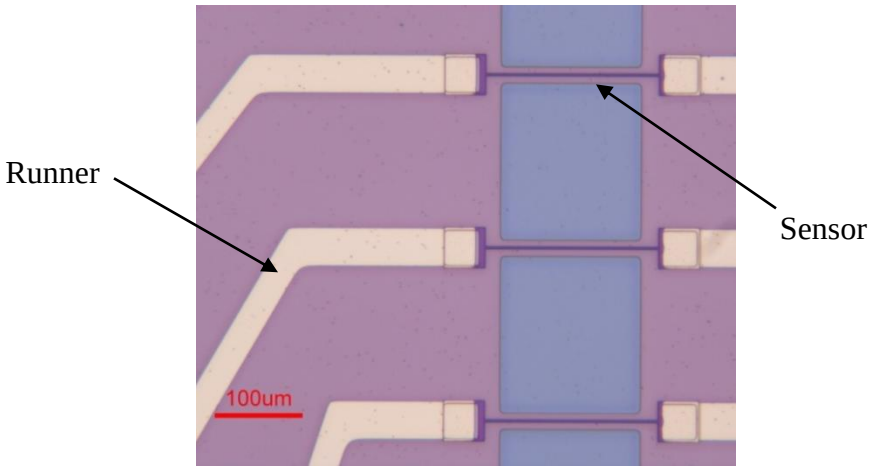

Figure 2.1: Original design; typical die with 100x2 µm microbridges

The design was later optimized, allowing for not only more sensitive sensors, but also making the use of different types of coatings for selective sensing possible. Several changes were made to the original design, including increasing the number of contact windows for the runners, switching from gold runners to platinum runners, and reducing the number of elements on one die by half. The fabrication process was also optimized in

order to increase the yield, making it possible to have a high number of sensing elements along with reference elements, which can later be used for a dynamic sensing system. In the later chapters, the optimized design will be addressed as the "new sensor", whereas the original design will be addressed as the "old sensor".

2.1 Design

In the optimized design, there are a total of six different designs which were fabricated. These designs not only vary in sizes but also vary in type of sensor. This design called for the first three dies to be used as thermal conductivity detectors, or TCDs. The last three dies were designed so that the microbridges act as heaters. These in turn work in conjunction with varying films which, after being deposited on the microbridges, are activated once they are heated. The films were chosen for their selectivity to specific gases; palladium was chosen for hydrogen sensing, while tin oxide was chosen for methane sensing. Figure 2.2a shows a schematic of a cross section of a microbridge which has been coated with either palladium or tin oxide.

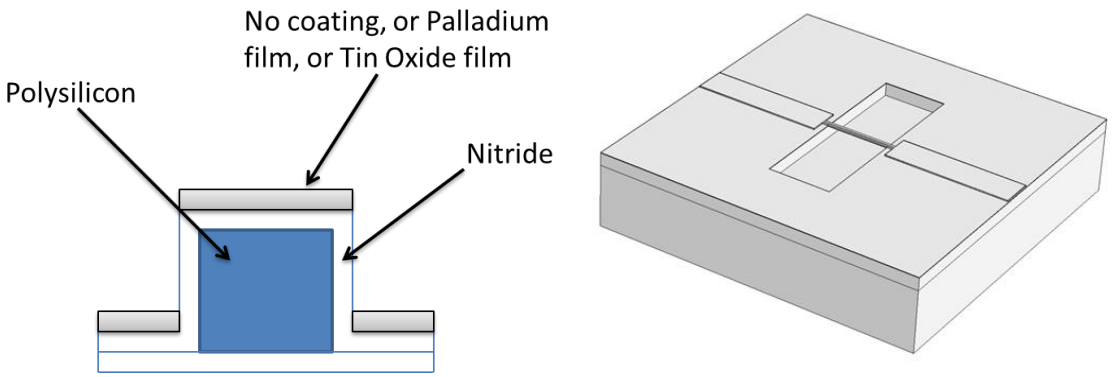

Figure 2.2: a) Schematic of a cross section of a typical microbridge; b) Schematic of a close up of a typical microbridge

As can be seen from Figure 2.2a, the nitride layer is much wider than the polysilicon element, creating "wings". This design characteristic is important since it is this wing which protects the polysilicon microbridge during the release step of the fabrication. All six dies were designed with the idea given by this schematic. The

microbridges were not the only polysilicon elements on each die; in fact the polysilicon was extended all the way from the microbridge, through the runners and into the bonding pads, as is portrayed by Figure 2.2b. This was done to eliminate the step of about 1 µm from the microbridge down to the nitride, thus making sure there is contact between the electrodes and the film to be deposited. Since the purpose of the polysilicon runners was to remove the step problem, these were designed to be 3 µm, whereas the actual platinum leads were designed to be 5 µm in width. A total of 3 different lengths of microbridges were built to study the effect of surface area. The 3 dimensions are as follows: 50x1 µm, 100x2 µm with a 50x1 µm center, and 50x1 µm with a 25x0.5 µm center. Three of the dies were designed as TCD sensors and three as heaters of the sensing films. A summary of all the dies in the optimized design is tabulated on Table 2.1.

Table 2.1: Optimized die designs

Die Number	Dimensions (µm)	Coating	No. of Sensors	No. of Extra Pt Leads per Element
1	50x1	None	4	0
2	100x2, 50x1 center	None	4	0
3	50x1, 25x0.5 center	None	4	0
4	50x1	Palladium/Tin Oxide	4	2
5	100x2, 50x1 center	Palladium/Tin Oxide	4	2
6	100x2, 50x1 center	Palladium/Tin Oxide	3	4

An example of what the final design of a die looks like is given in Figure 2.3, which shows a completed Die 1. From this figure, it can be observed that the die design includes a large polysilicon element which runs through the middle of the die. The purpose of this element is to act as a heater for the whole die, allowing for external

control of the substrate temperature. The dimensions of the die heater are that of 950x200 µm, and it's only found on the TCD dies, that is Dies 1, 2 and 3.

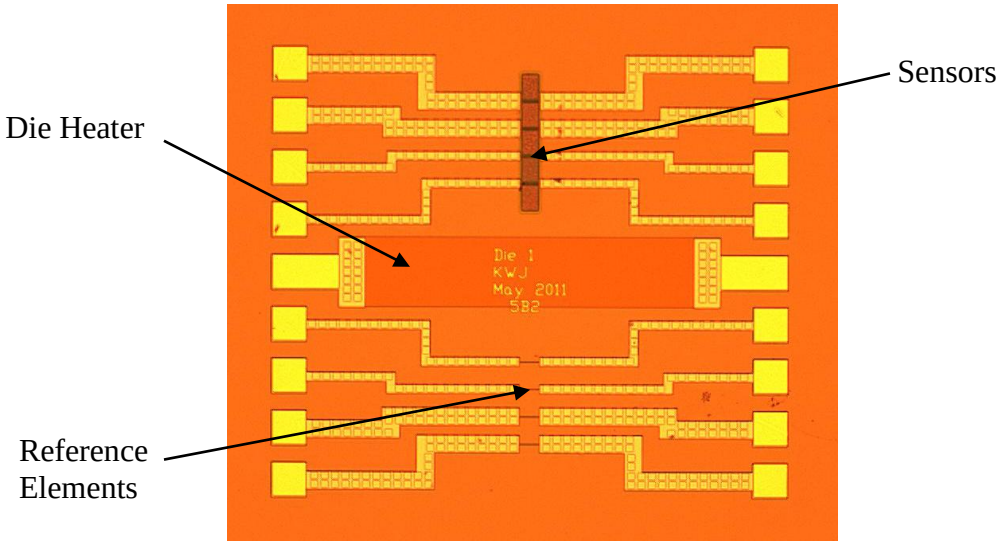

Figure 2.3: Final die design for Die 1

The first die in the new design is Die 1. It is composed of 8 elements of dimensions 50x1 µm. Four of these elements are released microbridges, while the other four are not released and thus act as reference resistance for the microbridges. The first two microbridges have twice the number of contact windows on the platinum runners than the last two microbridges, when looking from top to bottom. The die was designed this way with the goal of finding out if the number of contact windows had any effect on the sensor signal during testing. This design characteristic is also true for both Die 2 and 3. Die 2 is the next die in the design. It differs from Die 1 in that the dimensions of the elements are different, but it keeps all other aspects of the die the same. The dimensions of the elements found in Die 2 are 100x2 µm with a 50x1 µm center. The same holds true for Die 3, in that the only aspect of the die that differs from the first two dies in the design is the dimensions of the elements. These dimensions are 50x1 µm with a 25x0.5 µm center, making these elements the smallest of the designs. The fabricated Dies 1, 2 and 3 are shown in Figure 2.4. These three dies were designed as TCDs.

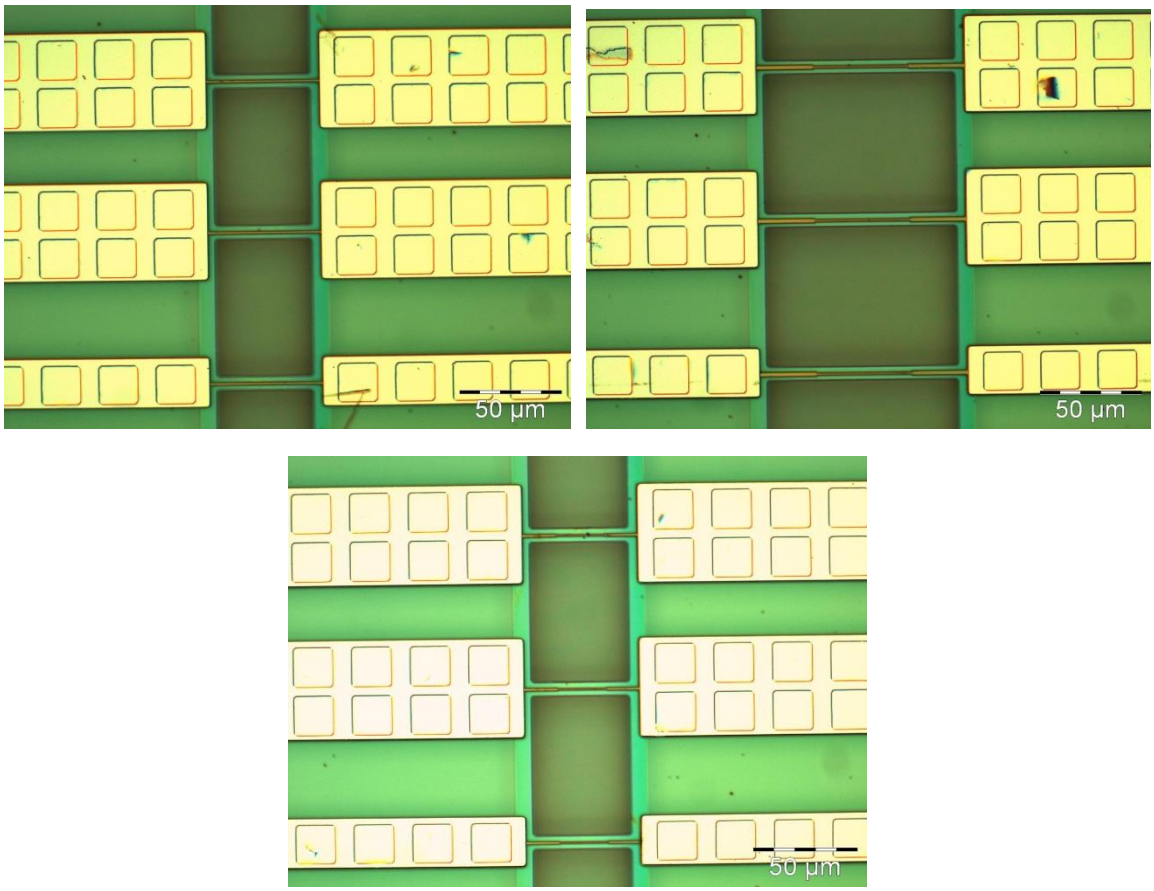

Figure 2.4: a) Die 1 – 50x1 µm; b) Die 2 – 100x2 µm with 50x1 µm center; c) Die 3 – 50x1 µm with 25x0.5 µm center

The last three dies were designed to be heaters which can provide a constant heat source to the film coating which acts as the sensing element. Die 4 is composed of 8 elements of dimensions 50x1 µm. Like Die 1, four of these elements are released microbridges, while the other four are not released and act as reference resistance to the microbridges. Die 4 differs from Die 1 in that it has a second pair of platinum leads for each element found on the die. This second set of platinum leads sits on top of the nitride and does not make contact with the polysilicon underneath; instead the purpose of the leads is for the measurement of resistance of the sensing film coating on top of the microbridges. This second set of platinum leads run cover each microbridge, but do not connect (except for only one set), and from there run back to bonding pads, separate from the ones that are connected to the microbridges themselves. The palladium and/or tin

oxide when deposited on the microbridges makes contact with the separated platinum leads, thus closing the circuit and allowing for testing and characterization. Die 5 is the next die in the design. It differs from Die 4 in that the dimensions of the elements are different, but it keeps all other aspects of the die the same. The dimensions of the elements found in Die 2 are 100x2 μm with a 50x1 μm center. The last die in the design, Die 6, is the most complicated die from the six. This die is composed of a total of 6 elements of dimensions 100x2 μm with a 50x1 μm center. Three of these elements are released microbridges, while the other three are not released and act as reference to the microbridges. Die 6 differs from Dies 4 and 5 in that instead of having one pair of platinum leads per element, Die 6 was designed with two pair of platinum leads per element. The idea behind having four platinum leads per element is to create a four point probe to measure the resistance of the film coating. The ability to measure the current and the voltage running through the film coating allows for a much more accurate reading of the resistance and resistance change found in that specific coating. Since each element required a total of 6 platinum leads (2 for the microbridge, 4 for the four point probe), Die 6 could only be designed to have a total of 6 elements because of space constraints. The fabricated Dies 4, 5 and 6 are shown in Figure 2.5.

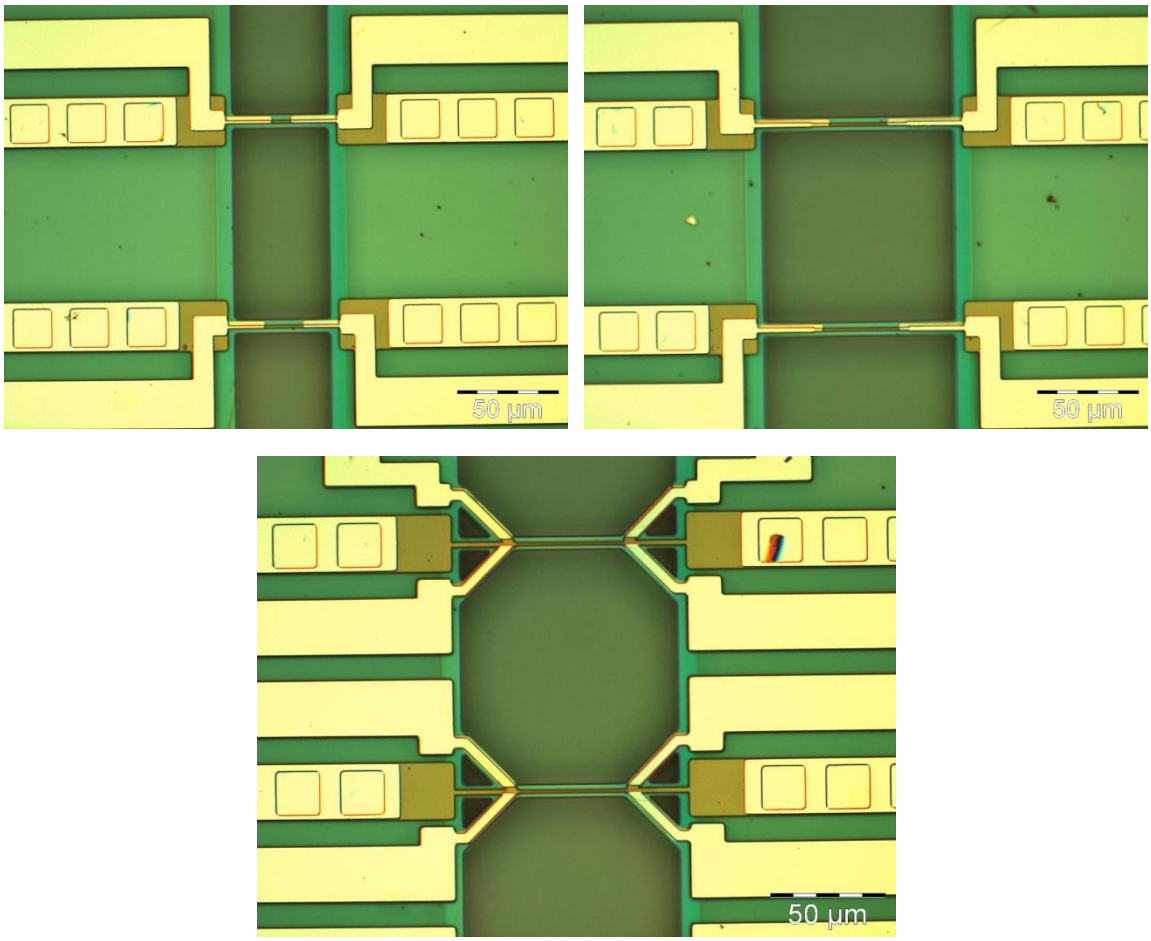

Figure 2.5: a) Die 4 – 2 point, 50x1 µm; b) Die 5 – 2 point, 100x2 µm with 50x1 µm center; c) Die 6 – 4 point, 100x2 µm with 50x1 µm

2.2 Fabrication

The optimized fabrication process in total is composed of 35 steps, which not only includes the physical fabrication of the microbridges, but also the preparation and packaging of the dies to be tested and characterized.

2.2.1 Etching, Metallization, and Release

The fabrication process began by taking a <100> silicon wafer and growing a 10 µm layer of silicon dioxide, SiO_2, on the surface of the wafer (step 1). The layer was thermally grown in a furnace at a temperature of 1100°C over the course of a week, allowing for a high quality SiO_2 film. A Nanospec refractometer was used to measure

and confirm the thickness of the SiO_2 film. This thick layer of SiO_2 was used as both the anchoring material to suspend the bridges as well as the sacrificial layer to be removed to form the suspended bridges later on. Next, a thin, low stress nitride layer of around 0.2 µm was deposited by a low pressure chemical vapor deposition (LPCVD) furnace (step 2). The parameters of the deposition were as follows: 100 sccm of dichlorosilane and 17 sccm of ammonia, at a temperature of 835°C. The nitride deposition was done it two steps, that is a 0.1 µm layer was deposited on top of the oxide layer, followed by a second 0.1 µm layer of nitride, with each layer taking 20 minutes to deposit onto the wafer. This was done in order to reduce the number of pinholes that may occur in the film during the deposition process. Having the film deposited in two steps makes it so that the second half of the film is not the same as the first; that is, it won't have the same types of defects as the first, thus reducing the chance of pinholes on the film. Figure 2.6 shows an example of what a pinhole defect looks like when found on a film, in this case an oxide film [21]. Even though the size of a single pinhole may be small when compared to the dimensions of the sensor and die designs, it can still affect the performance of the overall sensor depending on where it may be located on the film. The two step nitride deposition is used throughout the fabrication process for this purpose.

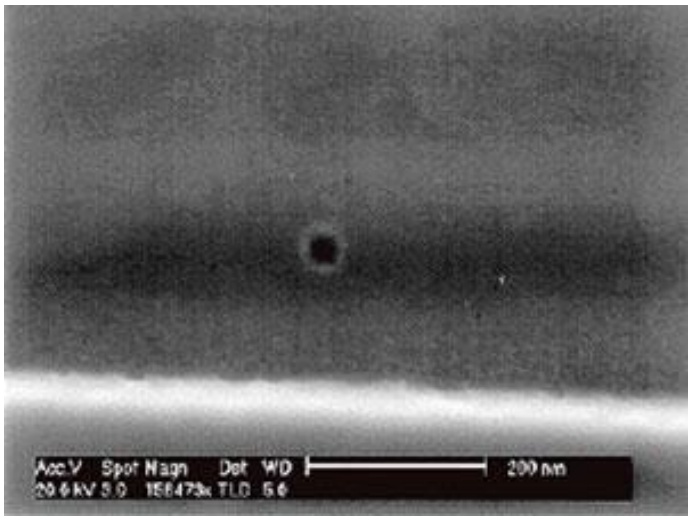

Figure 2.6: SEM of pinhole defect found on an oxide film

The purpose of the nitride layer is to act as a protection layer during the removal of the SiO_2 sacrificial layer. Once the nitride was deposited on the wafer, the next step was to do a polysilicon deposition, with a desired thickness of about 1 μm (step 3). The polysilicon serves as the sensing layer, which is what the sensors are composed of. It was deposited using an LPCVD furnace, with 100 sccm of silane, at a temperature of 588°C and a pressure of 250 mTorr for 3 hours. In order for the polysilicon layer to act as a sensing layer however, it needed to be doped with boron. This creates an abundance of holes in the polysilicon crystal lattice, which leads to electrons moving into fill these holes. The film is electrically neutral unless it is thermally excited, which is the case when applying a voltage bias, thus allowing for the polysilicon layer to become useful as a sensing layer. The p-type doping of the polysilicon layer was carried out by using a boron source at 1050°C, 200 sccm of oxygen, and 5000 sccm of nitrogen for 2 hours, followed by drive-in process at the same parameters for 1 hour. The drive-in step is done in order to allow for the dopant to completely diffuse through the entirety of the polysilicon thickness. This doping/drive-in process does form a thin oxide film on the wafer due to the use of oxygen during the process. In order to proceed with the fabrication, the wafer had to be placed in a buffered oxide etch (BOE) bath in order to remove the thin oxide layer from the wafer, as this film can act as an insulator, preventing the p-type doped polysilicon from the ability to make electrical contact.

Two methods were used in order to check the resistivity of the polysilicon layer after the doping process. The first was to conduct a four point probe measurement on the film after the BOE step to remove the native oxide. Table 2.2 lists an array of measurements which were done on several of the wafers that had been doped and were later used during the fabrication process. As can be seen, the resistivity values varied from wafer to wafer; it was found to be caused by the boron sources being too old and thus not doping the wafers with the right concentration. The expected resistivity value in order for the polysilicon to behave as a sensing film was that of around $1x10^{-3}$ to $2x10^{-3}$

Ω-cm. To check that the four point probe measurements were indeed correct, a doped wafer was sent to Solecon Laboratories in Nevada for an analysis of the concentration profile and the resistivity profile of the doped polysilicon using new boron sources. The company did so by cutting the wafer and making measurements on the cross section of the polysilicon, thus obtaining concentration and resistivity values as a function of the depth within the film. Their findings, which are found in Appendix A, coincided with the four point probe measurements and the expected resistivity values.

Table 2.2: Resistivity values for various wafers after boron doping

Wafer Number	Top $x10^{-3}$ Ω-cm	Bottom $x10^{-3}$ Ω-cm	Center $x10^{-3}$ Ω-cm	Left $x10^{-3}$ Ω-cm	Right $x10^{-3}$ Ω-cm
1	3.4410	4.0972	3.2316	4.1564	3.6714
2	2.2146	2.5395	1.9981	2.6761	2.2190
3	2.4464	2.4752	2.3120	2.4195	2.6883
4	1.9497	2.3098	2.0366	2.1296	2.5611
5	1.7507	1.9921	2.1738	2.0815	1.6984
6	1.8704	1.9827	2.3660	2.0649	1.7037
7	1.6376	2.0490	1.9009	2.0155	1.7141
8	4.8146	6.3169	4.8002	6.3640	6.3054
9	4.8966	4.9519	4.3056	3.7605	6.6428
10	1.9547	1.9558	1.8397	1.9510	2.0225
11	1.8343	2.0430	1.8187	1.8832	2.0641
12	1.9160	1.8129	1.7884	2.0057	1.7945
13	2.1343	2.2271	2.0415	2.2318	2.1731
14	1.9361	1.9723	1.8018	1.9647	1.8735

Once the oxide film was removed, the next step was to etch the initial alignment marks into the polysilicon film. These were used to align the subsequent masks, including the electron beam lithography (EBL) system. This was done first by patterning the initial alignment marks on to the wafer using a 1 μm thick film of the negative photoresist Futurrex NR9-1500PY, and then followed by an inductively coupled plasma (ICP) etch. The process that was used in the ICP was the Bosch process, as seen in Figure 2.7. As is shown in Figure 2.7, the Bosch process etches polysilicon in a cyclic matter, by alternating the etching step and the passivation step [22]. For the etching of the alignment marks, a total of 7 cycles was needed in order to etch the 1 μm of polysilicon which was exposed.

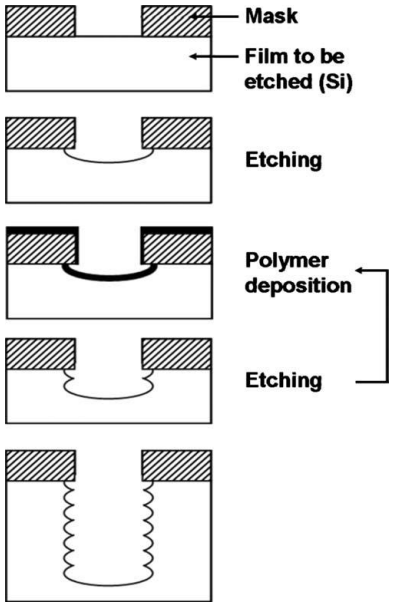

Figure 2.7: Schematic of the steps involved in the Bosch process

Once the alignment marks were etched, the wafer had to be prepared for the patterning of the microbridges and the etching that follows. The patterning of the microbridges was done using a technique called double exposure, in which a combination of EBL and Deep UV was utilized. This was a very crucial step in the fabrication process, posing several obstacles that had to be overcome in order for the success of the sensor fabrication. Due to the magnitude of work and research that went into

characterizing this step, it is further explained in detail in the next section. After the polysilicon layer was patterned using the double exposure technique, it was etched in an ICP etch using again the Bosch process (step 4). The etched polysilicon wafer was then cleaned using a Piranha solution, which consists of a 3:1 ratio of sulfuric acid to hydrogen peroxide solution which is heated with a heater set to a temperature of 120°C. This solution was used when the wafer needed deep cleaning, but always before any metallization was done to it. After the deep cleaning, the wafer was placed in the furnace for the deposition of another LPCVD nitride layer (step 5). This layer was done the same way as the first layer, in two steps with each step depositing about 0.1 μm. As previously explained, this was done in order to reduce the opportunity for pinhole defects to occur. Depositing the two layers of nitride between the polysilicon film was done in order to sandwich the polysilicon microbridges. The sandwiched structure is necessary to protect the polysilicon material from being attacked from the side by oxide etch during the beam release step which happens later on. However, it also acts as an insulating coating for the final product, ensuring that each sensor is isolated from all others.

At this point, the wafer was then prepared for metallization steps, in which the runners and bonding pads to the sensors were defined. In order to have the runners make contact with the sensing element, it was necessary to open windows on the nitride layer. This allows for the metal from the runners to make direct contact with the polysilicon underneath. The windows were first patterned on the wafer using a 1 μm thick film of the negative photoresist NR9-1500PY, and then opened using a reactive ion etch (RIE) step, which was run for a total of 6 minutes (step 6). The conditions in the RIE step were as follows: 15 sccm of fluoroform (CHF_3) and 5 sccm of oxygen, at a power of 270 W and a pressure of 47 mTorr. With the windows open, the metal could be deposited on the wafer in order to define the runners. The runners were patterned using the NR9-1500PY once again, and the wafer was placed in the electron beam evaporator system. Two different metals were evaporated on to the wafer: 30 nm of chromium at a rate of 0.5

Å/sec were evaporated first to act as an adhesive layer, followed by 250 nm of platinum at a rate of 1 Å/sec, which act as the electrical runners (step 7). Titanium could have been used as the adhesive layer for the metallization steps in the fabrication process, but chromium was preferable due to its resistance to BOE, which is used later for the release of the microbridges. After the evaporation of the platinum, the wafer was left in an acetone bath for an overnight liftoff. It was then cleaned off with acetone, methanol, and isopropanol, and inspected to make sure there was no residue left on the wafer. The same process was followed for the bonding pads, which were defined through a gold evaporation. The bonding pads were patterned using a 2 μm thick film of NR9-1500PY and gold was evaporated as follows: 30 nm of chromium at a rate of 0.5 Å/sec, after which 450 nm of gold at a rate of 2 Å/sec were deposited.

After the gold liftoff, the wafer was prepared for the last few steps of the fabrication process which release the microbridges. This is where the sacrificial SiO_2 layer comes into play, since its removal is what releases the elements forming suspended microbridges. In order to get to this layer however the nitride on top of it had to be removed. First, etch windows in alignment with the polysilicon elements were opened using a 2 μm thick film of NR9-1500PY for the pattern. The nitride layer was then etched using the same RIE step used earlier for opening up the contact windows, only difference being that it was used for a period of 12 minutes in order to etch the full thickness of 0.4 μm (step 8). Originally for this step only 1 μm of NR9-1500PY was spun on the wafer. This proved to be problematic in two ways: the film was too thin for the varying topography found on the wafer up to this point, making it difficult to obtain accurate alignment, as well as providing minimal protection to the smallest features found on the wafer, in this case the polysilicon elements. Figure 2.8 shows a result of using a 1 μm thick film of NR9-1500PY for this step. As can be seen from the figure, the polysilicon elements were attacked by the RIE plasma, which means the photoresist was too thin at those locations on the wafer.

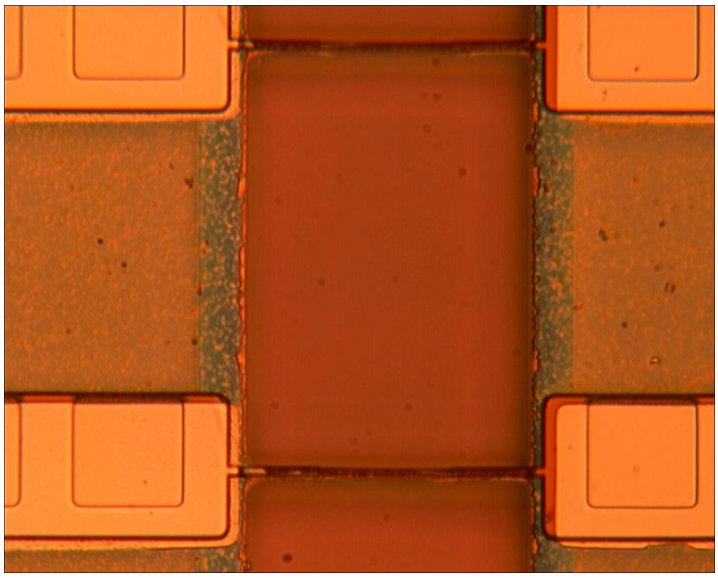

Figure 2.8: Damage to polysilicon elements due to RIE plasma

After the RIE step, the wafer was cleaned in order to remove the photoresist mask, at which point it was ready for the wet etch of oxide. A BOE solution was prepared with a 6:1 volume ratio of 40% NH_4F (ammonium fluoride) in water to 49% HF (hydrofluoric acid) in water, and the wafer was placed in the bath for a period of 30 minutes, agitating the container gently every so often. The agitation is needed so that the surface of the wafer is always in contact with fresh etchant. The rate at which BOE etches oxide is that of about 1 μm every 10 minutes, in theory; this meant that in order to etch at least 9 μm from the 10 μm of oxide layer, the wafer had to be placed in BOE for a total of about 90 minutes. The 90 minutes were divided into three steps of 30 minutes, to ensure maximum etching of the oxide (step 9). The reasoning behind using BOE is that it etches oxide in an isotropic manner, meaning that it etches vertically at the same rate as it etches horizontally. This type of etch was preferred over a dry etch process, namely an RIE process, since it is needed for the oxide to etch horizontally as much as possible in order to release the microbridges, and thus forming the sensors. Figure 2.9 shows a simplified schematic summarizing the steps that were taken in order to fabricate the microbridge sensors. Shown in the schematic are numbered steps, which correspond to

the steps laid out in the fabrication process explained above. A table listing each of the tools used in the fabrication of the microbridges can be found in Appendix A, Table A.1.

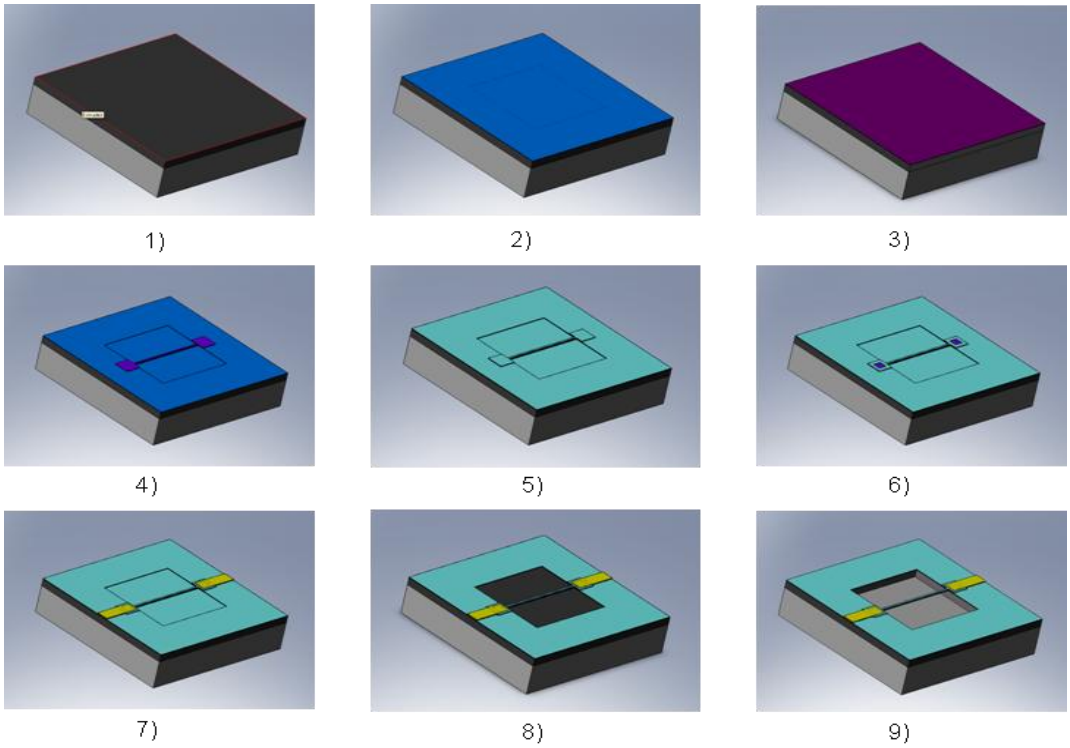

Figure 2.9: Schematic of the fabrication procedure for the microbridges

After the release of the microbridges, the wafer was prepared for dicing. Dicing allows for each individual die to be separated from the wafer and used on its own as a sensor, once packaged. Before the dicing the wafer however, the wafer had to be coated with photoresist in order to protect the released bridges during the dicing process. The photoresist Shipley S1813 was used to coat the wafer; it's important to note that the resist was not spun, but rather it was poured on to the wafer using a pipette, and the excess was removed, leaving a film of about 0.5 cm thick. The thick resist coating allowed for less stress to be found at the bridge's location once the resist hardened after the hard bake. After the wafer was coated, it was placed in an oven at 120°C for 10 minutes to make sure the resist hardened, making it stay on the wafer. After the coating step, the wafer was sent to be diced into quarters. The dicing tool that was used was the ADT 7100 which has 100 µm nickel blades.

The quarters were then cleaned using acetone to remove the photoresist. Each quarter was aligned to the last mask, the shadow mask, which allowed for the evaporation and/or sputtering of palladium and tin oxide, respectively. The shadow mask, purchased at Photo Sciences Inc., consists of windows which open up only to the microbridges that are to be coated. Through this procedure, only the last three die designs were coated with either film, leaving the first three dies to still act as TCDs. Figure 2.10 shows optical images of the shadow mask windows for each corresponding die. Figure 2.11 shows an SEM image of a 50x1 μm microbridge with a palladium coating on it.

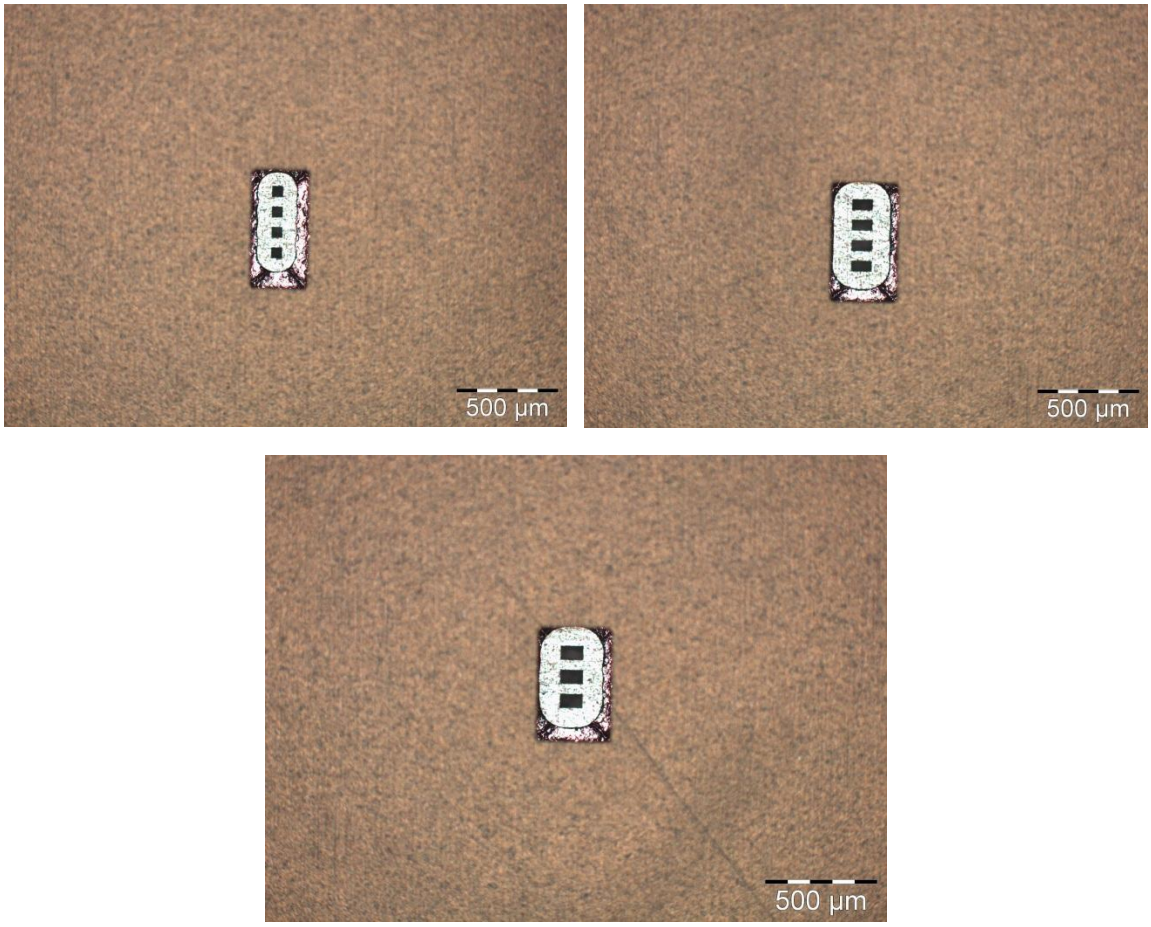

Figure 2.10: Shadow mask windows – a) Die 4; b) Die 5; c) Die 6

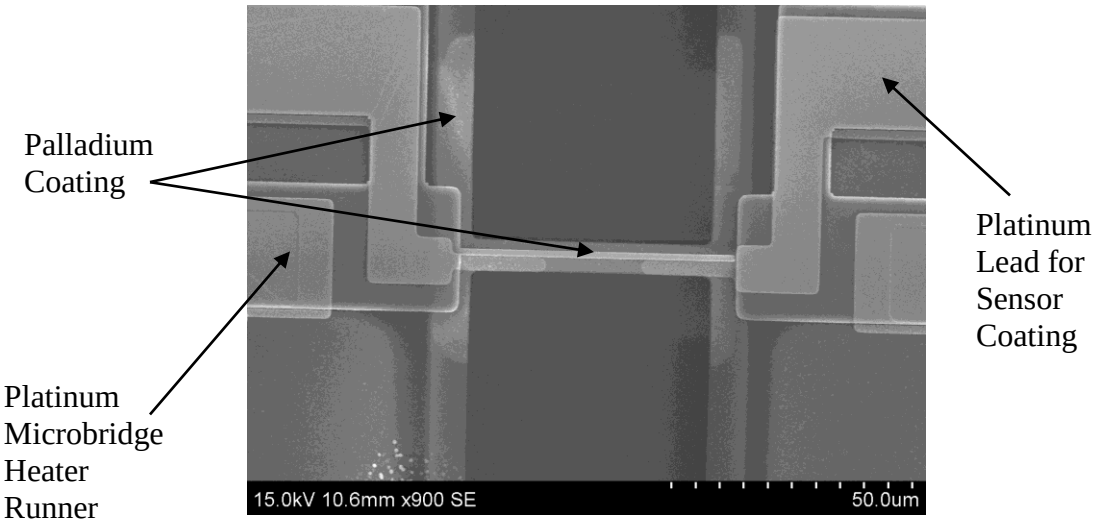

Figure 2.11: SEM image of palladium coated microbridge

After the quarters were coated with their corresponding films, they were once again coated with S1813 and diced into the individual dies. After dicing, the dies that were needed for the experiments to follow were cleaned of the photoresist using acetone. These dies were then wire-bonded to an IC package for use as gas sensors. A wedge bonder from Marpet Enterprises Inc. was used to wire bond the dies, with .0015" thick aluminum wires. Each sensor consists of an array of 8 elements, 4 of which are released microbridges, while the other 4 are the reference elements. An SEM image of the released microbridge is shown in Figure 2.12a; the distance between the microbridge and the bottom of the trench is about 7 μm after the BOE etch. The IC package shown in Figure 2.12b has a total of 16 pins; other IC packages were considered with varying number of pins, all depending on the type of set up and die sensor configuration for the given die.

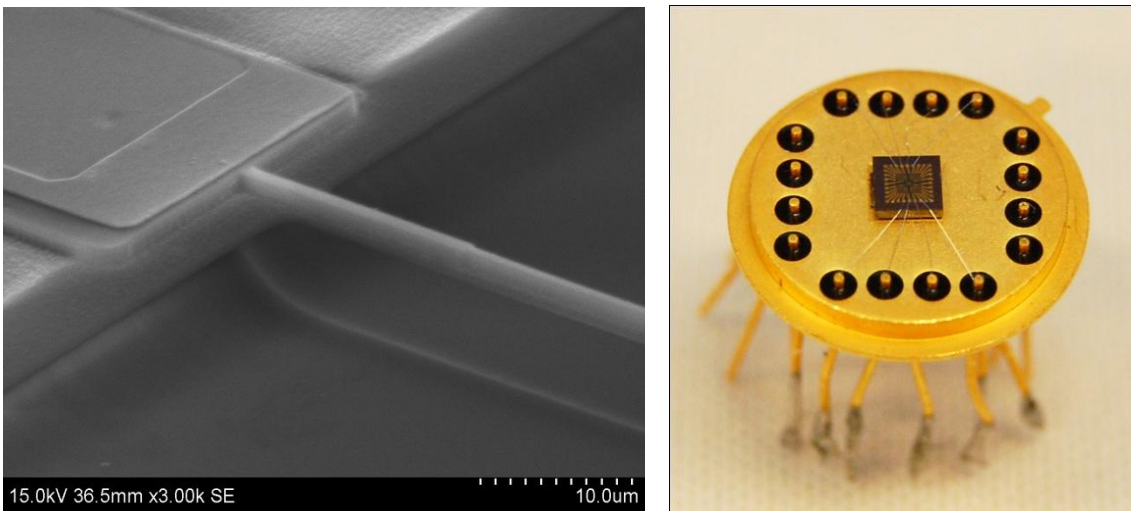

Figure 2.12: a) SEM image of released microbridge; b) Picture of a packaged sensor

2.2.2 Electron Beam Lithography

The first critical step in the fabrication process of the microbridges is the double exposure, as was mentioned in the above section. The double exposure consists of writing a small feature pattern onto the photoresist using electron beam lithography, and then later exposing the bigger feature pattern onto the same photoresist using Deep UV light. The advantage of using such a procedure is that it cuts down on the time it takes to write the pattern on the electron beam lithography system, while allowing for much bigger features to be patterned on the same process step, resulting in a much more complex pattern containing a range of feature sizes.

The double exposure method requires that the resist to be used be a CAR, a chemically amplified resist, since not only can it be exposed through a deep ultraviolet source (DUV), but it also is compatible with EBL, which allows for the patterning of the same level, that is on the same resist layer [23]. This is how the double exposure method works, by exposing the pattern using the electron beam and the deep ultraviolet separately but into the same resist layer [24]. After the resist is spun, the EBL is used to write the submicron features on the resist. The wafer is then taken to the DUV lithography system and the mask which contains the larger features is used to expose the

rest of the pattern onto the same resist. The wafer is then developed, leaving the complex pattern of submicron features with large features. Using this technique combines the high-resolution capabilities of the EBL system, along with the high throughput of the DUV lithography system [25]. These are not the only advantages though; since the pattern to be written on the EBL system is less complex, with much less features, the writing time decreases, which in turn also reduces the overall cost. Figure 2.13 shows an SEM image of a test double exposure using a CAR as the resist layer [26]. As can be seen, both of the features, the one exposed in the DUV and the one written using EBL, come out to be almost identical.

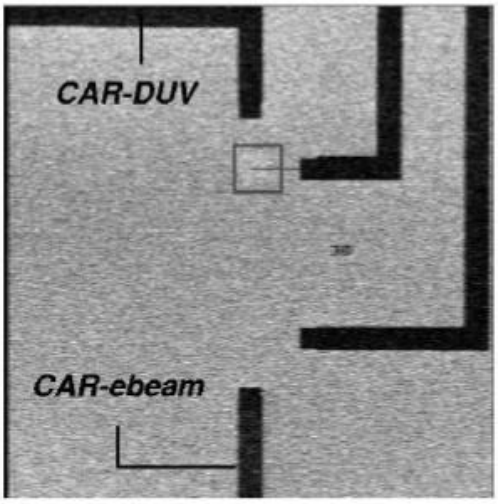

Figure 2.13: SEM image showing the double exposure method

For the fabrication of the microbridges, the photoresist that was used for the double exposure was the negative tone EBL resist ma-N2403. This resist not only allows for high pattern resolution, like other EBL resists, but it also is versatile, as it has been found that it can be used in the double exposure method. It is after all a chemically amplified resist, in that it does have high sensitivity to both the exposure dose of the EBL and the exposure energy of the DUV lithography system. Indeed it is sensitive only to the deep ultraviolet side of the light spectrum, as is shown on Figure 2.14 [27]. One can

see from this graph that the range of wavelength at which the resist will be successfully exposed is from 248 to 254 nm.

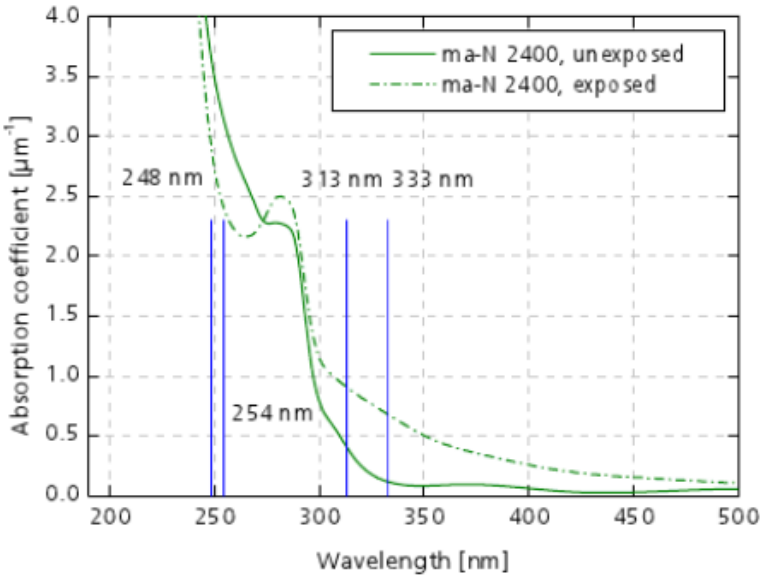

Figure 2.14: UV absorption of ma-N2403 resist

Since it was found that ma-N2403 can be used with both EBL and DUV systems, it was chosen to be used for the purpose of fabricating the microbridges using the double exposure technique. The first step was to run different dose tests of the resist in the EBL system, in order to determine which dose not only gave the desired line width, but also produced features with high resolution. Figure 2.15 shows SEM pictures of different dose tests that were conducted using ma-N2403. Ultimately a dose of 290 mC/cm^2 was found to be the best dose for the purposes of this study.

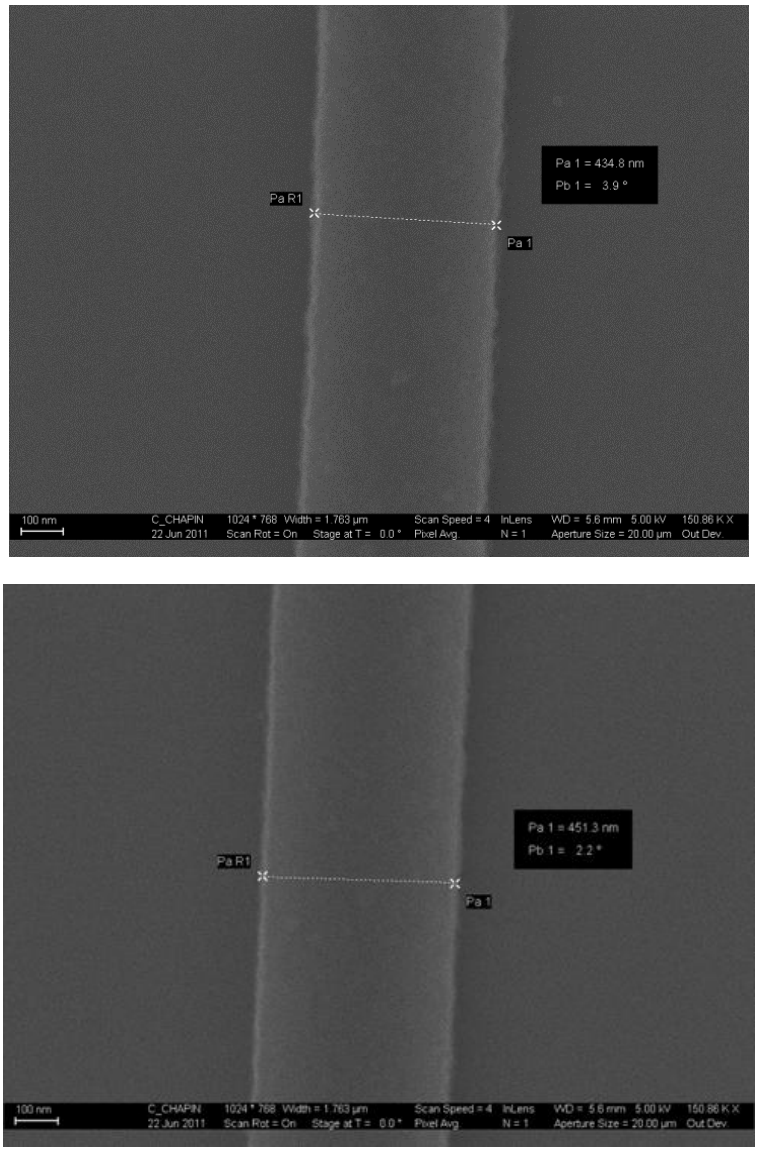

Figure 2.15: Desired line width 500 nm; a) dose of 250 mC/cm^2, producing a line width of about 434 nm; b) dose of 270 mC/cm^2, producing a line width of about 451 nm

After finding the correct dose for the EBL system, the pattern which only included the microbridges was uploaded to the EBL computer system. In order to carry out the actual double exposure, the wafer had to be prepared with some initial alignment marks so that the EBL and the DUV system could both use these marks to align to, making the process a possibility. The process by which these alignment marks were made on wafer was discussed in the above section. Figure 2.16 shows an optical image of the initial alignment mark after a test platinum deposition run.

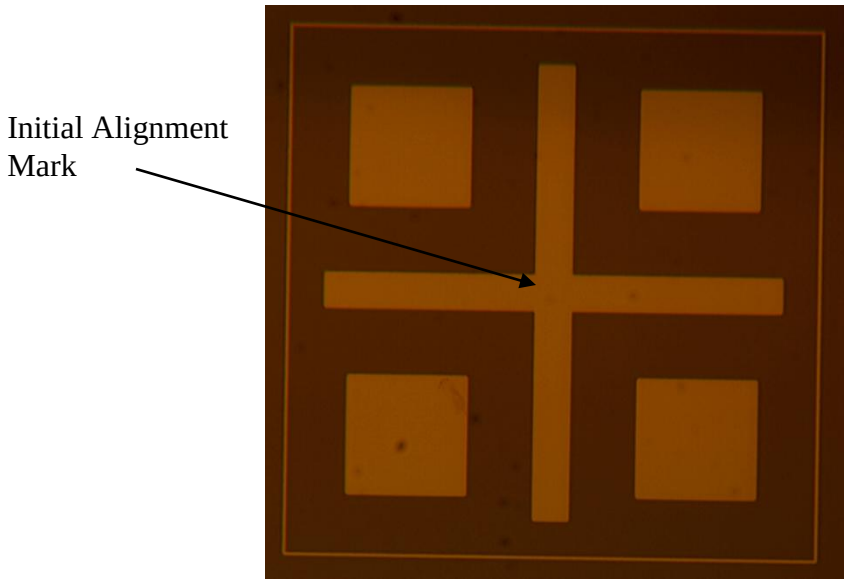

Figure 2.16: Initial alignment mark after platinum deposition

The pattern was written onto the resist on the wafer, taking about an hour per wafer to complete. The wafer was then taken to the DUV mask aligner, where the wafer was aligned to the marks on the mask and once again exposed, completing the double exposure of the same resist layer. Since ma-N2403 is a negative tone resist, a dark field mask had to be used for the DUV part of the double exposure. The dose that was used to calculate the time that was required for the resist to be exposed to the DUV light source was that of 550 mJ/cm^2. This number was obtained through testing of a range of doses in order to get the right dose which would allow for a development time of 70 seconds. After development of the pattern, the wafer was rinsed in DI water for a minute and half to remove any residual developer from the surface of the wafer. It was then inspected under an optical microscope to evaluate the quality of the final resist mask. Figure 2.17 shows an optical image of one of the microbridges which was obtained through the double exposure method. As can be seen, after much testing, the technique was a success and the combination of submicron features with large features on the same resist layer with minimal cost in terms of money and time was obtained. The leads shown are 25 μm

wide, whereas the area in the center of the microbridge, the submicron feature in this case, is 500 nm wide.

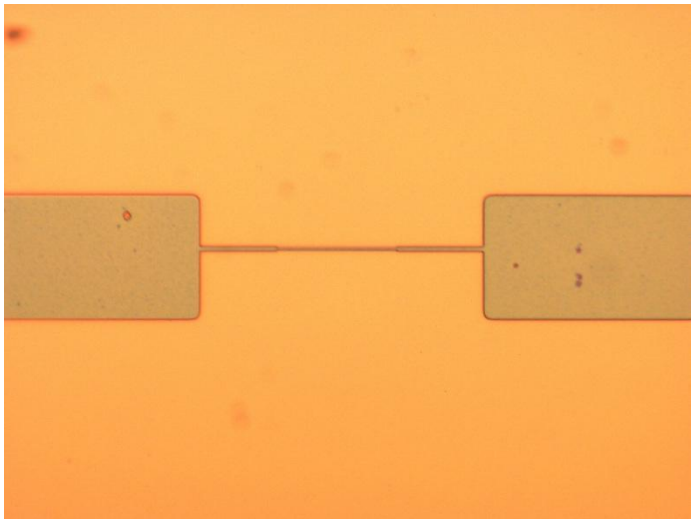

Figure 2.17: Microbridge pattern using ma-N2403 with the double exposure method

The double exposure technique did pose several obstacles and problems which were encountered during fabrication. One of the very first problems dealt with the resist not absorbing the deep ultraviolet light. Initially it was thought that perhaps the resist was too old or perhaps even expired, limiting the amount of light it could actually absorb. To this end, the time of exposure was increased exponentially, not only on the old resist, but also on a fresh batch of resist, to no avail. It was later found that the mask being used was made of Soda Lime, which absorbs about 90% of the light with wavelengths in the DUV region. The mask was then changed to a Quartz mask, which does allow DUV wavelengths to pass through.

The biggest and most pressing problem was one that occurred several times during and after the development process. It was found that during the development step and the rinsing step afterwards, a big portion of the pattern was being removed. Figure 2.18 shows an optical image of what in general was happening during the development process.

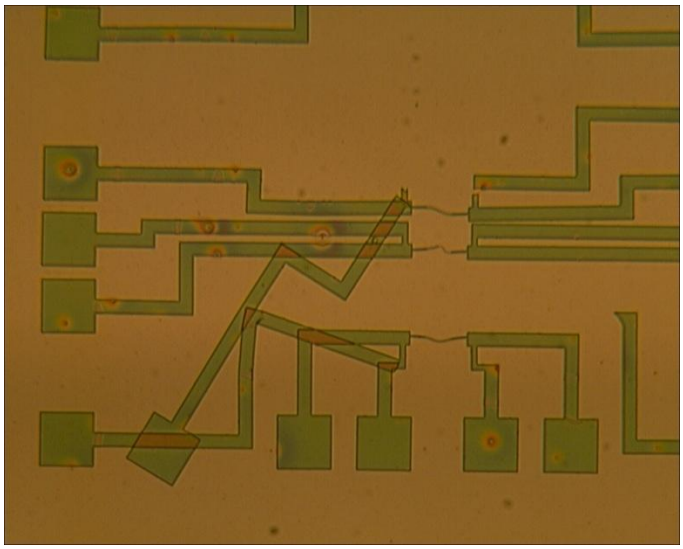

Figure 2.18: Delamination of ma-N2403 after development

As can be seen from picture, the problem was the delamination of the resist from the surface of the wafer. What this means is that the pattern was being exposed correctly, but during the development process, after the excess resist was washed away and the pattern left behind, due to lack of appropriate adhesion to the surface of the wafer, the patterned resist started to come off, or delaminate. Whole sections were either completely removed or removed but later deposited somewhere else in the wafer, as is apparent from Figure 2.18. Another important observation is that the larger features were the ones to delaminate, whereas the submicron features seemed to be mostly distorted, if not removed entirely. After extensive testing, it was found that ma-N2403 is extremely sensitive to the environment in which it is used. Mainly changes in the humidity in the air affect the adhesion behavior of the resist on to the wafer. This was pronounced for this specific fabrication since the DUV mask aligner was located in a different building than the EBL system, and so when the wafer was transported after the EBL exposure to the DUV lithography system, the humidity in the air reduced the adhesion of the resist on the wafer, producing the results seen in Figure 2.18.

In order to overcome this obstacle, many measures were taken so that adhesion would not be a problem. Initially, the use of an adhesion promoter was tested to see if

this would help the resist stick to the surface during the transfer process from one exposure to the next. The adhesion promoter that was used was HMDS, and it was spun on the wafer before coating it with the resist. It was found that instead of helping adhesion, it hindered it instead. After having coated the wafer with HMDS, and spinning the resist on top of that layer, the result was that of streaks of resist on the wafer, and an uneven coating. What turned out to be the solution to the adhesion problem was the use of extreme pretreatment of the wafer and increased care in between processes. Before coating the wafer with ma-N2403, the wafer was heated on a hot plate which was set at 200°C, and pre-baked for a total of 30 minutes. This extreme pretreatment was executed to make sure that the wafer surface was free of water molecules once it was time for spinning the resist. After the pretreatment, the resist was spun and the wafer exposed in the EBL. The second change happened here, where the package in which the wafer was placed was vacuum sealed to prevent any air from going in and to maintain the dry air inside of the package. The vacuum package that was used, and which is shown in Figure 2.20 on the right side, was the Desi-Vac Container with manual vacuum pump from VWR [28]. These changes to the fabrication process proved to be successful in reducing the amount of delamination that happened after development.

Figure 2.19: VWR Desi-Vac Container with manual vacuum pump

CHAPTER 3

OLD SENSOR EXPERIMENTAL SETUPS AND RESULTS

This chapter will cover all of the different experiments that were performed on the old sensors. The old sensors include the 100x2 μm and the 50x1 μm microbridges from the original design, fabricated in 2008.

3.1 Experimental Setups

3.1.1 Sensor Transient Response to Pure Gases

The first experimental setup was simple in that it consisted of a total of six components: a function generator, an oscilloscope, a reference resistor, a glass bottle to act as the container that holds the sensor, the gas to be tested, and the sensor itself. A schematic of the experimental is shown in Figure 3.1. As can be seen in the schematic, the resistor was placed in series with the sensor; this was done in order to measure the current going through the circuit, as the resistance of the sensor would vary depending on the voltage applied and the gas found inside the glass bottle. Channel 1 on the oscilloscope recorded the voltage coming out of the function generator, which was applied across the whole circuit, while channel 2 recorded the voltage drop across the reference resistor. These readings were extracted from the oscilloscope and a computer was used to calculate the resistance change, and thus the signal of the sensor.

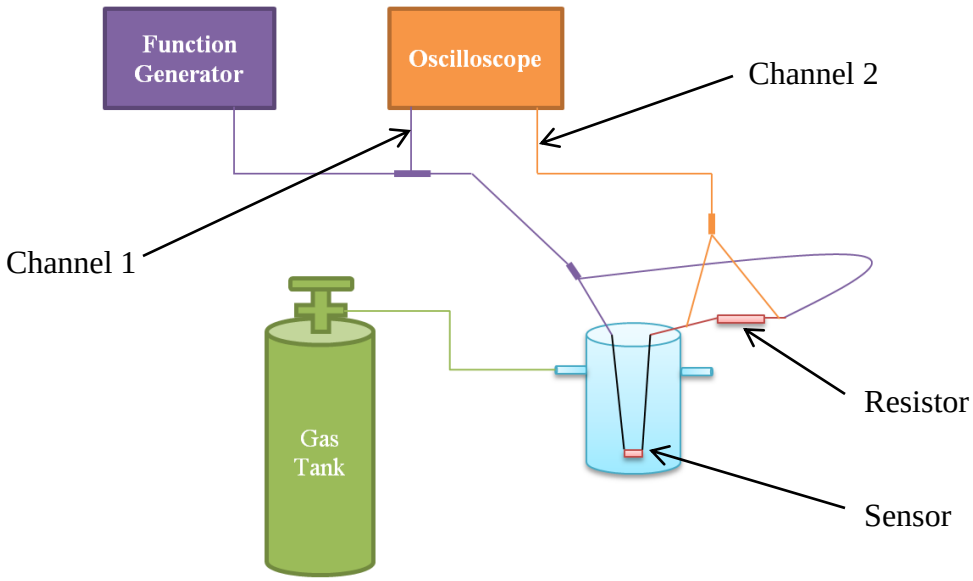

Figure 3.1: Schematic of first experimental setup

The experiment was started by flushing the glass bottle which housed the sensor with the desired gas. The gases that were used during these experiments were carbon dioxide, nitrogen, and helium. The container was flushed for a total of 2 minutes, at which point the gas flow was turned off, and the container sealed to prevent the gas from escaping. At this point the function generator was turned on, applying a pulsed bias across the circuit at a frequency of 500 kHz, that is every 1 µs. The circuit consisted of the sensor and the reference resistor in series, where the reference resistor value was that of 100 Ω. Three different pulsed amplitudes of 4, 4.5, and 5 volts were applied to the circuit. Several pulses were recorded and then averaged for each separate voltage value in order to find the resistance change due to voltage and type of gas.

3.1.2 Sensor Response to Gas Mixtures

A second experimental setup was constructed and utilized much later. The reason behind the second setup was to reduce the noise in the measurements and increase the resolution, allowing for a more accurate measurement of the sensor resistance. A Wheatstone bridge was constructed for this setup, which was composed of the sensor with its respective resistor (R2), and a reference sensor, along with its respective resistor

(R1). The reference sensor was an identical microbridge on the same die, the difference being that it was coated with a glass (Seramic SI from Gelest, Inc). The glass was originally in a liquid phase, which allowed for use of it as a coating for the reference microbridge. The liquid was gently and carefully placed on the target microbridge using an adequate syringe, after which point the microbridge was placed in the oven at 100°C to cure the liquid so that it became a glass. This coating negated the effect of different thermal conductivity of the gases being tested on the microbridge, thus making it the reference sensor. The resistors R1 and R2 had resistance values which very closely resembled the cold resistance value of their respective microbridges. The cold resistance in this case was the resistance value of the microbridge at room temperature before the addition of a gas and the application of bias across it. Along with the Wheatstone bridge, the second setup included the addition of a lock-in amplifier and a digital voltmeter (DVM). The lock-in amplifier was added to the setup so that the AC voltage could be measured across the sensor in the Wheatstone bridge. The lock-in amplifier was the SR830, manufactured by Stanford Research Systems. A schematic diagram of the second experimental setup is shown in Figure 3.2.

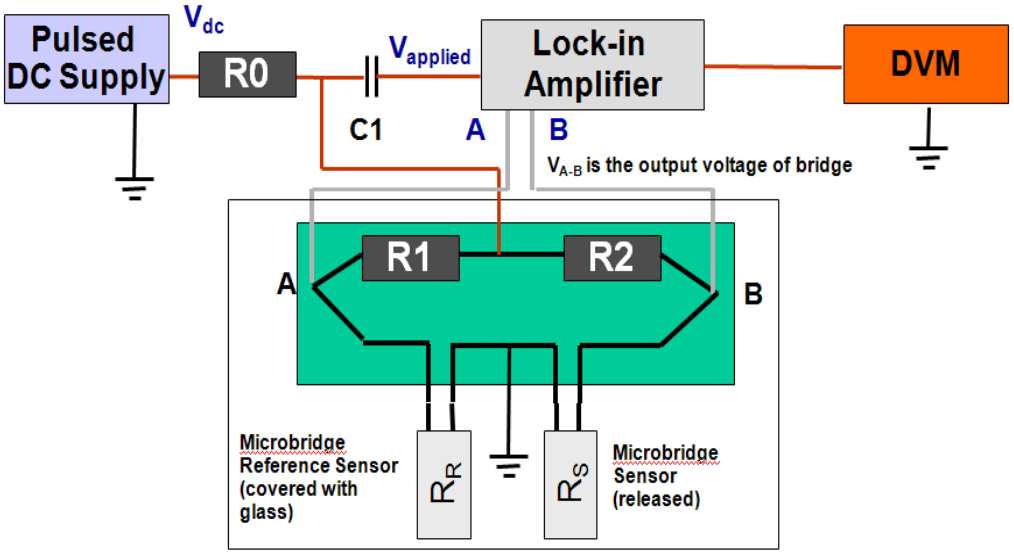

Figure 3.2: Schematic diagram indicating how the instruments are connected to the sensors using the lock-in amplifier

The sensor was kept in the same glass container as in the first experimental setup. The container was filled with the target gas by flushing it for 2 minutes and then closing it, preventing the gas to escape. The target gases included helium, nitrogen, and carbon dioxide. This setup also differed from the first one in that gas mixtures were also tested, allowing for more complex characterization of the sensor. A pulse of amplitude 3.5, 4, or 4.45 volts with an AC signal up to 500 mV (RMS) was applied to the sensor. The pulse duration was varied to achieve stable readings of resistance between 0.1 second and 2.5 seconds. At larger AC amplitudes a heating effect was observed, where each successive pulse produced a slightly higher resistance reading. This was ascribed to increased power dissipation generated at larger amplitude AC excitation. Therefore most measurements were made with 62 mV excitation. Various time constants were investigated with the lock-in amplifier to reduce noise and provide a stable resistance reading. It was found that a time constant of approximately 1/10 the period of the pulsed signal was optimum. The voltage across the sensor was recorded with a data logging DVM which takes a reading every tenth of a second and stores up to 200 readings. The voltage reading was then converted to resistance values using a computer. Various input voltages were applied to better characterize the sensor and to gauge the effect on temperature changes in the sensor. Figure 3.3a shows the schematic of the setup, while Figure 3.3b shows photographs of the physical setup.

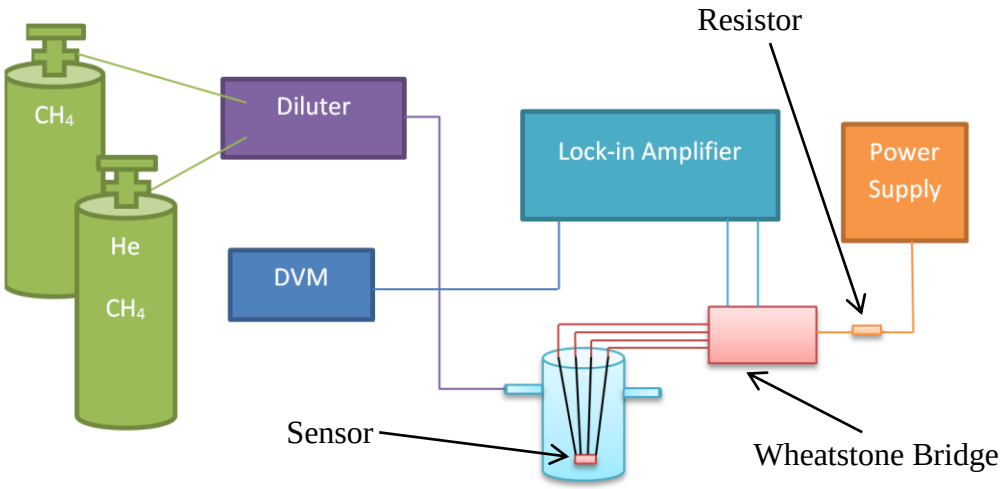

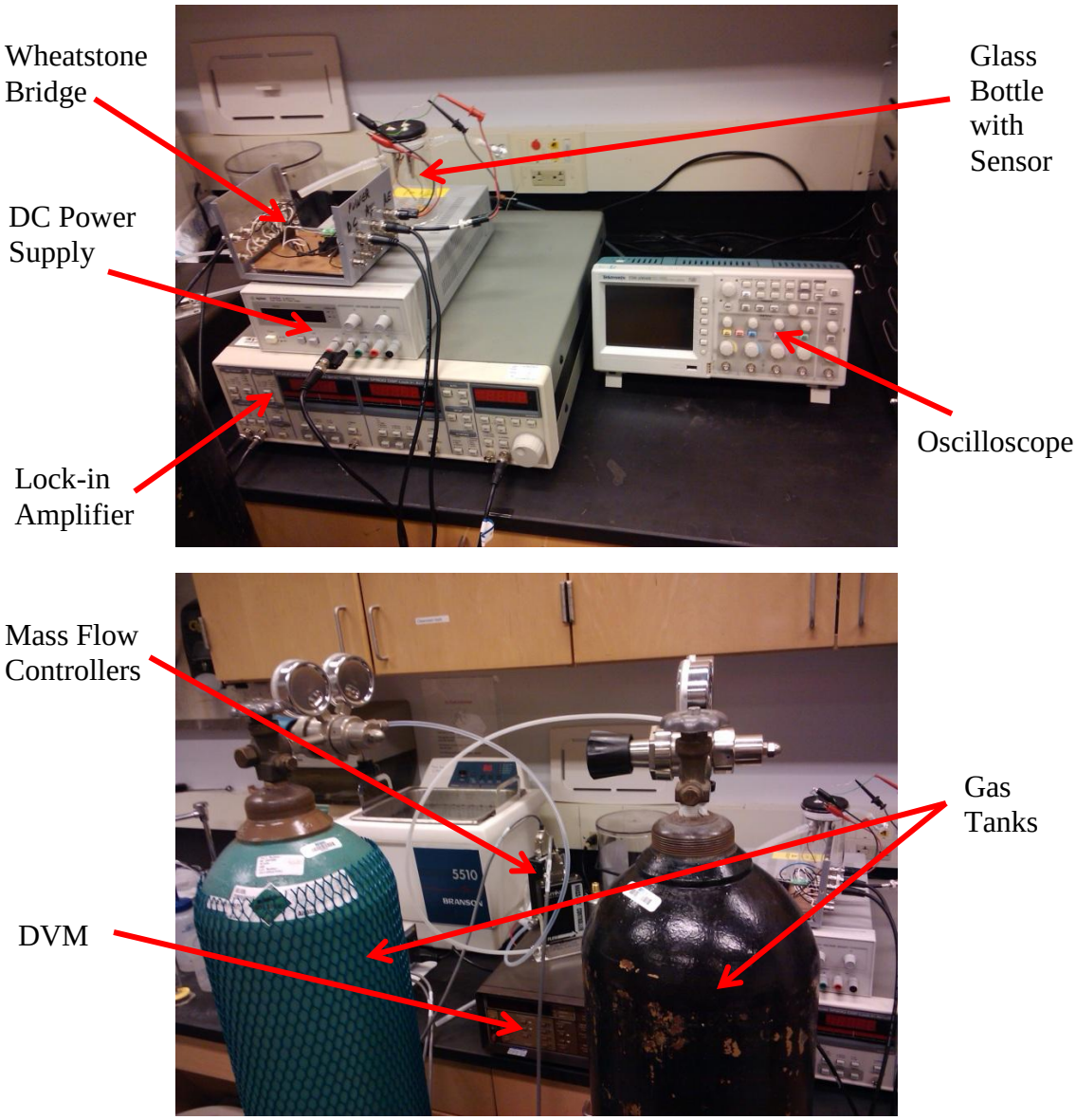

Figure 3.3: a) Schematic of gas mixture setup; b) Photographs of physical Wheatstone bridge setup

Shown in Figure 3.3b is not only the setup for the Wheatstone bridge, but also some additions for the purpose of testing gas mixtures. The mass flow controllers (MFC) were added to regulate the volume of gas coming out of each of the gas tanks and the rate at which the gases came out. Through this regulation, the mixing of the gases was possible, allowing for the control of the actual gas mixture composition. The setup was

further tweaked by replacing the electrical MFC's with a solenoid driven gas mixer which was able to produce more accurate gas mixtures. It was found through testing that the MFC's were either faulty or could not handle the low gas flows that were required to obtain the desired gas compositions. Due to the fact that they did not give the correct compositions, and were expensive to either have them repaired or buy them, it was decided to replace them with the 1010 Precision Gas Diluter from Custom Sensor Solutions Inc. The DVM was also replaced with a new, more powerful one from Fluke, specifically the 8846A. This instrument was able to record 6 digit readings with a 6.5 digit resolution, and a range of 10 Ω to 1 GΩ, with good resolution. Figure 3.4a shows the solenoid gas mixer [29], while Figure 3.4b shows the Fluke DVM that was utilized to record the resistance readings [30]. Using this setup, the testing of gas mixtures became possible, allowing for not only testing helium in nitrogen, but also methane in nitrogen.

Figure 3.4: a) Solenoid gas mixer; b) Fluke DVM

3.1.3 Temperature Calibration

A separate experimental setup from the testing of gases was designed in order to perform a temperature calibration of the sensor. This was done in order to more accurately estimate the temperature of the microbridge during operation and testing of it under different conditions. The temperature calibration setup consisted of the following instruments: the sensor, the DVM, a thermocouple, and an oven that was able to reach temperature upwards of 300°C. A schematic of the setup used for this experiment is

shown in Figure 3.5. As the schematic portrays, the sensor was placed in the oven, with wires going from the sensor, out of the oven, and connecting to the DVM. Due to the nature of the experiment in that there was no testing of the gases, the glass bottle was not used; instead only the sensor package was placed in the oven, along with the wires that ran into the oven to connect the sensor to the DVM. The thermocouple wire was run into the oven as well and placed in a manner in which it was touching the sensor package. This was done in order to get a more accurate reading of the actual temperature of the sensor substrate, and not necessarily the oven itself. The temperature of the oven was increased steadily, noting the temperature of the sensor, and recording the resistance value of the sensor at each temperature intervals of 10°C initially. It was found that the thermocouple in use was reading temperatures that were off due to it not being connected correctly and thus not reading as a Type K thermocouple; adjustments were made accordingly, which are reflected in the results shown in the next section.

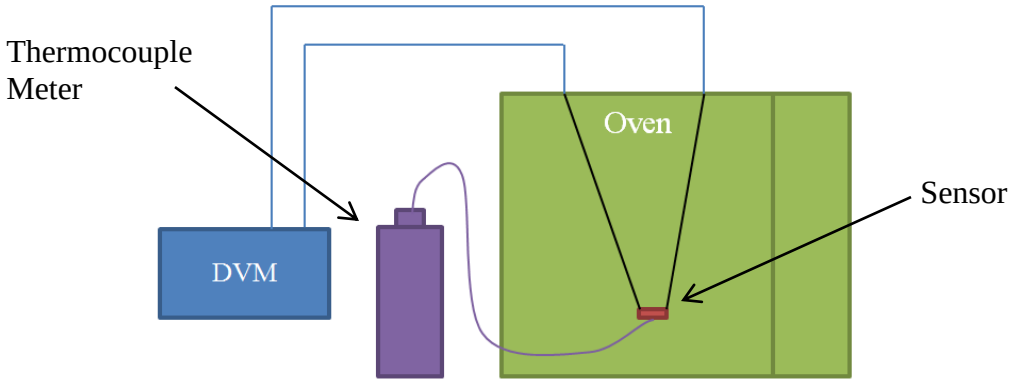

Figure 3.5: Schematic of temperature calibration setup

3.2 Experimental Results

3.2.1 Pure Gases Experiment Results

The first set of experiments that were conducted utilized the first experimental setup, using only on gas at a time. The first microbridge to be used for these experiments

was the 100x2 µm. The baseline resistance of this microbridge was measured to be around 1659 Ω. This value was important in that with it, the resistance change in the sensor could be calculated. The experiment was conducted by exposing the sensor to pure gases, which included nitrogen, carbon dioxide (for preliminary characterization purposes only), and helium. The voltage applied across the sensor was varied between 2 and 4.5 volts, in increments of 0.5 volts. The same experiment was run using the 50x1 µm sensor, except that in this case the range was increased to include 5 volts. The baseline resistance of this smaller microbridge was measured to be around 2618 Ω. It was found that this sensor produced a larger resistance change when a voltage was applied to it than the 100x2 µm sensor; thus it was found that the smaller sensor was indeed more sensitive. Figure 3.6 shows two comparison graphs, one at 4 volts and the second one at 4.5 volts, of the resistance change measured for the three different gases between the 100x2 µm and the 50x1 µm sensors.

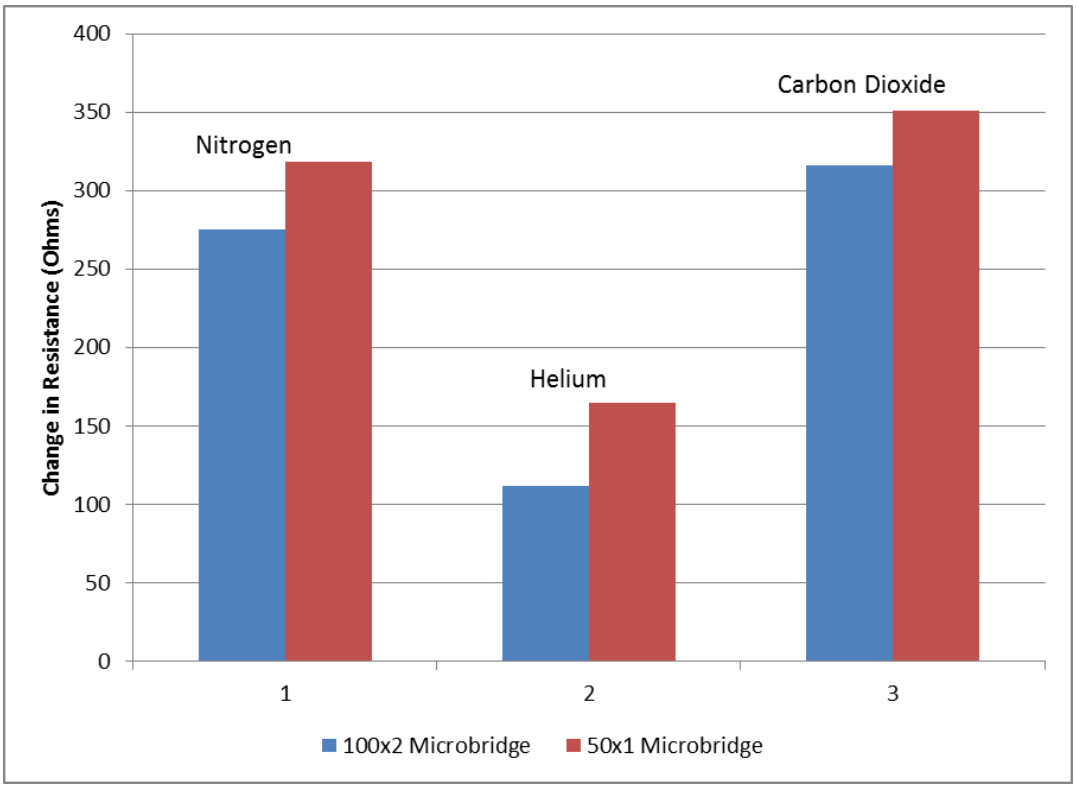

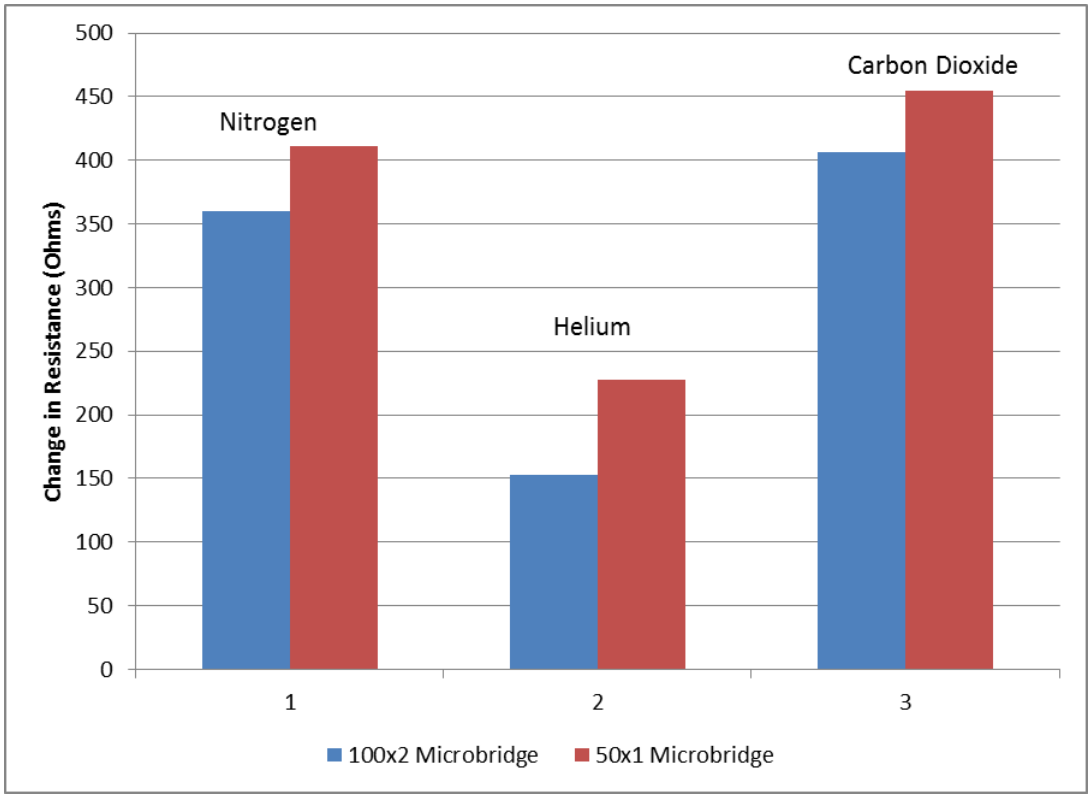

Figure 3.6: a) Resistance change comparison at 4 volts; b) Resistance change comparison at 4.5 volts

Due to the higher sensitivity of the 50x1 µm sensor, the rest of the experiments were done using only this sensor. A comparison of the resistance change for each of the first three gases mentioned is given in Figure 3.7 for the 50x1 µm microbridge. The graph shows the readings obtained at three different voltage values, that is 4, 4.5 and 5 volts. As can be seen from the graph, among the three gases the resistance change for carbon dioxide was the greatest, while that for helium was the least. Overall, applying higher voltages yielded higher resistance changes for all three gases that were tested. In addition, for the 4 volts data, it was calculated that the power consumption for helium was around 16.1 mJ, whereas for nitrogen it was 11.5 mJ.

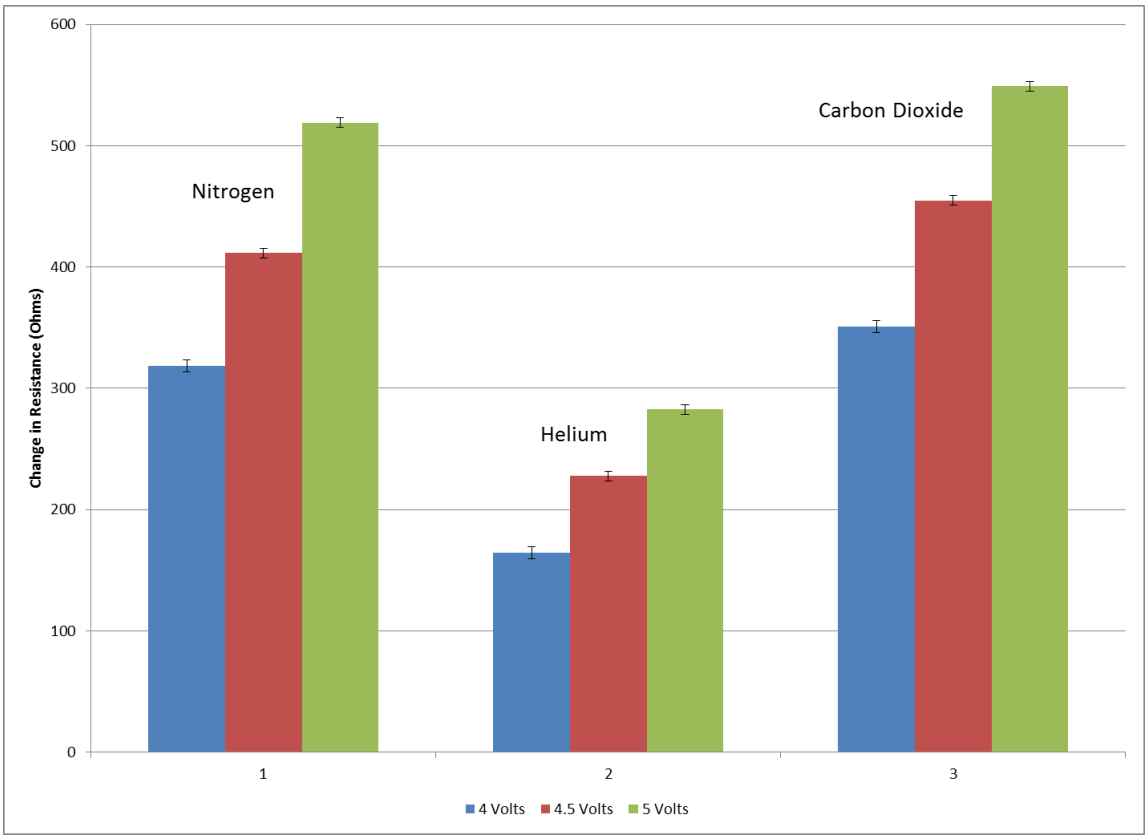

Figure 3.7: Resistance change for the 50x1 µm at three different operating voltages – 4, 4.5, and 5 volt pulses for different pure gases

The reason behind using pulsed bias was that by doing so, the power consumption would be reduced, along with preventing the sensor from having a heating effect that can occur at a constant voltage. With the first experimental setup however, the pulsed bias experiment still produced very noisy data, so the setup was changed to the second setup described earlier. Three different pulsed voltages of 3.5, 4, and 4.45 were applied across the Wheatstone bridge and the LIA amplitude data was recorded using the Fluke DVM. This was done for nitrogen and helium separately. Figure 3.8 shows typical results from this experiment with voltage pulse amplitude of 4V to the sensor in nitrogen and in helium. As expected, the resistance change of the microbridge in nitrogen is much greater than in helium. The repeatability of the sensor response demonstrates the robustness of the sensor for continuous operation. Therefore, many consecutive pulses

can be used for data averaging to improve the accuracy of the resistance readings. With the use of the Fluke DVM, readings were obtained with a resolution of approximately 1/10 of an ohm.

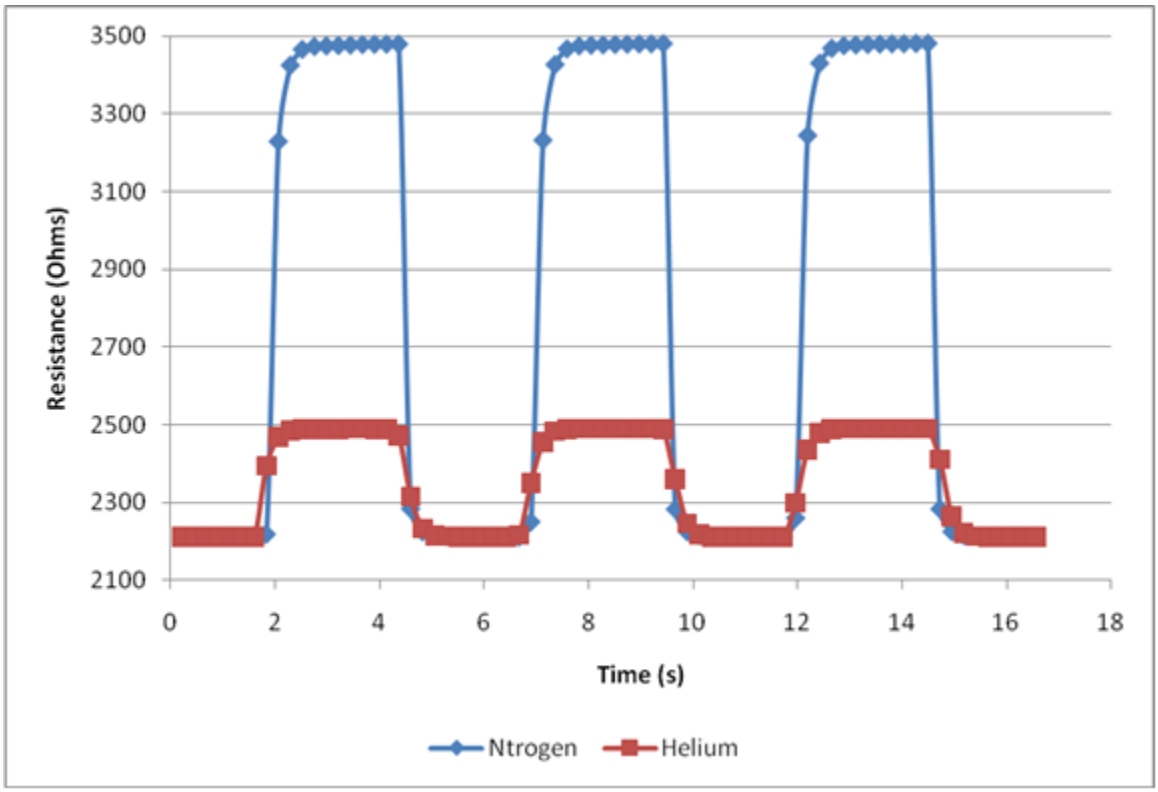

Figure 3.8: Resistance response of 50x1 µm sensor in both nitrogen and helium at 4 volts

3.2.2 Gas Mixture Experiment Results

The second type of experiment that was conducted was that of the gas mixture experiment. In this experiment, the glass container was flushed with a mixture of helium and nitrogen, or a mixture of methane and nitrogen. The mixture was based on nitrogen, with different concentration of helium or methane. For both of these gases, the concentrations ranged from 1% to 5% of each respective gas in nitrogen.

The sensor response to different concentrations of helium is shown in Figure 3.9. From the slopes that were calculated, the resistance change at 5V operation was found to be 2.05 mΩ/ppm, at 4.5V it was 1.14 mΩ/ppm, and at 4V it was 0.7 mΩ/ppm. The standard deviation of noise level in the setup was about 86 mΩ; therefore, with 5V

operation the sensor can detect 126ppm helium in nitrogen with signal-to-noise ratio at three, i.e., the criteria for limit of detection.

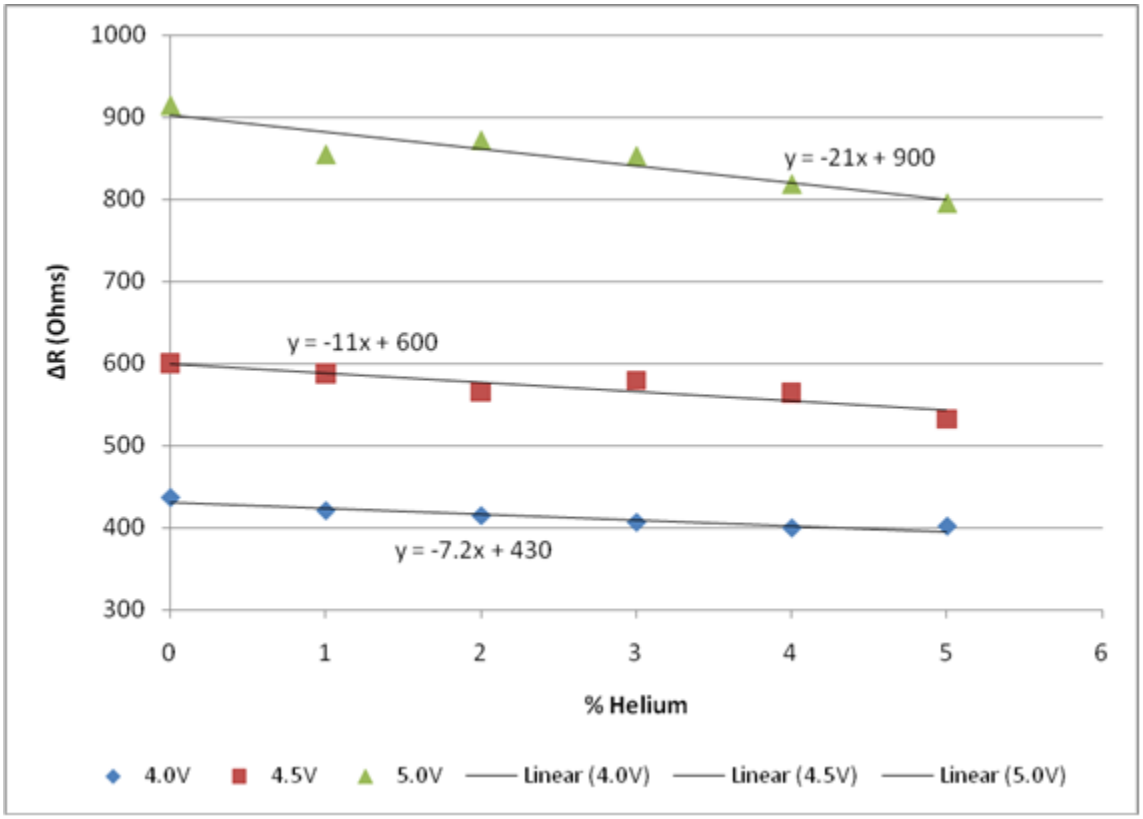

Figure 3.9: Resistance change as a function of different helium concentrations in mixture

The second experiment on gas mixture was conducted in which the glass container was flushed with a mixture of methane and nitrogen. Again, the mixture was based on nitrogen, but instead of helium, methane was used at different concentrations. The sensor response to these different concentrations of methane is shown in Figure 3.10. From the slopes that were calculated, the resistance change at 3.6V hot operation was found to be 0.75 mΩ/ppm, at 3V it was 0.49 mΩ/ppm, and at 2.5V it was 0.078 mΩ/ppm. Again, the standard deviation of noise level in the setup was about 86mΩ; therefore, with 3.6V operation the sensor can detect 344 ppm methane in nitrogen with signal-to-noise ratio at three.

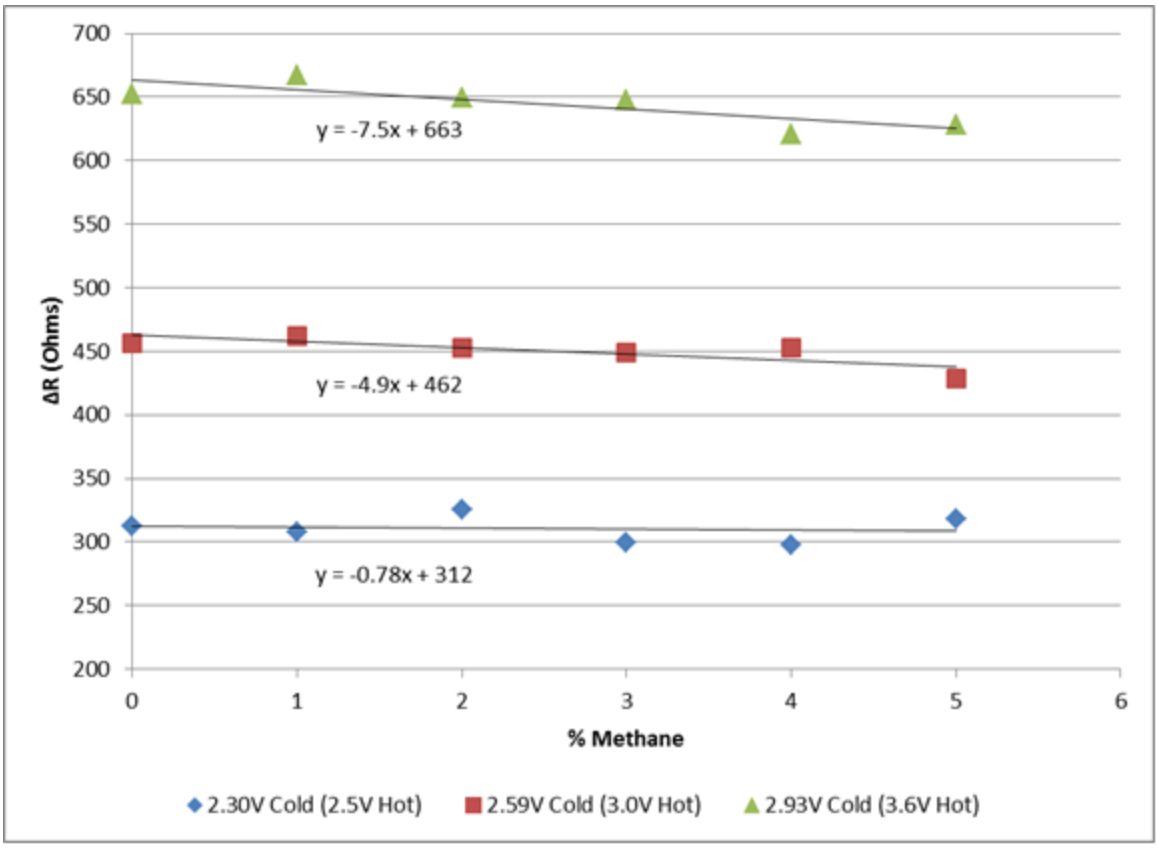

Figure 3.10: Resistance change as a function of different methane concentrations in mixture

As can be seen from the figures above, the sensor's detection level does increase as the voltage applied is increased. However, due to overheating and possible damaging to the microbridge, lower voltages had to be used for the methane and nitrogen mixture experiment. Even though lowering the voltage does decrease the sensitivity, the difference of the impact of the thermal conductivity of each gas mixture on the change in resistance in the sensor can be observed. Overall, the sensor is more sensitive to helium in mixture than to methane in mixture.

3.2.3 Temperature Calibration Experiment Results

A temperature calibration experiment was carried out on the sensor in order to obtain a relationship between the resistance change in the sensor and the temperature at those points. This would allow for a better estimate of the overall sensor temperature

during operation. The temperature calibration was conducted not only on the 50x1 µm microbridge, but on the 100x2 µm with a 50x1 µm center as well. The temperature calibration for the 50x1 µm was done up to a temperature of about 172°C. The temperature calibration for the 100x2 µm with a 50x1 µm center was done up to a temperature of about 220°C. Figure 3.11 shows the temperature calibration plot for both microbridges. As is shown, the sensor's temperature dependence can be modeled by a cubic function.

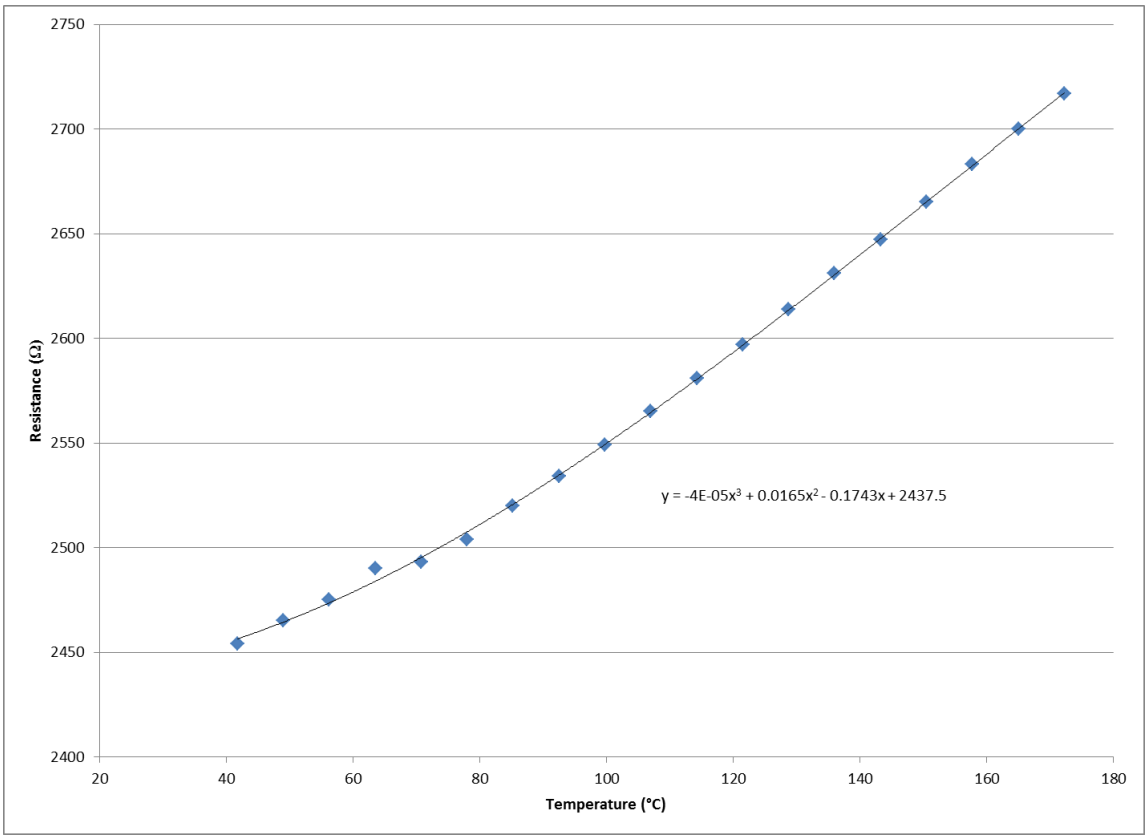

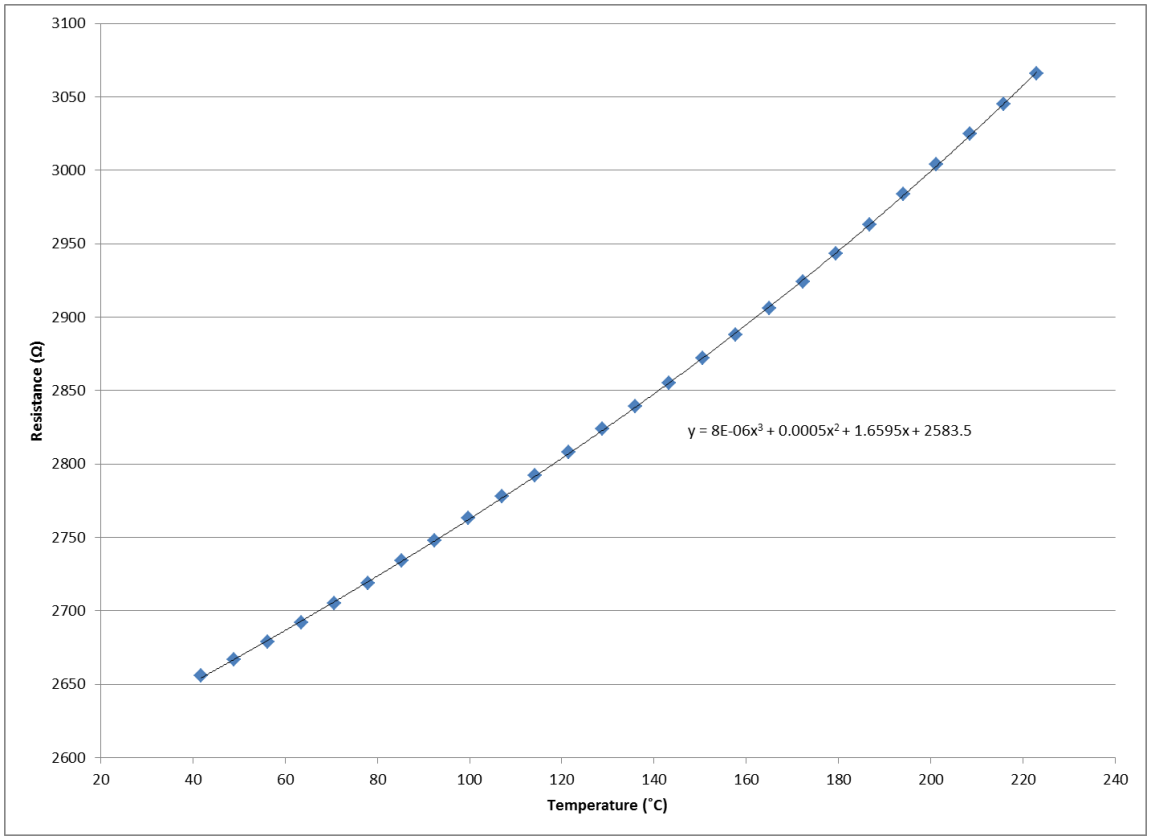

Figure 3.11: a) Resistance vs. temperature for the 50x1 µm microbridge; b) Resistance vs. temperature for the 100x2 µm with 50x1 µm center microbridge

The relationship between the temperature and the resistance of the microbridges was originally observed as a linear relationship. This was due to the fact that the temperature calibration which was first done only went up to about 100°C, which did not allow for the full profile to be studied. With the above data however, the temperatures to which the microbridges were heated too well exceeded the 100°C. Figure 3.12a and 3.12b shows the same temperature calibration plots as the ones above, except it shows them with a linear fit, along with the R value that is associated with each fit. Figure 3.12c shows a plot of the temperature calibration that was performed on a separate 50x1 µm microbridge up to a temperature of 100°C. As can be seen from the plots, the linear fit is not perfect but it is close, close enough to use for approximation. Also, the slopes for both 50x1 µm microbridges have a lower value than that of the larger microbridge.

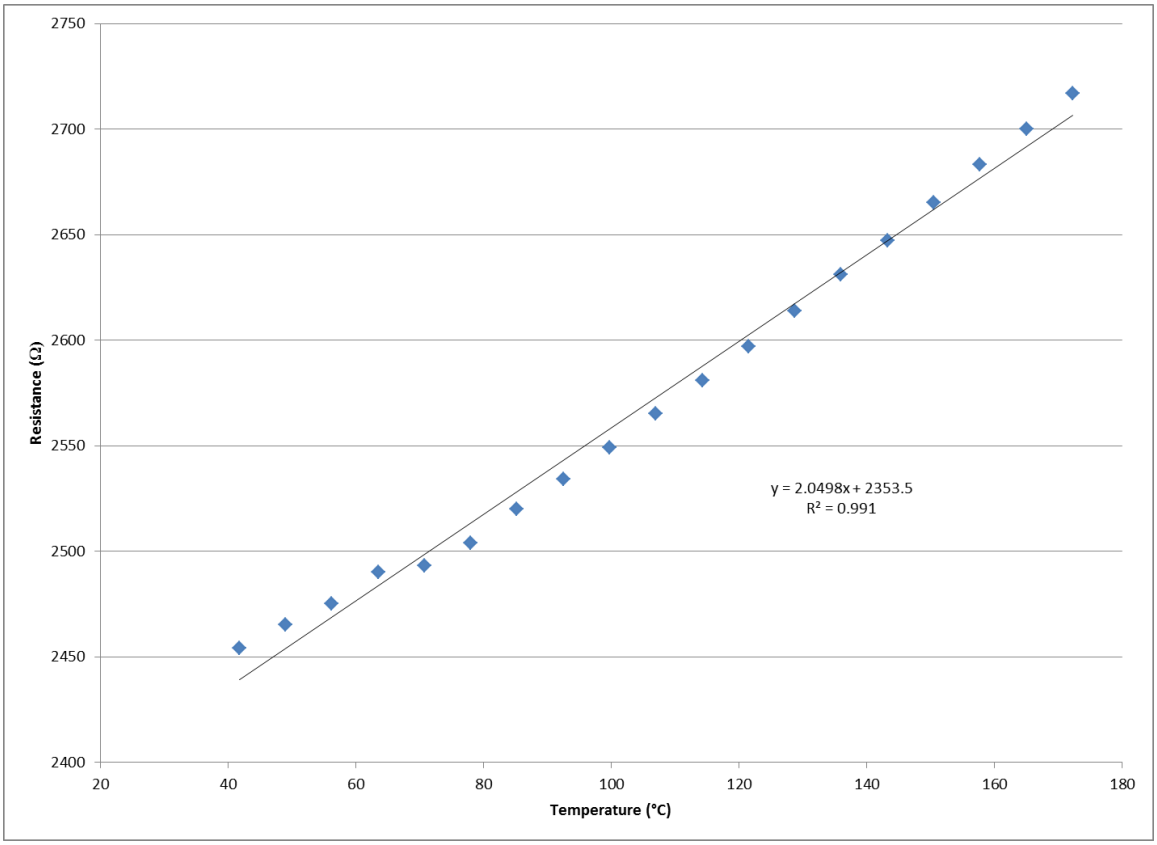
Resistance (Ω)
Temperature (°C)
y = 2.0498x + 2353.5
R² = 0.991

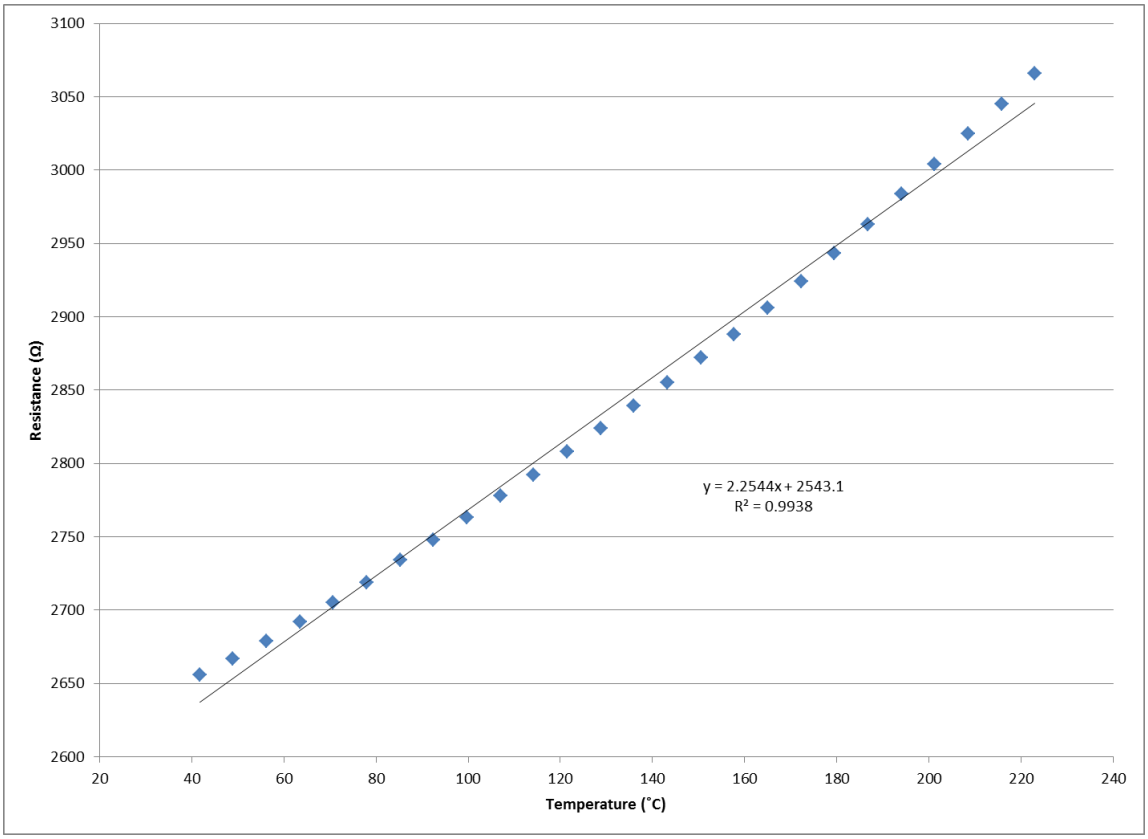
Resistance (Ω)
Temperature (°C)
y = 2.2544x + 2543.1
R² = 0.9938

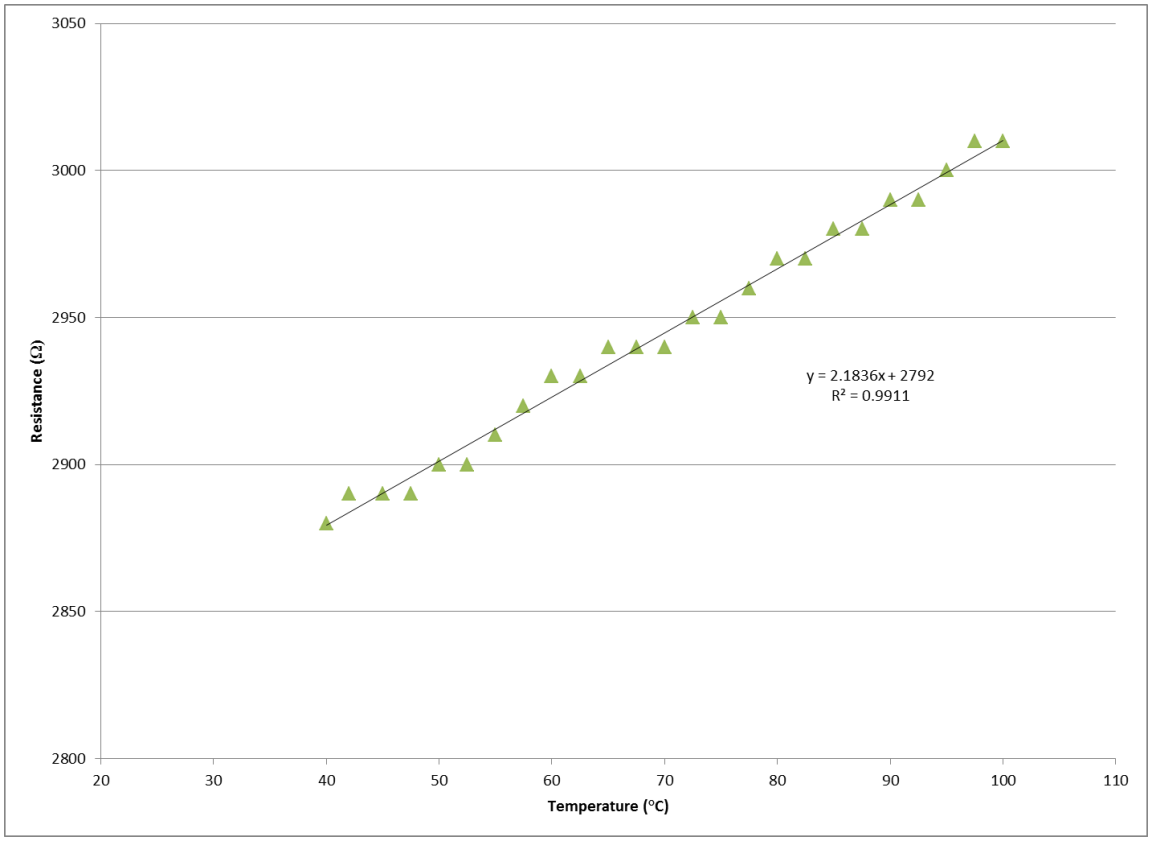

Figure 3.12: Resistance vs. temperature linear fit – a) 50x1 µm microbridge; b) 100x2 µm with 50x1 µm center microbridge; c) Separate 50x1 µm microbridge up to 100°C

CHAPTER 4

NEW SENSOR EXPERIMENTAL SETUPS AND RESULTS

This chapter will cover all of the different experiments that were performed on the new sensors. The new sensors include the 50x1 μm (Die 1), the 100x2 μm with 50x1 μm center (Die 2), and the 50x1 μm with 25x0.5 μm center (Die 3) microbridges from the new design.

4.1 Experimental Setups

4.1.1 Time Response of the Sensors

The first experimental setup for the new sensors was actually the same first setup that was used in Chapter 3. This setup is shown again in Figure 4.1. The only difference was in the way the data was acquired. For the first experiment conducted on the new sensors, the reading that was recorded was the response time of the sensor to the gas. This was done by changing the time interval in the oscilloscope, shortening it so that a recording of the time response of the sensor could be accomplished. One obstacle that manifested during testing was that the measurements had a lot of noise with it. It was found that this was being caused by the cables and their length. For the frequency at which the tests were operating at, the long BNC cables added a significant amount of noise to the data. It was for this reason that shorter BNC cables were made, with a length of 5" from end to end. This eliminated the excessive noise, and allowed for more comprehensive measurements.

In order to observe the differences in response time between each of the dies that were tested, the experiments were kept the same, regardless of the sensor in question. The function generator was set to apply voltages which on the test circuit were equivalent

to 10 mW, 7 mW, and 4 mW of power to the sensors in Dies 1 and 2, whereas for the sensor in Die 3, the powers applied to the sensor were that of 3 mW, 2 mW, and 1 mW. Since the size of the sensor in Die 3 is half that of Die 2, the power applied had to be roughly a quarter of what was applied to Die 2, which is why the power levels are lower for Die 3. Nitrogen and helium were used to flush the glass bottle, as separate test runs. Similarly to the old sensor single gas test, the container was flushed for 5 minutes with the desired gas before sealing it. These tests were done on the first three dies from the new design, at a frequency of 2 kHz to capture the full response.

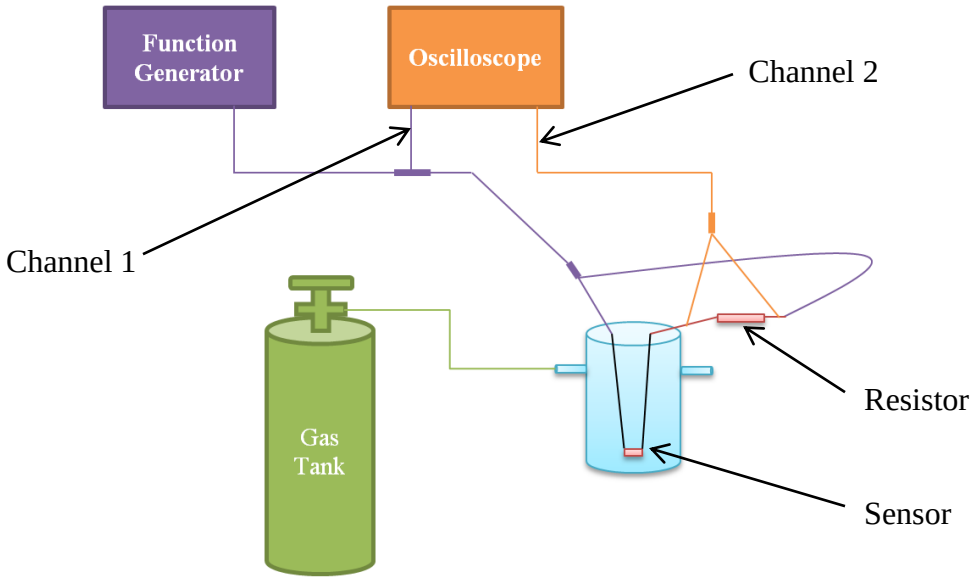

Figure 4.1: Schematic of first experimental setup on the new sensors

4.1.2 Life Test on Sensor

The second experiment was conducted, using the setup shown in Figure 4.2. The purpose behind this setup was to test the robustness of the new sensors. This was done by placing a sensor, in this case a sensor from Die 5, in series with a resistor of 100 Ω, and applying a voltage to the circuit. To truly test the life of the microbridge, the voltage applied was a square wave, meaning it was pulsed with a frequency of 10 kHz. With such frequency, the sensor received voltage pulses at a rate of about 36 million pulses per hour, which was ideal for a life test. The power that was applied to the sensor was

originally that of 2.95 mW. The baseline resistance value of the sensor was recorded as often as possible, if not every day. After a period of 30 days however, the power was increased to about 5 mW. This was done to see if this increase in power would have an effect on the sensor. The temperature of the room was also recorded at this time, for the sole purpose of observing the effects of the room temperature on the sensor signal.

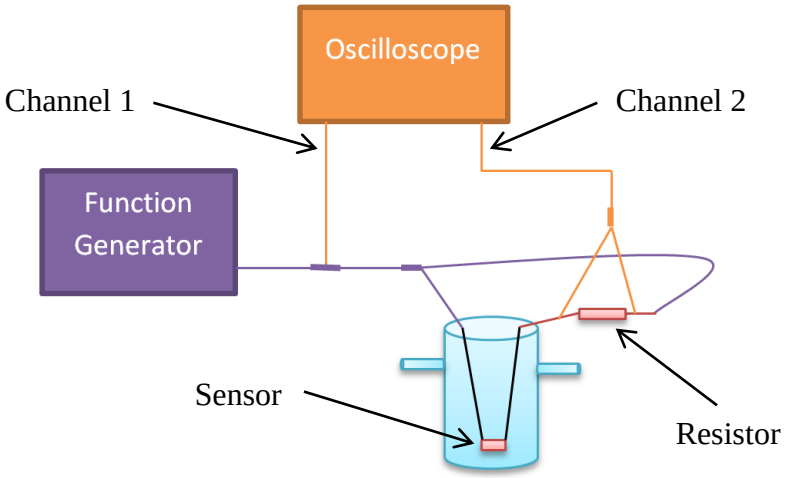

Figure 4.2: Schematic of life test setup

4.1.3 Palladium Coating Setup

The third experiment was done on the palladium coated dies, that is Dies 4, 5 and 6. The palladium coating was evaporated on these dies, as was mentioned in Chapter 2, Section 1 of this Thesis, for the purpose of selectively sensing hydrogen. About 60 nm of palladium were evaporated on the dies. The film had to be a relatively thin film due to the low resistivity of palladium, a resistivity of 105.4 nΩ-m. This meant that evaporating thicker films of palladium on the microbridges would reduce the baseline resistance of the palladium coating. The target baseline resistance so that meaningful data could be measured with it was that of about 100 Ω to 300 Ω, which was obtained with the 60 nm film thickness.

The setup was simple in the sense in that it did not use the Wheatstone bridge, and thus did not require use of the lock-in amplifier. Since the coatings on the microbridges

had never been characterized, it was decided to make the initial tests as simple as possible to get preliminary results. Another aspect of the setup was that instead of using a function generator which can apply a pulsed bias on the sensor, a power supply was used which applied a constant DC voltage. This voltage was applied across a circuit which was composed of the microbridge and a resistor of 220 Ω connected in series. The resistor was added in order to measure the current flowing through the circuit, by measuring the voltage drop across said resistor and calculating the current. A handheld voltmeter was used to measure the voltage drop across the resistor. The calculated current and the applied voltage were then used to calculate the resistance of the microbridge during the experiment. The Fluke DVM used in the experiments for the old sensors was connected across the extra platinum leads which, via the palladium coating, were now connected. The DVM recorded the resistance value of the palladium coating as the voltage across the microbridge/resistor circuit was increased. These measurements were below kΩ range, and thus the DVM proved useful with its 6 digit resolution. Even though this was the original intent for a palladium sensor setup, a few changes were made which are explained below. A revised schematic of the palladium coated sensor setup is shown in Figure 4.3.

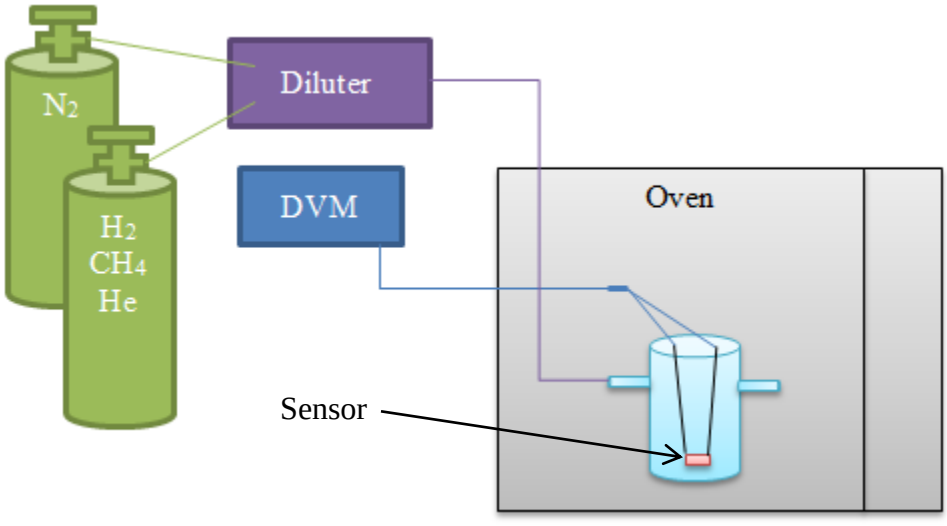

Figure 4.3: Schematic of palladium coated sensor setup

As can be seen from Figure 4.3, the sensor was placed in an oven, while the power supply and resistor were removed. Originally, the sensor was enclosed in a glass bottle, the same one that was used in the experiments with the old sensors, and it was left out in the ambient. The bottle was flushed with a mixture of 5% hydrogen in nitrogen tank for 5 minutes, at which point the bottle was closed up, leaving the mixture inside. The gas tank used for hydrogen was 5% hydrogen in nitrogen tank. This was done because of the highly flammable nature of hydrogen; having the 5% tank made it possible to run the experiments, giving a range of 0% to 5% hydrogen by mixing the 5% tank line with a pure nitrogen tank line. Once the voltage was applied, the microbridge would heat up, heating up the palladium coating and activating it so that it would selectively sense hydrogen. After several experiments however, it was observed that there was a significant amount of drift in the palladium coating signal, even when the hydrogen concentration was changed. It was then decided to maintain the whole substrate at a constant external temperature to see if this would help eliminate the drift. This was done by placing the glass bottle inside the oven and disconnecting the power supply from the circuit, as is shown in Figure 4.3. The temperature of the oven was then set to the 100°C necessary to activate the palladium coating. It was found that placing the sensor in the oven was a good way to minimize the drift, and thus more meaningful responses could be recorded.

4.1.4 Tin Oxide Coating Setup

The fourth experiment was done on the tin oxide coated dies, that is Dies 4, 5 and 6. The tin oxide coating was sputtered on these dies, as was mentioned in Chapter 2, Section 1 of this Thesis, for the purpose of selectively sensing methane. About 250 nm of tin oxide were sputtered on the dies. This fourth experimental setup was very similar to the third one described previously. There are a few key changes however, due to the fact that the metal coating which was being tested was tin oxide which required higher

temperatures to activate. For this reason the preliminary experiments performed were done in order to activate the coating and induce a response when introducing methane gas. One of the differences is that the oven was not used in the setup. This was the case due to the fact that in order to activate the tin oxide film, a temperature upwards of 400°C was needed. The oven that was available for running the experiments was not configured to go that high in temperature. For this reason, the activation of the tin oxide film was done by heating the microbridge enough so that a response from the tin oxide was observed. The power supply was once again incorporated into the setup, as well as the 220 Ω resistor and the handheld voltmeter. Figure 4.4 shows a schematic of the tin oxide coated sensor setup.

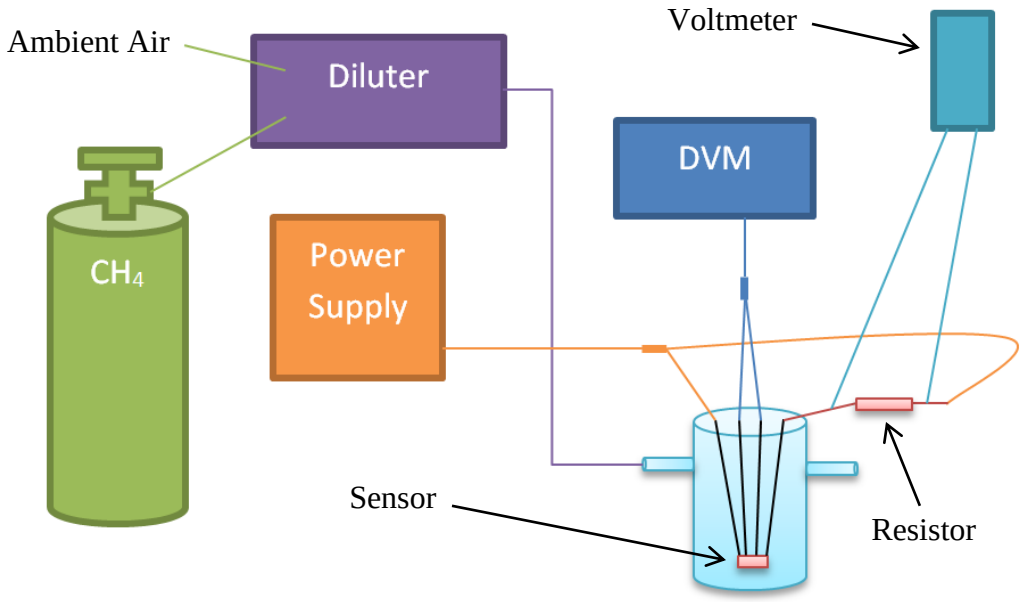

Figure 4.4: Schematic of tin oxide coated sensor setup

Before running the tin oxide experiment, an experiment was run in order to observe the relationship between the platinum resistance and the operating temperature. This temperature calibration was necessary so that with it, it would be possible to approximate the temperature of the tin oxide given a certain power level. A sensor with no coating on it was connected to the setup. The sensor had to have the extra set of platinum runners actually making contact for this to work, since the goal here was to see

how the platinum resistance changed as the microbridge under it was heated due to the current. Figure 4.5 shows an optical image of a typical Die 4 sensor which has the platinum runners all along the microbridge. Once connected, a voltage was applied to the microbridge, and it was increased in increments of 0.2 volts up to a voltage value of 4.4 volts. The resistance of the platinum and the voltage drop across the resistor were recorded per voltage increase.

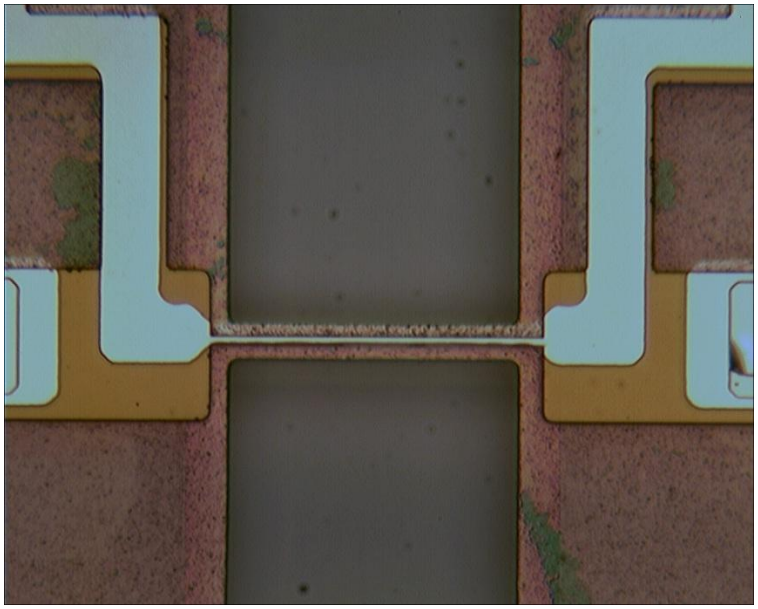

Figure 4.5: Microbridge with platinum runner

The tin oxide experiment differed from all other experiments in that instead of flushing the container with the target gas, a constant flow of either pure nitrogen or the target mixture was kept during the tests. At first, ambient air was introduced in the chamber. A bias was then applied to the sensor/resistor circuit, starting from 0.5 volts. Since no response was observed from the tin oxide coating, the voltage was increased by 0.5 volts. This process was conducted until a response was seen from the tin oxide film. Initially the response obtained was in the range of hundreds of Mega ohms, so the voltage was further increased until the reading dropped and was stable enough to run experiments with. At this point, the gas flow was switched every minute, starting with ambient air. After the first minute the first concentration of 5% methane was introduced into the line.

Once again after the next minute, the line was flushed with ambient air and kept for another minute. This was done for a total of about 10 minutes, allowing for methane concentrations of 1% to 5% to be tested. The methane response however was observable only for concentrations from 3% to 5% methane. For these tests, a 5% methane in nitrogen tank was used for the same reasons for using a 5% hydrogen in nitrogen tank for the palladium sensor testing described earlier.

4.2 Experimental Results

4.2.1 Time Response Experiment Results

The first tests that were conducted on the new sensors were the transient response tests. The purpose behind these tests was to characterize the sensors in terms of how quickly they respond, depending on the dimensions of the sensor and the gas that was present at the time. A way to differentiate the transient response between each microbridge is to look at the time constant for each. How quickly a sensor can respond and produce a signal is important, which is where the time constant comes into play. The different time constants were obtained from the transient response graph of each die in each gas present. Table 4.1 shows the time constant for each microbridge dimension, in both nitrogen and helium.

Table 4.1: Time constants

	Nitrogen			Helium		
Power (mW)	Die 1 (μs)	Die 2 (μs)	Die 3 (μs)	Die 1 (μs)	Die 2 (μs)	Die 3 (μs)
10	61.35	55.55	N/A	15.75	25.19	N/A
7	54.65	65.36	N/A	21.60	37.17	N/A
4	53.19	47.17	N/A	22.07	30.40	N/A
3	N/A	N/A	47.85	N/A	N/A	16.75
2	N/A	N/A	32.26	N/A	N/A	8.44
1	N/A	N/A	34.36	N/A	N/A	9.78

4.2.2 Life Test Results

The second tests consisted of applying a set power to the microbridge, in this case the sensor from Die 5, and leaving it in operating mode until the sensor failed. The purpose of this test was to understand and observe the robustness of the sensors. The sensor initially had a baseline resistance of 12.99 kΩ. A voltage of 5.52 volts was applied to the circuit, which was equivalent to 2.95 mW. The frequency as was mentioned previously was set to 10 kHz, which is about 36 million pulses per hour. The resistance of the sensor was recorded for a period of 30 days. At this point the power was increased to 5 mW by applying a voltage of 7.2 volts. The resistance was once again recorded until it was found to be too unstable, which meant the sensor had failed to function properly. Figure 4.6 shows the findings of this test.

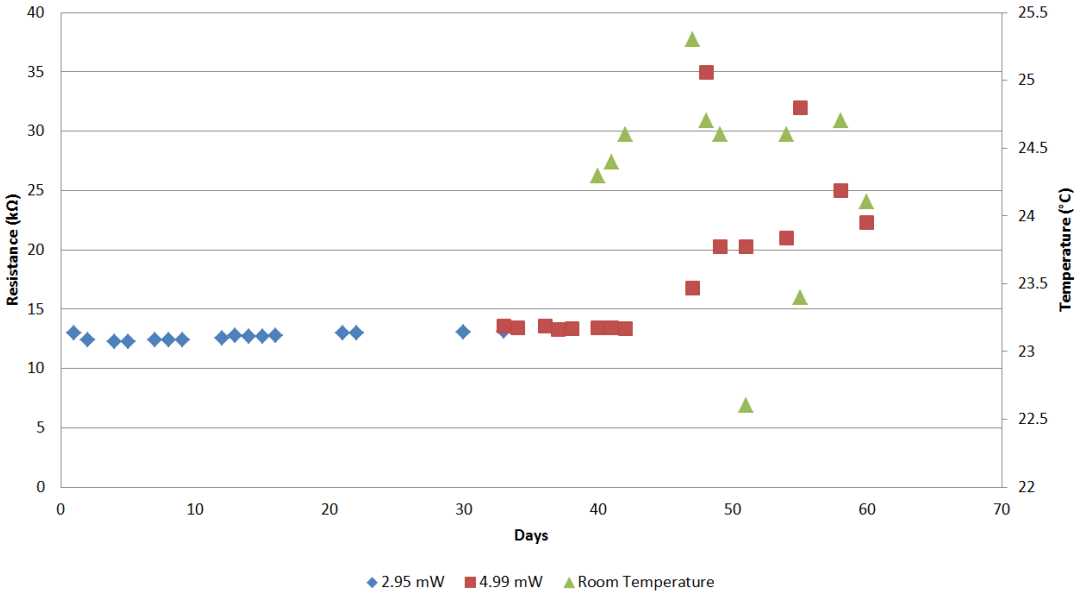

Figure 4.6: Resistance of Die 5 sensor over time in days during constant operation

4.2.3 Palladium Coating Experiment Results

The third tests were run in order to characterize the palladium coating that was evaporated on the microbridges from the new design. Even though three different microbridges were designed for metal coating testing, only one was experimented with which had the palladium coating on it. Die 5, which is the 100x2 µm with a 50x1 µm center, was the microbridge with palladium coating that was tested for hydrogen sensing. In order to activate the palladium film, the microbridge had to be heated up to a temperature of about 100°C. The voltage needed to heat the microbridge up to that temperature was obtained by conducting a temperature calibration test on the Die 5 with the palladium coating. Figure 4.7 shows the graph of the temperature calibration that was performed on the palladium sensor. Since this was a preliminary test, it was assumed that the resistance to temperature relationship was a linear one. Using this linear fit, it was calculated that the required voltage that was needed to heat the microbridge to the desired 100°C was about 1.6 volts.

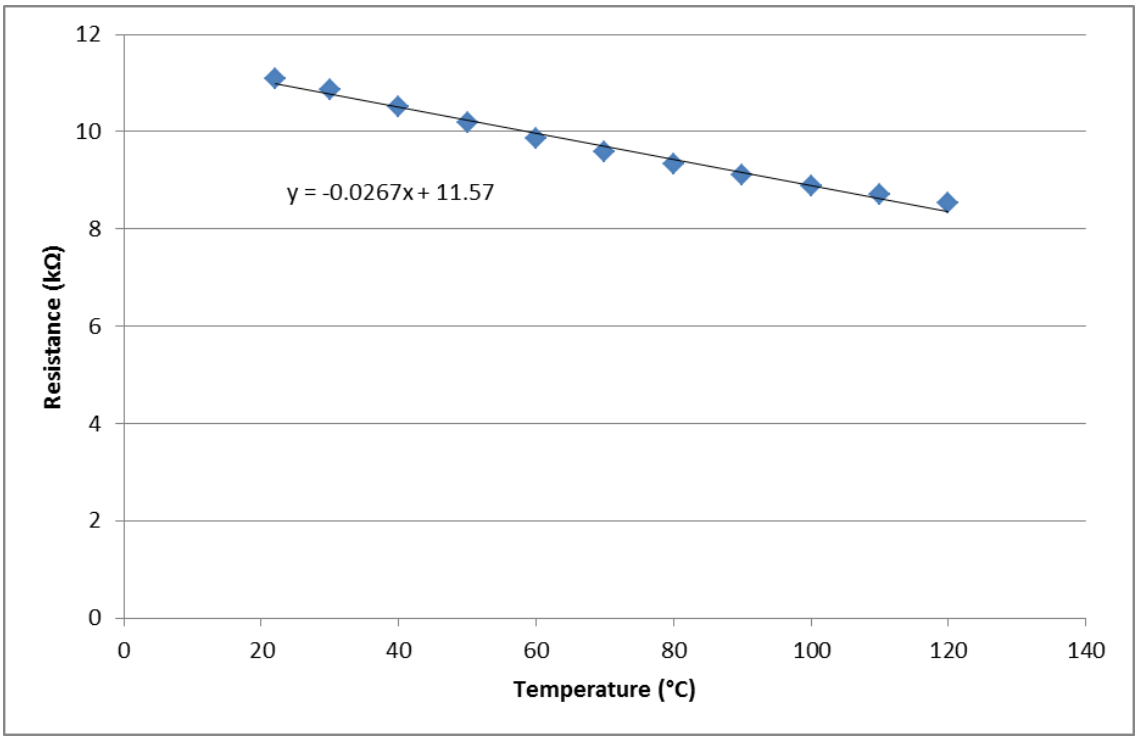

Figure 4.7: Temperature calibration for palladium sensor

After calculating the necessary voltage, the palladium sensor was connected to the experimental setup explained earlier. Once the 1.6 volts were applied to the circuit, it was observed that the palladium signal was not stable, and tended to drift with not meaningful pattern. Assuming that perhaps it was the microbridge not completely heating up to the required temperature, the sensor was left in the circuit with the applied 1.6 volts for a total of 4 hours, periodically introducing a certain concentration of hydrogen. The results of this test are shown in Figure 4.8. As can be seen there is a large change in resistance at around hour 13 to hour 13:18. Even though there was a large resistance change during this time interval, there was no actual change in the conditions of the experiment, that is no introduction of a target gas. The introduction of hydrogen was done around hour 14:35, starting at 0.5% hydrogen and going up to 2% hydrogen, alternating between hydrogen and pure nitrogen. A concentration of helium, around 10%, was later introduced to see if there would be a significant resistance change. This

was done around hour 14:58, with the introduction of pure nitrogen later in the test, with again no meaningful resistance change.

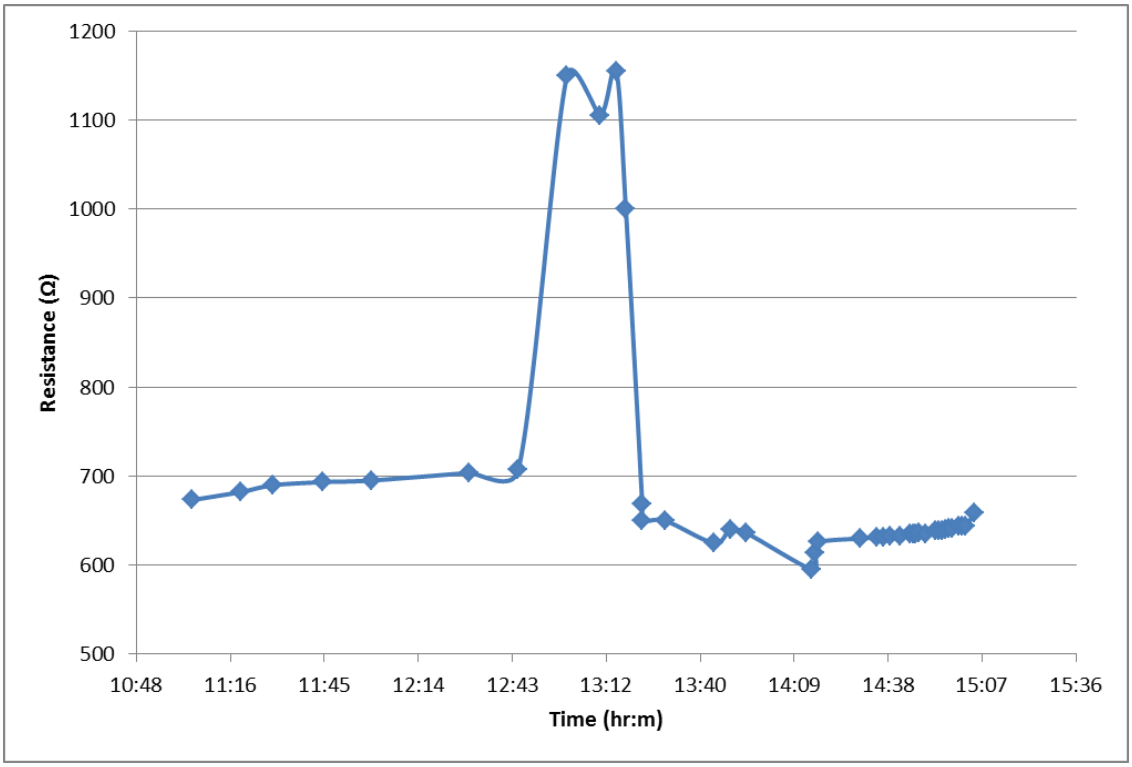

Figure 4.8: Stability test of palladium sensor at 1.6 volts

The setup was then changed, as was explained earlier, by disconnecting the power supply and moving the glass bottle into the oven. The oven temperature was brought up to 100°C in order to activate the palladium coating. The reading from the palladium film was observed to be steady, at which point the testing of hydrogen was commenced. Two different tests were conducted in order to show the selectivity of palladium to hydrogen. Figure 4.9a shows a comparison of resistance change of the palladium to different concentrations of pure helium as well as different concentrations of 5% hydrogen. Figure 4.9b shows a comparison of resistance change of palladium to different concentrations of methane as well as different concentrations of hydrogen. The sensitivity of the palladium coating to hydrogen at 100°C was found to be 0.18 mΩ/ppm.

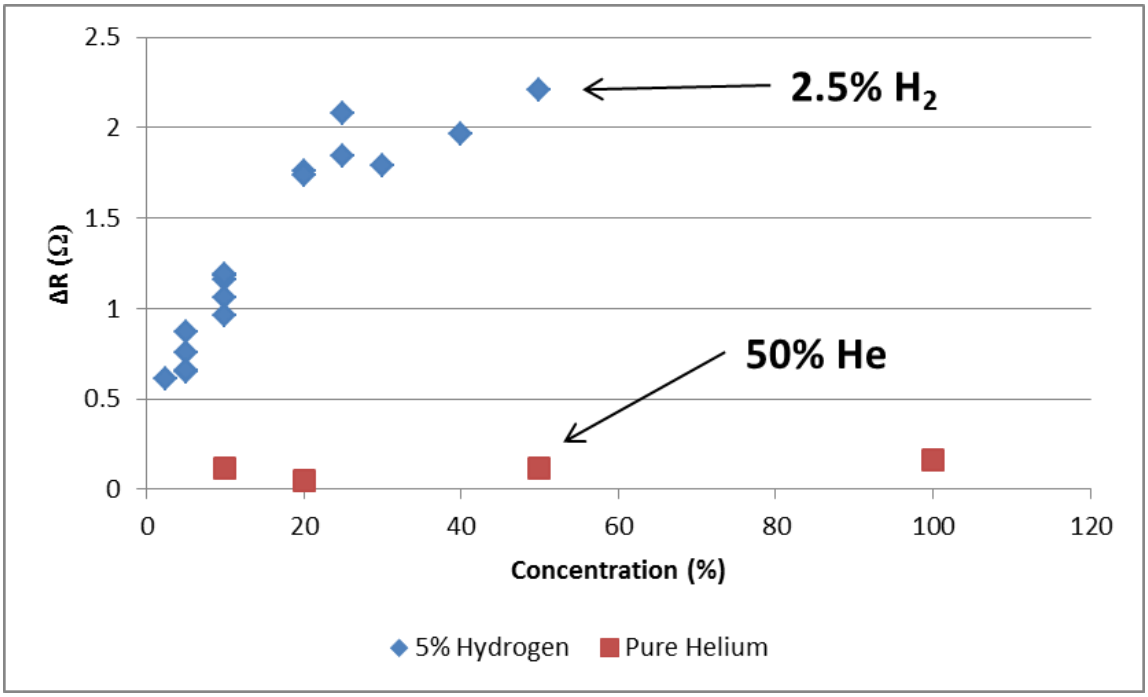

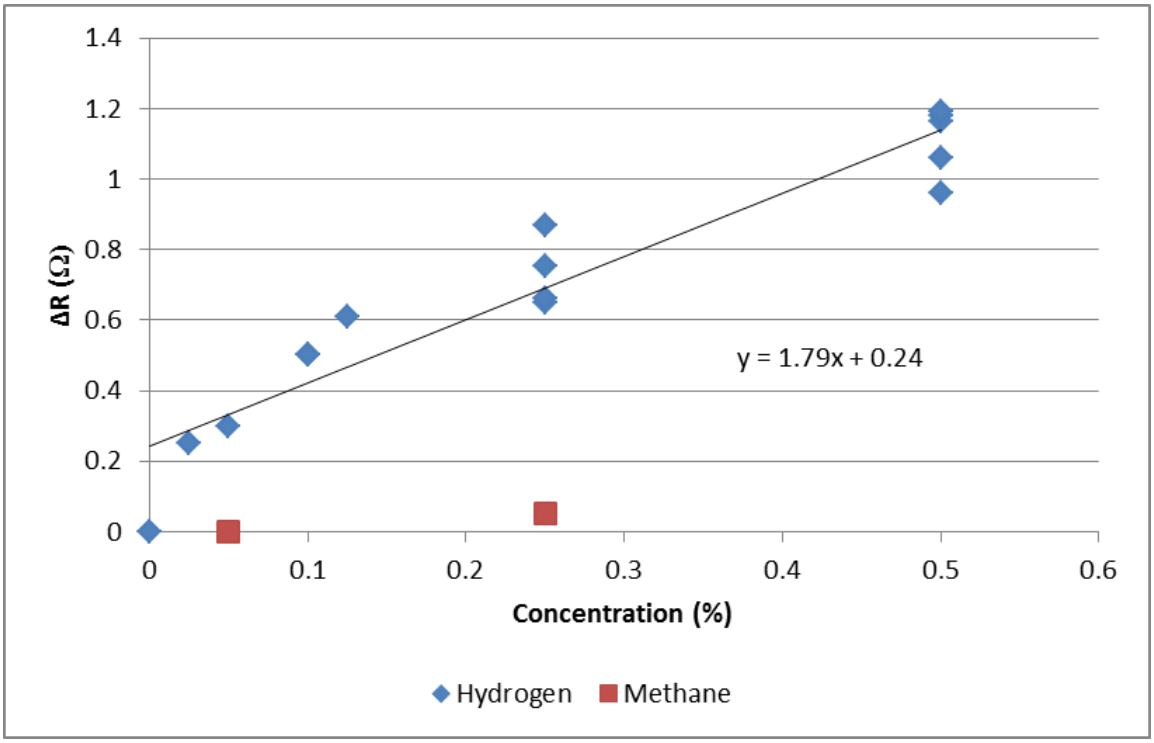

Figure 4.9: Resistance change vs. concentration for palladium sensor - a) 5% hydrogen and pure helium; b) Hydrogen and methane

4.2.4 Tin Oxide Coating Experiment Results

The fourth tests were run in order to characterize the tin oxide coating that was sputtered on the microbridges from the new design. The first part of these tests was the temperature calibration of the platinum runners on the microbridges. During the experiment, both the resistance of the platinum and the voltage drop across the resistor were measured and recorded. The voltage drop across the resistor was vital for the calculation of the current running through the circuit, and thus the power that was applied to the microbridge. The resistance of the platinum was then used to calculate the temperature of the bridge, given that the temperature coefficient of resistance for platinum is 0.00393 [31]. Figure 4.10a shows a plot of the resistance of the platinum versus the power that was applied to the microbridge. Figure 4.10b shows a plot of the resistance of the platinum versus the operating temperature.

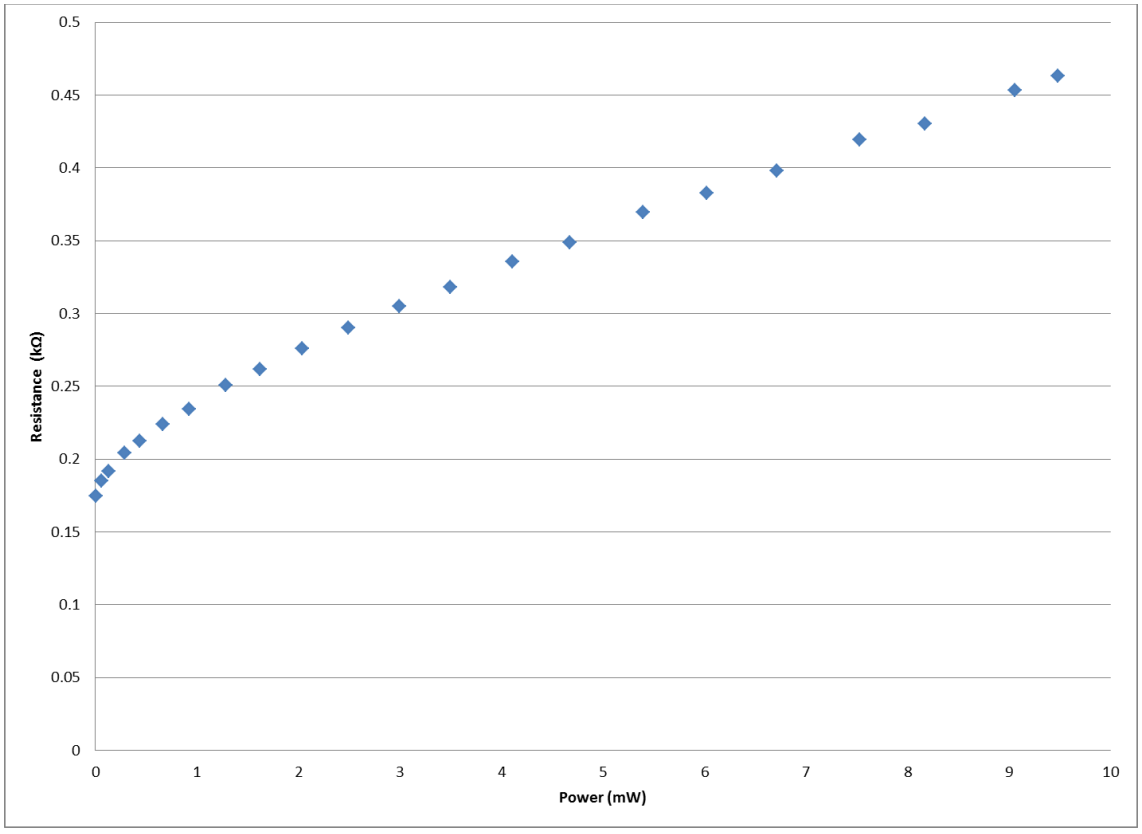

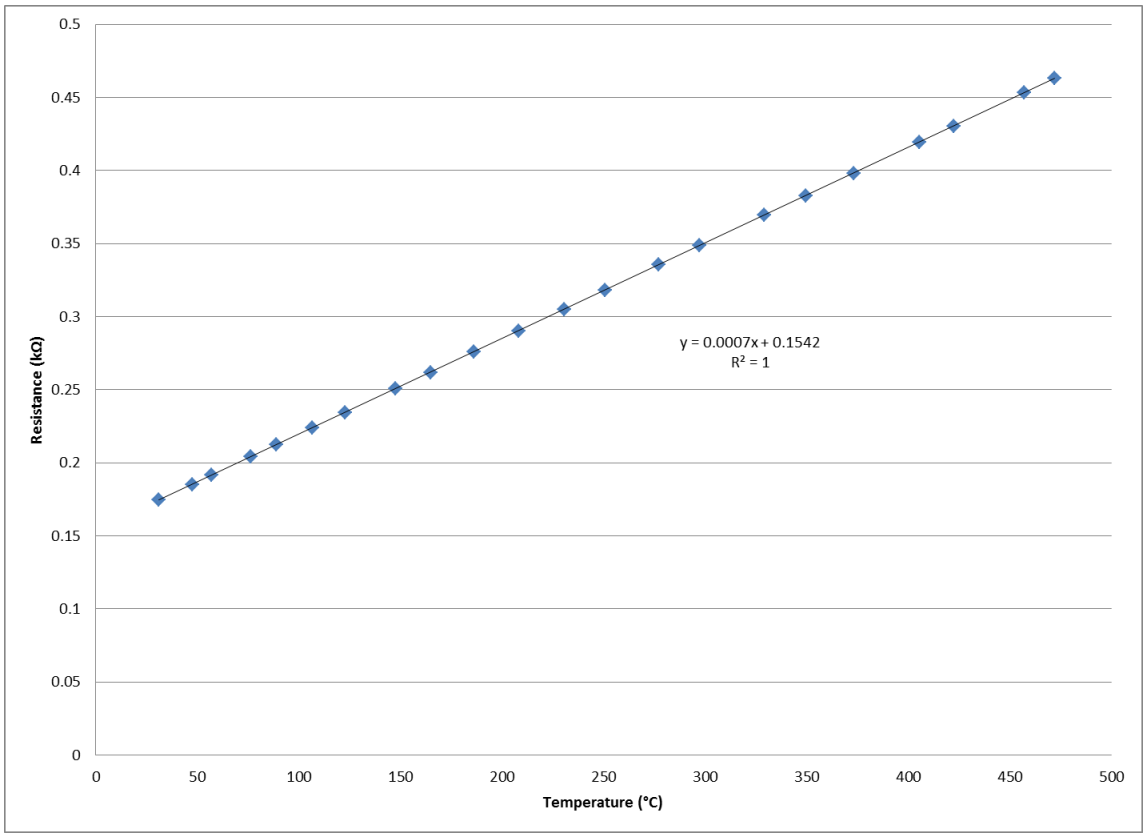

Figure 4.10: a) Platinum resistance vs. operating power; b) Platinum resistance vs. operating temperature

Even though three different microbridges were designed for metal coating testing, only one was experimented with which had the tin oxide coating on it. Die 4, which is the 50x1 µm, was the microbridge with tin oxide coating that was tested for methane sensing. In order to activate the tin oxide film, the microbridge had to be heated up to a temperature upwards of 400°C. This was achieved by heating the microbridge to a power level of 8.85 mW, at which point the flow of methane mixture was introduced into the chamber in which the sensor was found. The flow of mixture was kept constant throughout the experiments. The mixture in the chamber was changed every minute, starting with room air first, then the first concentration of methane, then room air again, and so forth. Figure 4.11 shows two graphs of the resistance change on the tin oxide film as the methane mixture changes. As can be seen from the Figure 4.11a, at 5% methane

mixture a resistance change of about 45 MΩ was observed. Also on the graph, it can be observed that at 3% methane, it is difficult to deduce whether the signal is response to methane or just noise from the instruments and/or the sensor. Figure 4.11b shows a similar trend as the first graph, denoting a resistance change of about 47 MΩ at 5% methane mixture. The 3% methane signal however is very poor, and as can be observed there is much more noise in the second graph.

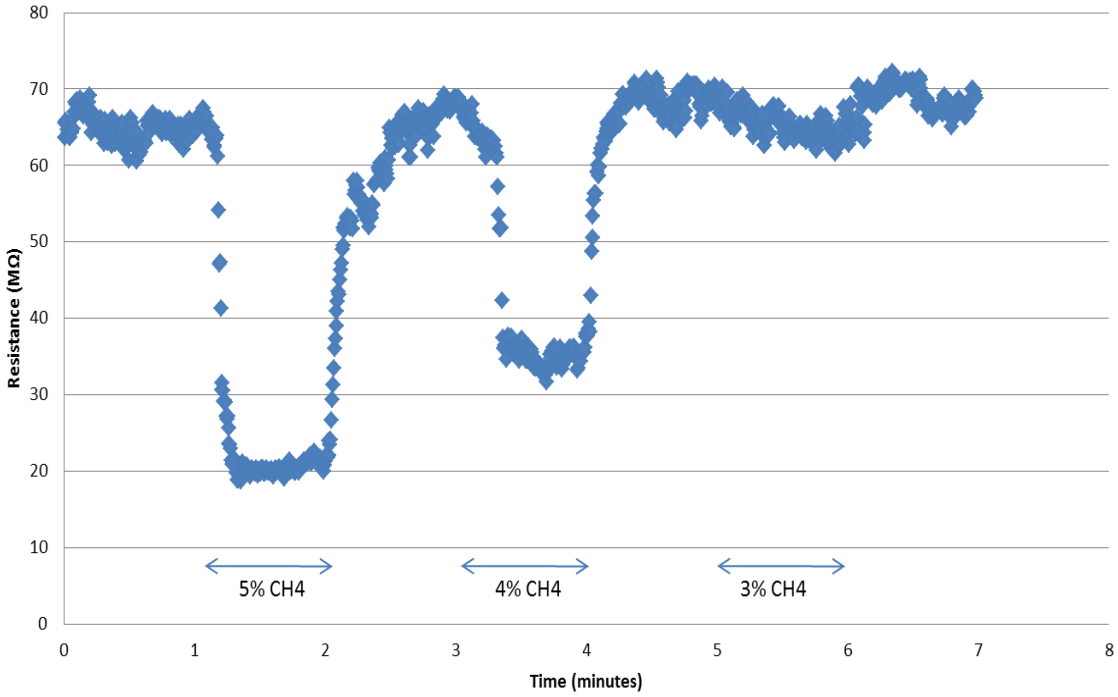

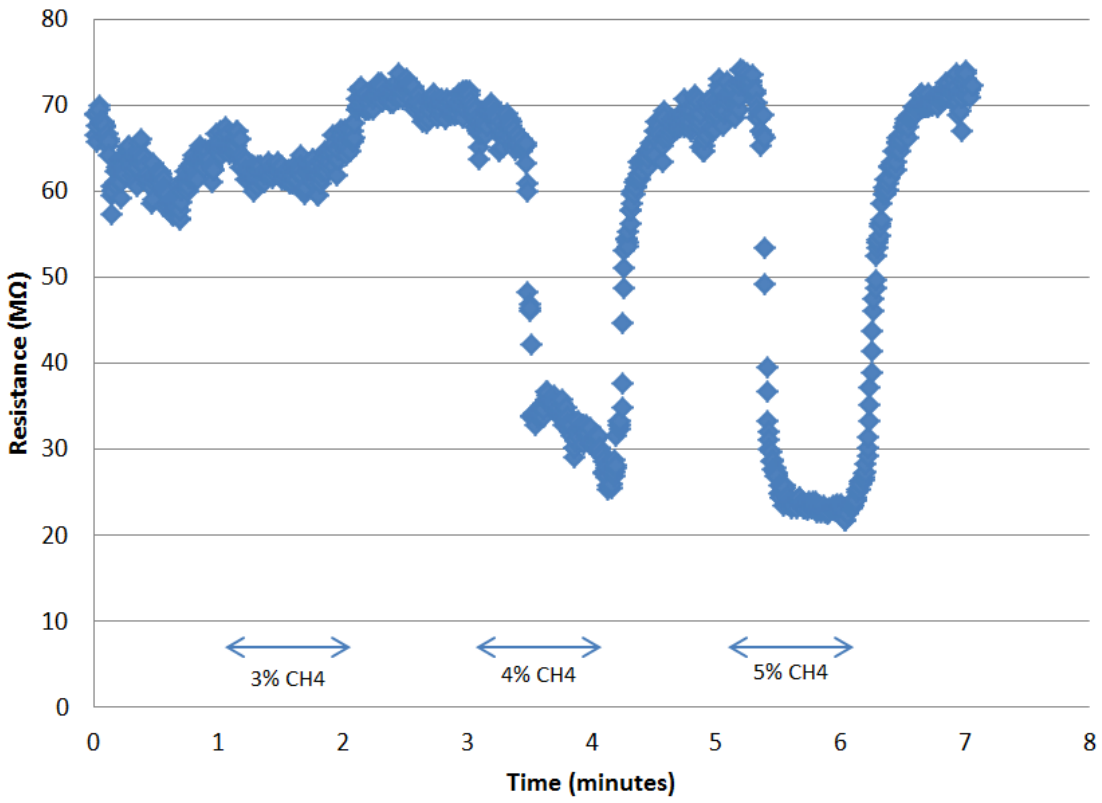

Figure 4.11: Tin oxide film resistance vs. change in methane mixture – a) Decreasing methane in mixture; b) Increasing methane in mixture

CHAPTER 5

DISCUSSION

This chapter will cover discussion of the experimental results, along with the juxtaposition of these same results with theory. Before discussing the results, it is important to expand on the theory behind thermal conductivity detectors initially explored in the first chapter of this Thesis. This will be followed by discussion of the various data sets obtained through the different experiments.

5.1 Thermal Conductivity

As was explained previously, the microbridge sensor, acting as a thermal conductivity detector, works on the concept of heat loss due to the presence of the target gas. The sensitivity of the TCD is characterized by its resistance change, and thus its temperature change, while a voltage is applied across it. Figure 5.1 shows the schematic, once again, of the heat loss in the microbridge TCD during operation.

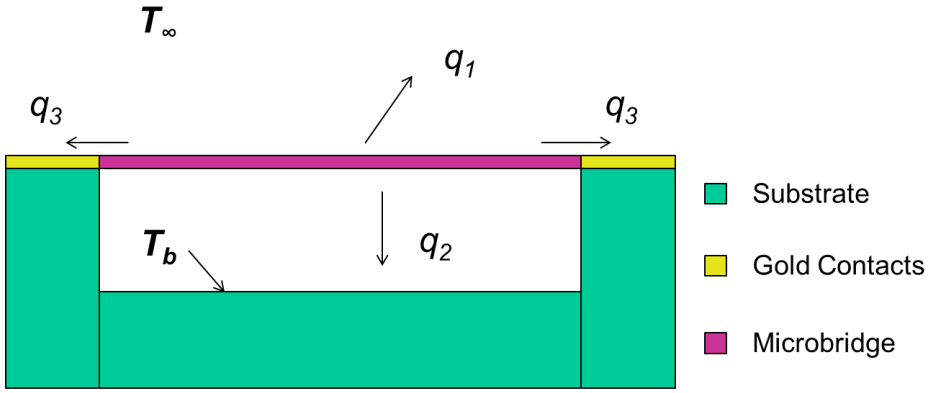

$$q_{tot} = \int q_1 + \int q_2 + 2q_3$$

Figure 5.1: General schematic of heat loss in the microbridge during operation

The schematic shows the different directions in which the heat from the microbridge is dissipated. The main source of heat loss is via conduction through the target gas. This can be seen from heat rate values q_1 and q_2. The heat loss through the substrate is the heat rate q_3. Thus this model shows in general the heat transfer behavior which arises once the sensor is activated and heated.

In order to further understand the mathematics behind the phenomenon in the microbridge TCD, certain assumptions need to be made. The following derivation holds true for the microbridge which has constant cross sectional area, and thus the temperature changes along the length of the microbridge. The first assumption is to treat the microbridge as a fin. Since the temperature distribution along the sensor is symmetrical, a good assumption is to look at only half of the microbridge, where one end is anchored to the substrate and has a constant temperature, while the other end is suspended and it is assumed to be adiabatic. In order for the following model to be valid, it is important to check that there is a uniform temperature field across the width and the thickness of the microbridge. To do so, the Biot is calculated for silicon in air using the following equation,

$$Biot = \frac{ht}{\lambda}$$

where h is the heat transfer coefficient of the ambient gas, t is the thickness (or width in this case) of the microbridge, and λ is the thermal conductivity of the polysilicon. Assuming a value of h = 25 W/m^{2}K for air due to natural convection, a value of λ = 149 W/mK for polysilicon, and t = 1 μm for both the width and the thickness of the microbridge, the Biot number is calculated as 1.678 x 10^{-7}, which is much less than 1. For this reason, the microbridge is taken to have a uniform temperature field across the thickness and the width.

The last assumption to be taken into account is neglect of radiation from the surface of the element. Now to model the microbridge as a fin, it is important to take

slice of the microbridge and applying the conservation of energy to it. Doing so leads to the following equation,

$$q_x + Q = q_{x+dx} + dq_{conv}$$

where q_x and q_{x+dx} are the conduction heat rates through the slice, dq_{conv} is the convection heat transfer rate, and Q is the heat generation rate in the silicon. These four terms can be expressed as the following,

$$q_x = -\lambda A_c \frac{dT}{dx}$$

$$q_{x+dx} = q_x + \frac{dq_x}{dx}dx = -\lambda A_c \frac{dT}{dx} - \lambda \frac{d}{dx}\left(A_c \frac{dT}{dx}\right)dx$$

$$dq_{conv} = hdA_s(T - T_\infty)$$

$$Q = q'''A_c dx$$

Where A_c is the cross sectional area, dA_s is the surface area of the differential slice, h is the heat transfer coefficient, λ is the thermal conductivity of the material, q''' is the volumetric heat generation rate, T is the temperature, and T_∞ is the ambient temperature. Substituting these expressions into the conservation of energy equation on the differential slice and simplifying gives the following,

$$\frac{d}{dx}\left(A_c \frac{dT}{dx}\right) + \frac{q'''A_c}{\lambda} - \frac{h}{\lambda}\frac{dA_c}{dx}(T - T_\infty) = 0$$

Even though this is general model for a fin, this is not the final model which describes the microbridge. First, the heat generation term is a function of location and a function of time, when a current is applied to the microbridge. This generated heat is dependent on the location on the microbridge because the resistance is a function of temperature. This holds true for the temperature variable and the heat transfer coefficient as well, since both of these are not constant along the length of the element. There are some assumptions that can simplify the model even further however. Since the cross sectional area is constant, the differential term $dA_c/dx = 0$. Additionally, the surface area can be expressed in terms of the perimeter of the microbridge, P, times the length, x.

This observation leads to the differential term $dA_s/dx = P$. With the incorporation of these assumptions, along with the addition of the heat generation due to the bias on the microbridge, the final model is obtained,

$$\frac{d^2T(x)}{dx^2} + \frac{q'''(x)}{\lambda_p} - \frac{Ph(x)}{\lambda_p A_c}(T(x) - T_\infty) = 0$$

The above equation is thus a model for the behavior of the microbridge TCD during operation, with the λ_p being the thermal conductivity of the polysilicon. Even though it is not directly apparent, the effect of the thermal conductivity of the gas is indeed included in the model, via the heat transfer coefficient. This term is dependent on the thermal conductivity of the gas, which in turn depends on the temperature of the gas. Since the microbridge temperature changes along its length, the thermal conductivity of the gas along this same length changes, thus changing the heat transfer coefficient with it. As can be seen, the above equation is a model for the steady state case. This was not always the case however during the experiments, in which a pulse was applied to the sensor, thus going from excitation to relaxation, and so on and so forth. Thus, the temperature profile along the microbridge not only changes with position but with time as well. An extra term is added to the model as well to account for this transient behavior. The following equation describes the transient model (C_p is the specific heat of the polysilicon),

$$\frac{d^2T(x,t)}{dx^2} + \frac{q'''(x,t)}{\lambda_p} - \frac{Ph(x,t)}{\lambda_p A_c}(T(x,t) - T_\infty) = C_p \frac{dT(x,t)}{dt}$$

Due to time constraints and lack of necessary equipment, the temperature function *T(x)* was not obtained. Thus both the steady state and the transient model were not completely solved. They do however explain the heat transfer behavior of the microbridge which allows it to act as a thermal conductivity gas sensor. This behavior was approximated through the use of a finite element analysis program though. Through the use of the FEA tool COMSOL, a quarter of a 50x1 μm microbridge was modeled. In

this model, the microbridge was assumed to be at steady state and the heat transfer coefficient was assumed to be constant. Figure 5.2 shows an image of the results of running the FEA model using the following parameters: silicon resistivity of $2x10^{-3}$ Ω-cm (value close to actual resistivity after doping), silicon thermal conductivity of 149 W/mK [32], and heat transfer coefficient of air of 25 W/m^2K [33]. The gas present was air, which was taken care of by denoting the heat transfer coefficient to be that of air, assuming free convection. Figure 5.2a shows the results for an applied voltage of 1 volt, while Figure 5.2b shows the results for an applied voltage of 2 volts. As is observed, the temperature does depend on the position along the microbridge length. Another meaningful result is the maximum temperature at which the microbridge goes up; for 1 volt, the maximum temperature is about 185°C, whereas for 2 volts the temperature is about 602°C. As is expected, the middle of the microbridge, or in the case of the FEA model the end of the fin, is at the maximum temperature during operation.

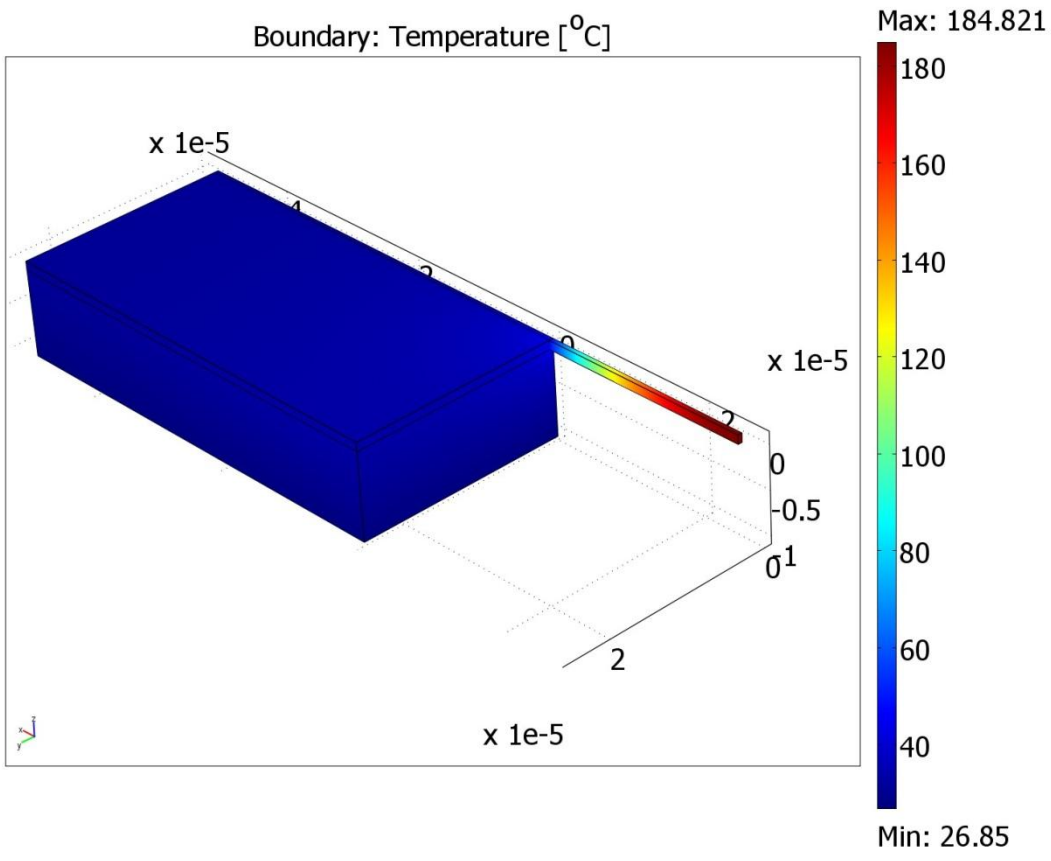

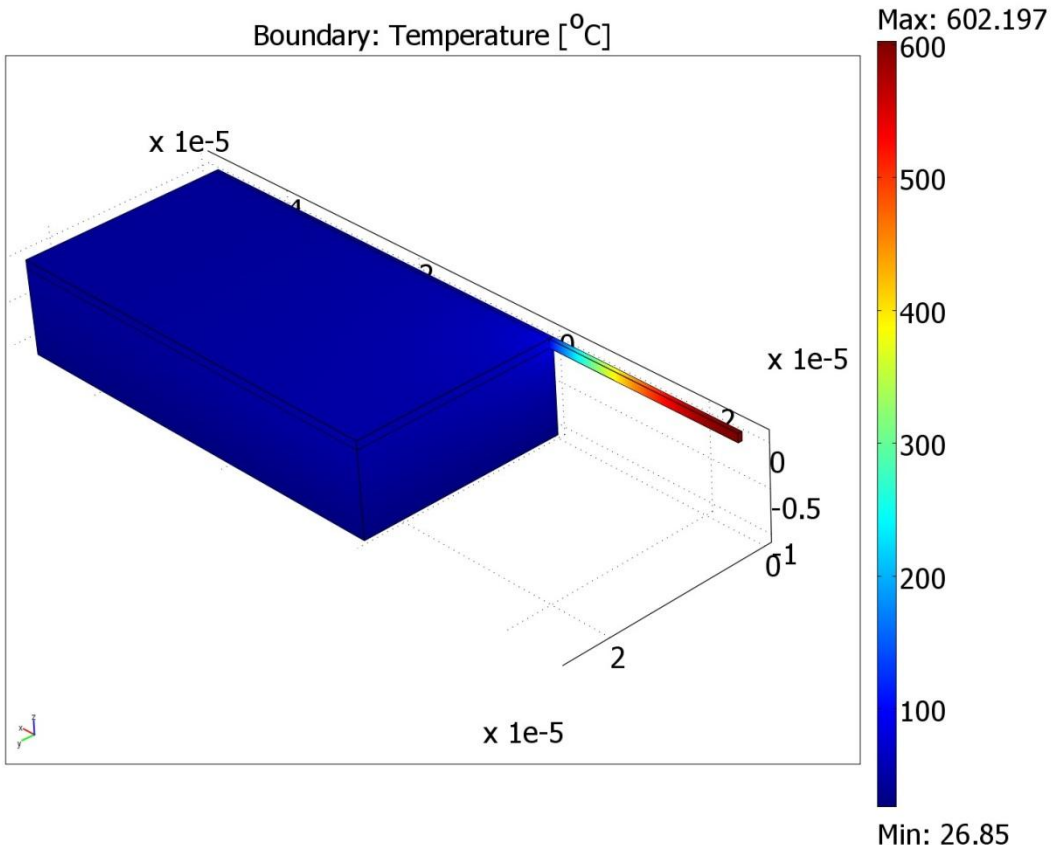

Figure 5.2: FEA model of quarter of a 50x1 µm microbridge – a) 1 volt; b) 2 volts

By looking at the governing equation which describes the behavior of the microbridge during operation, it can be seen that the thermal conductivity of the gas present plays a vital role in the overall heat loss. Thus the microbridge, acting as a TCD, can sense which gas is present, by applying a voltage to it and measuring the change in resistance, which is directly related to the temperature of the microbridge. This was shown in Chapter 3.3.3, where by conducting a temperature calibration on the sensor, it was observed that not only was there a positive relationship between the resistance and the temperature of the microbridge (that is, as the temperature increased, so did the resistance), but that it is not a simple linear relationship, but that instead it is much more complex and can be approximated with a cubic fit.

The results for the single gas experiment show that the largest change in resistance was observed with carbon dioxide, followed by nitrogen, and then followed by

helium which had the least change in resistance. Even looking at the gas mixture experiments, it is apparent that when more nitrogen was in the mixture the change in resistance was larger than when higher concentrations of either methane or helium were found in the mixture. By knowing the principle behind the TCD model, these findings suggest that the thermal conductivity values for nitrogen and carbon dioxide are in fact smaller than those of helium and methane. The lower the resistance change, the cooler the microbridge is during operation. This means that for the low resistance change cases, the gas has to have a high thermal conductivity value in order to increase the heat rate at the surface of the microbridge. This trend can be confirmed by looking at the thermal conductivity values for each of these gases, as shown in Table 5.1 [34].

Table 5.1: Table of the thermal conductivity of different gases at room temperature

Thermal conductivity of various gas at 293 K ($mW\,m^{-1}\,K^{-1}$)

Gas	λ
H_2	174
He	142
CH_4	30
O_2	24.7
N_2	24.3
CO	24.3
NH_3	21.8
CO_2	14.2
Cl_2	8.7

From the table, the thermal conductivity values for helium and methane are indeed higher than that of nitrogen and carbon dioxide. Helium specially has a much higher thermal conductivity value, which explains such low resistance change when compared to the other gases tested. Note that these thermal conductivity values are in fact at room temperature. As was explained before, the thermal conductivity of each gas changes depending on the temperature. This is observed in the single gas experiments in which the voltage was increased from 4 volts to 5 volts, in increments of 0.5 volts. The

resulting data shows that as the voltage applied was increased, so too did the resistance change increase for each of the tested gases. Increasing the voltage means increasing the temperature in the microbridge, and thus changing the thermal conductivity of the gas. This relationship between the thermal conductivity and the temperature is as follows,

$$\lambda = \lambda_0 \left(1 + k\left(\frac{T - T_0}{2}\right)\right)$$

where λ is the thermal conductivity at temperature T, λ_0 is the thermal conductivity of the gas at room temperature T_0, and k is the temperature coefficient.

Even in the gas mixture case, the thermal conductivity of the gases plays a vital role when it comes to the sensing behavior of the microbridge. The results from this experiment show that in general as less nitrogen is mixed into the gas mixture, the lower the resistance change measured. In a sense, it can be argued that the gas mixture has its own thermal conductivity and that depending on the concentrations of the gases present, the thermal conductivity of the gas mixture changes accordingly. By looking at the data, it can be inferred as well that the thermal conductivity of the mixture not only is dependent on the concentrations of each gas, but on the thermal conductivity of each individual gas as well, and that these in turn are dependent somehow to the corresponding concentration. Pascal Tardy not only made the same argument in his paper [34], but also presented an expression which combined these observations in one. The thermal conductivity of the mixture can be obtained using the following expression,

$$\lambda_{mix} = \lambda_1 \left(1 + G_{12}\frac{x_2}{1 - x_2}\right)^{-1} + \lambda_2 \left(1 + G_{21}\frac{1 - x_2}{x_2}\right)^{-1}$$

where λ_1 is the thermal conductivity of the first gas, λ_2 is the thermal conductivity of the second gas, x_2 is the molar fraction of the second gas, and the G terms are as follows,

$$G_{12} = \frac{1.065}{2\sqrt{2}}\left(1 + \frac{M_1}{M_2}\right)^{-1/2}\left(1 + \sqrt{\frac{\mu_1}{\mu_2}\left(\frac{M_2}{M_1}\right)}^{1/4}\right)^2$$

$$G_{21} = \frac{1.065}{2\sqrt{2}}\left(1 + \frac{M_2}{M_1}\right)^{-1/2}\left(1 + \sqrt{\frac{\mu_2}{\mu_1}\left(\frac{M_1}{M_2}\right)}^{1/4}\right)^2$$

where M_1 and M_2 are the corresponding molar masses, while μ_1 and μ_2 are the corresponding viscosities for each of the gases. The above equations show the effects of the concentration as well as the thermal conductivity of each gas in the mixture on the overall mixture thermal conductivity. Since the viscosity and the molar mass of each of the gases are constant, it is possible to plug in different concentrations in order to calculate the mixture thermal conductivity. Table 5.2 shows the values for the terms necessary to solve the above equations for the mixture thermal conductivity, all at room temperature [35] [36]. Table 5.3 shows the values of the mixture thermal conductivity at different concentrations for mixtures of nitrogen/helium and nitrogen/methane. For both of these tables, the temperature is assumed to be room temperature.

Table 5.2: Molar mass, viscosity, and thermal conductivity at room temperature

Gas	Molar Mass M (g/mol)	Viscosity μ (Pa-s)	Thermal Conductivity λ (W/mk)
Nitrogen, N_2	28.02	1.79×10^{-5}	0.024
Methane, CH_4	16.04	1.12×10^{-5}	0.030
Helium, He	4.002	2×10^{-5}	0.142

Table 5.3: Mixture thermal conductivity values at room temperature

N_2 Concentration (%)	He Concentration (%)	$\lambda_{N2\text{-}He}$ (W/mK)	CH_4 Concentration (%)	$\lambda_{N2\text{-}CH4}$ (W/mK)
0	100	0.142	100	0.030
20	80	0.1063	80	0.0282
40	60	0.0786	60	0.0268
60	40	0.0566	40	0.0257
80	20	0.0387	20	0.247
100	0	0.024	0	0.024

As Table 5.3 shows, the mixture thermal conductivity is heavily dependent on the thermal conductivity of the individual gases present. The results from the gas mixture tests follow this same trend. For the nitrogen/helium mixture shown in 3.9, the resistance change of the mixture as a function of concentration is significant, with a negative slope. This follows theory since as the concentration of helium goes up, the mixture thermal conductivity increases also, which as has been shown earlier, decreases the overall resistance change. The same holds true for the nitrogen/methane experiment, as can be seen in Figure 3.10. This mixture however has a lesser slope, meaning that the resistance change does decrease as a function of methane concentration, but does not decrease a significant amount. Again, this follows the trend that is observed in Table 5.3, given that the thermal conductivity of pure methane gas is much lower than that of helium.

5.2 Time Response

The time response experiments were conducted in order to find the speed at which sensors could sense the target gas. For any kind of gas sensor, the time it takes for it to go from idle to target gas sensing is very important, especially when the target gas is

hazardous. Thus low time constants are always desirable in the gas sensing industry. For the sensors tested for this Thesis, the time constant was obtained by first gathering the time response data. From this data it was possible to calculate the time constant of the sensor, that is the time that it takes for the sensor to reach 63% of its full signal. The equation used to calculate the time constant is as follows,

$$R = \Delta R\left(1 - e^{-t/\tau}\right) + R_0$$

$$\Delta R = R_{sat} - R_0$$

which after rearranging,

$$-\ln\left(\frac{R - R_{sat}}{R_{sat} - R_0}\right) = \left(\frac{1}{\tau}\right)t$$

where R is the resistance of the sensor over the duration of the time response graph, R_0 is the baseline resistance of the sensor during no operation, R_{sat} is the resistance of the sensor when the power is on, t is the time, and τ is the time constant. The value for $1/\tau$ was found by applying the above equation to the data. Figure 5.3 shows a typical graph of $1/\tau$. Plotting a fit line on the data and taking the inverse of the slope gives the time constant for the sensor. As can be seen in Table 4.1, all three sensors show a faster response time when the gas present is helium, while showing a significant increase in response time when in the presence of nitrogen. This is caused by the difference in thermal diffusivity between helium and nitrogen, where helium's thermal diffusivity is $1.9\text{x}10^{-4}$ m^2/s and nitrogen's thermal diffusivity is $2.2\text{x}10^{-5}$ m^2/s [37]. Since helium has the higher thermal diffusivity value, about a magnitude larger than that of nitrogen, the heat generated in the microbridge moves much more rapidly through it, which explains the faster response in helium than in nitrogen. As the power is increased, there does not seem to be a trend across all sensors. There is however a significant change in response time when comparing Die 3 to the rest of the sensors. Die 3 exhibits a much quicker response time than the others when compared within the same parameters. The reason behind the faster response time lies in the size of the microbridge. Since this microbridge

is half the size of Die 2, its surface area is much smaller. This means less heated surface area which is cooled down by the gas present. Thus during operation, the Die 3 sensor is able to reach its steady state much quicker than the other two sensors. This phenomenon is magnified when the target gas is that of helium, since it has such a high thermal diffusivity than other gases. The sensitivity of all three dies does seem to be the same however, as the time constant in helium is roughly about a fourth of the time constant in nitrogen for all three dies.

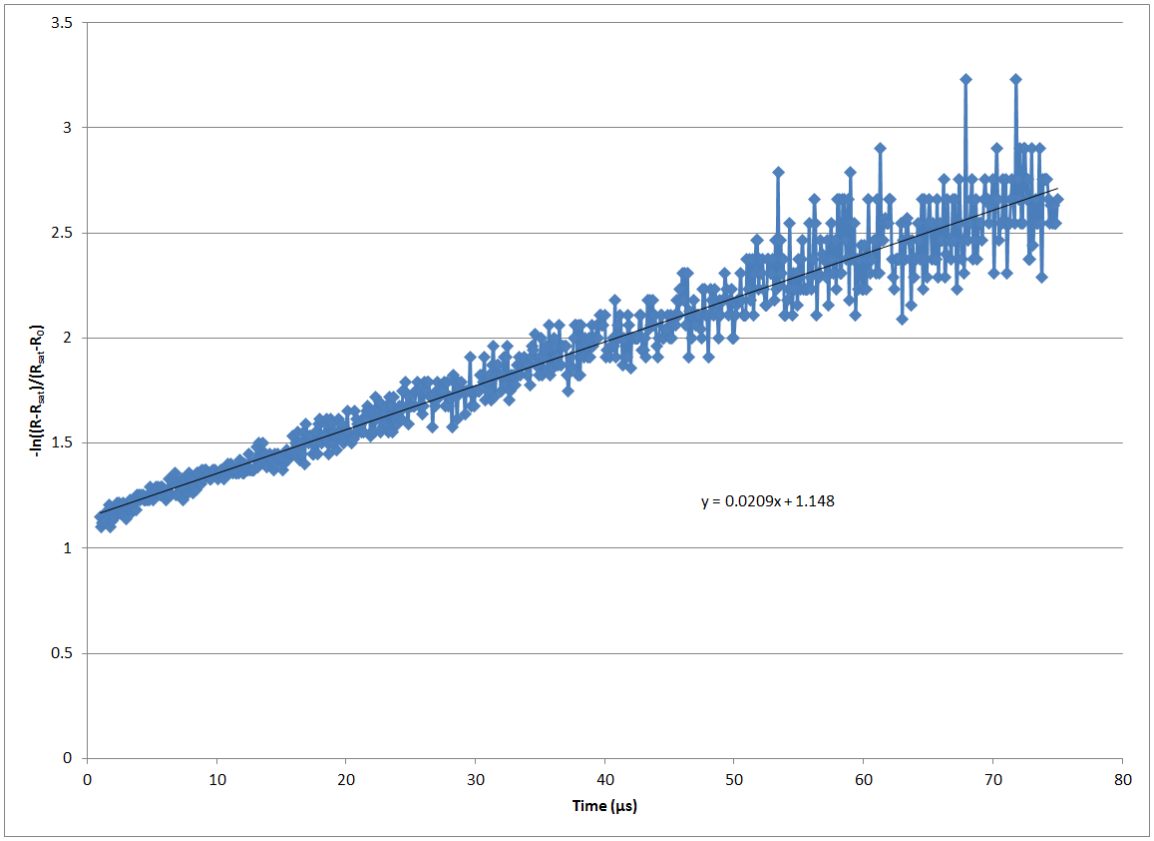

Figure 5.3: Plot of $1/\tau$ for a 50x1 µm, 25x0.5 µm microbridge in nitrogen at 3 mW

5.3 Response from Metal Coatings

Two different coatings were utilized and tested on the new sensor. These two were the metal palladium and the metal oxide tin oxide. For these experiments, the sensor did not behave as a TCD, that is following the model explored earlier. Instead, the microbridge acted as a heater, which activated the coatings on top of it. This activation

allowed for the coating to have sensing capabilities. In essence, instead of using the mechanical feature of heat transfer via conduction in order to sense the target gas, these metal coatings react with the gas chemically, allowing for absorption and desorption of the gas, and thus returning the sensor to its original state after operation [38]. Only certain gases react chemically with either of these metals, as was shown in Chapter 4 of this Thesis. This characteristic allows for selective sensing; in other words, by choosing the appropriate metal coating, it is possible to make a sensor that is only sensitive to the gas in question.

The new design provided for dies which had the capability for the use of metal coatings as the sensing element. These had extra platinum runners which ran on top of the microbridge, and were covered with either palladium or tin oxide. An example of one of these sensors can be seen in Figure 2.12, which shows an SEM image of a 50x1 μm microbridge coated with palladium, which is typical for both palladium and tin oxide sensors. The goal here was to show that these sensors, once coated, would be able to selective sense hydrogen or methane, respectively. As the results show, this was achieved during the preliminary experiments. In these tests, the metal had to be heated to a certain temperature which would allow for the chemical reaction between it and the gas to materialize. It was found that for a 60 nm palladium film to activate and be able to sense hydrogen, a temperature of around 100°C was required. The goal was to be able to use the microbridge as the heater for the palladium, but this was not achieved during experimentation. As was shown earlier, while applying a voltage to the microbridge and increasing its temperature, the resistance of the palladium did not stay stable, but instead drifted in a random manner. This was the reasoning behind using the oven as the heating source. Ultimately the goal was to show that the palladium coating did indeed work, being able to selective sense hydrogen. Not only was it able to sense hydrogen, it did not show any type of resistance change when other gases were introduced, thus showing selectivity to hydrogen.

For tin oxide, the use of the microbridge as a heater was a success. During the experiments, it was observed that the tin oxide coating of thickness of 250 nm did not show any resistance reading at low power levels. This meant that either the resistance was too high for the DVM to pick up and record, or that the coating was still not hot enough to be activated and allow for the necessary chemical reaction with the target gas. At a power level of around 5.2 mW however, a reading was observed for the tin oxide of around 200 MΩ. At this point, the power was increased in order to further reduce the observed tin oxide resistance. The signal of the tin oxide became unstable if the voltage applied to the microbridge was too high, which meant the temperature was too high, meaning that the thermal stresses at this temperature might cause parts of the film to delaminate from the microbridge and thus introduce the unstable resistance values which were observed. The bias was then adjusted so that the tin oxide signal could be stabilized. The voltage that was reached by doing this was that of 7 volts, in other words a power level of around 8.85 mW.

In order to find the operating temperature of the tin oxide it was necessary to understand the behavior of the platinum's inherent resistance and how it changes as the temperature is increased. To do so, a test was run similar to the tin oxide test, except that for this case a microbridge with a full platinum runner was chosen as was shown in Figure 4.5, and thus the resistance of the platinum was recorded as a function of the power. With this data, it was possible to calculate the temperature of the platinum at each given power level. To do so, the following equation was used,

$$R = R_{ref}\left(1 + \alpha\left(T - T_{ref}\right)\right)$$

which after rearranging,

$$T = \frac{R - R_{ref} + \alpha R_{ref} T_{ref}}{\alpha R_{ref}}$$

where T is the temperature of the platinum, R is the resistance of the platinum, R_{ref} is the resistance of the platinum at the reference temperature, T_{ref} is the reference temperature

which in this case is room temperature, and α which is the platinum temperature coefficient of resistance, which is α = 0.00393 [31]. Figure 5.4 shows the plot of the calculated temperature of the platinum versus the power input.

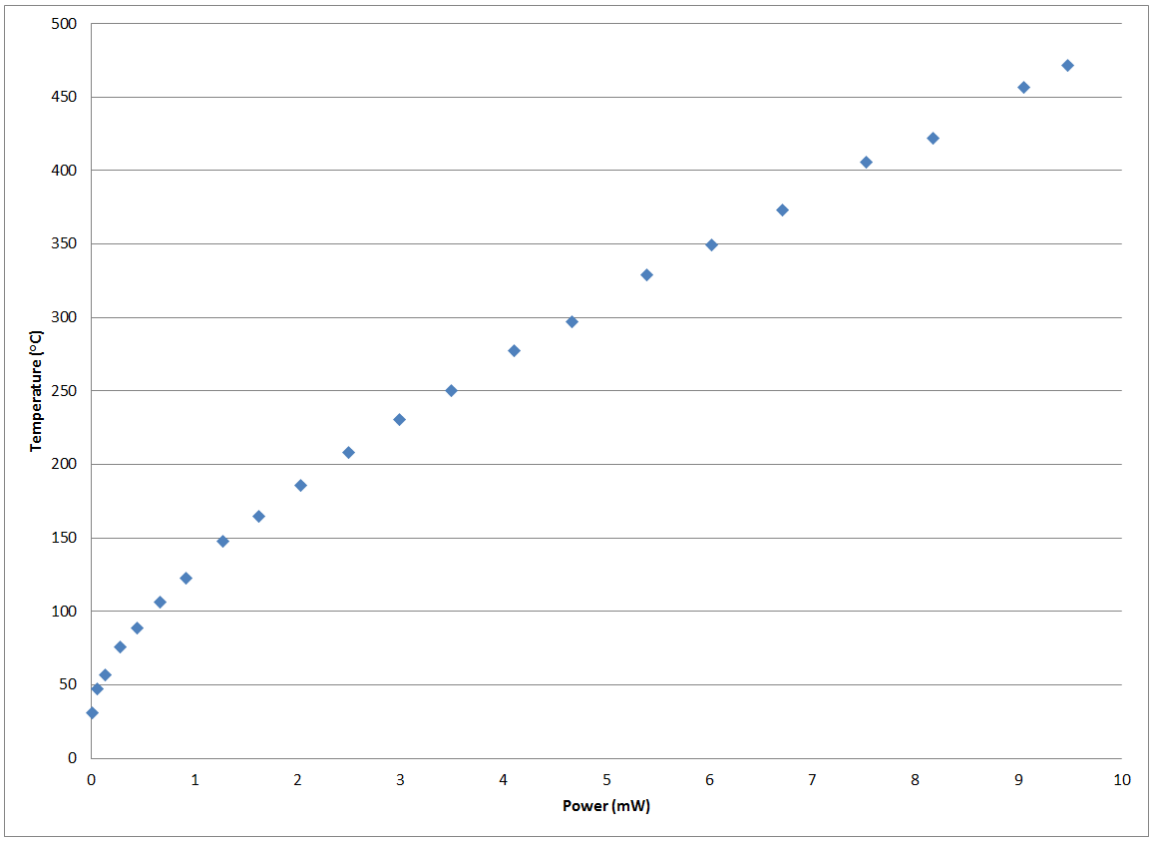

Figure 5.4: Platinum temperature vs. power input

From the plot, it was deduced that the temperature at which the data acquisition occurred was at about 450°C. The power input to the microbridge of 8.85 mW is equivalent to said temperature. That means that the microbridge heated up to 450°C, which in turn heated up the platinum and thus the tin oxide to that temperature. At this temperature, the data was collected and plotted, showing the sensing abilities and selectivity of the tin oxide coating on the microbridge. According to Chakraborty's paper [39], the operating temperature for the tin oxide to have its optimal methane sensing ability is at 350°C, with lower sensitivity at higher temperatures. A power of about 6 mW is needed to reach this temperature on this sensor; however this is not an ideal power

level for detection as was discussed earlier. This could be due to the nonuniform temperature on the microbridge, so that only a portion of the film is at a sufficiently high temperature. Even though the temperatures do not coincide, the sensor still senses and shows selectivity to methane.

5.4 Alternative Model

There is another model which could describe the sensing mechanics of the microbridge. This model assumes that the microbridge is at a uniform temperature. This is not the case however, as was suggested in the above COMSOL model, for the microbridge with a constant cross sectional area. For the microbridge which has a smaller center than the rest of the element, the assumption of uniform temperature could work for the center section, since this is the section which will generate the high temperatures. It is because of this observation that the following model is being explored. Once again, the model starts by looking at Figure 5.1; this time however, the individual heat rates are described. For conduction from the top of the microbridge into the ambient gas, the value for q_1 is as follows,

$$q_1 = \frac{q^*_{ss} \lambda_g A_s \left(T(x) - T_\infty\right)}{L_c}$$

where λ_g is the thermal conductivity of the gas, A_s is the active area, L_c is the characteristic length, $T(x)$ is the temperature function along the microbridge, T_∞ is the temperature of the ambient gas, and q^*_{ss} is the dimensionless conduction heat rate. The equations for the active area and the characteristic length are as follows,

$$A_s = 2wL$$

$$L_c = \sqrt{\frac{A_s}{4\pi}}$$

where w is the width of the microbridge and L is the length of the microbridge. The expression for q_1 assumes that the microbridge acts as an infinitely thin rectangle in an

infinite medium; this gives the above expression for A_s, as well as a value for q^*_{ss} of 0.932. The heat rate from the top of the microbridge is integrated across the length of the microbridge due to the temperature changing along the length of it. This is the reason for the function *T(x)* in the heat rate equation. The model for the heat rate from the microbridge also includes the heat loss from the microbridge due to conduction through the gas into the substrate. The value for this heat loss q_2 is as follows,

$$q_2 = S\lambda_g\left(T(x) - T_b\right)$$

where *S* is the shape factor for the given case, λ_g is the thermal conductivity of the gas, *T(x)* is the temperature function along the microbridge, and T_b is the temperature of the substrate. The expression for q_2 assumes that the microbridge is a horizontal isothermal cylinder, which is buried in a semi-infinite medium at a specified amount *z* from the surface. In the case of the microbridge, the medium is assumed to be the target gas, while *z* is the distance from the microbridge to the substrate. Given these assumptions, the value for the shape factor *S* is as follows,

$$S = \frac{2\pi L}{\cosh^{-1}\left(\frac{2z}{t}\right)}$$

where *L* is the length of the microbridge, *z* is the distance from the microbridge to the substrate, and *t* is the thickness of the microbridge.

There is also heat loss through the actual runners which connect to the bridge and into the substrate, portrayed as q_3 in the schematic. This heat loss is small however when compared to the heat loss due to the thermal conductivity of the gas. The equation for the value of q_3 is as follows,

$$q_3 = -kA_c \left.\frac{dT}{dx}\right|_{x=0}$$

where λ_p is the thermal conductivity of the microbridge, A_c is the cross sectional area, and the *dT* term is the differential change of the temperature at the point *x = 0*, that is at the

point where the microbridge meets the substrate. This model holds true for the both sides on which the microbridge ends and the substrate begins, thus the reason for the doubling of this term for the expression of the overall heat rate from the TCD. Both the main model and the alternative model were derived using the book Fundamentals of Heat and Mass Transfer by Incropera *et al* [40].

CHAPTER 6

CONCLUDING REMARKS

Surface micromachined polysilicon microbridges were designed, fabricated, and tested for use as electrothermal gas sensors. Six different designs were successfully fabricated and produced mechanically stable and electrically functional devices that were used for gas composition measurements. The fabrication of these devices proved to be complex, due to the number of process steps that were needed, and the difficulty behind some of them. One of these, the double exposure step, was by far the most difficult and brought many obstacles with it that needed to be overcome for the success of the fabrication. By using techniques such as vacuum sealed containers and proper care of the wafers, the double exposure step was achieved, allowing for the small features to be written in the electron beam lithography system and, while using the same photoresist, using deep ultraviolet photolithography to expose the rest of the pattern with the larger features onto the resist. The fabrication process was indeed a success, allowing for the fabrication of the six different sensor designs.

The sensor responds to ambient gas very rapidly with different level of change in resistance for different gases, purely due to the difference in thermal conductivity of gases. At 5V, the sensor was observed to have a resistance change of about 500 Ω in nitrogen, and a resistance change of about 300 Ω in helium. The higher voltages yielded higher resistance changes for all of the gases tested. It was also observed that the smaller the sensor the higher the sensitivity. In the gas mixture testing, the sensitivity of the sensor at 5V operation voltage was found to be 2.05 mΩ/ppm with a limit of detection at 126 ppm for helium in nitrogen, whereas at 3.6V operation voltage, it was found to be 0.75 mΩ/ppm, with a limit of detection at 344 ppm for methane in nitrogen. Another aspect of the sensor is that it has very low power consumption. From the single gas tests

it was deduced that at 4 volts the power consumption was around 16.1 mJ for helium and 11.5 mJ for nitrogen. The sensor's sensitivity to temperature alone was observed by conducting a temperature calibration, which resulted in a cubic function. The sensor was found to be robust, by functioning for over a little less than two months of operation at frequency of 10 kHz, or 36 million pulses per hour; the sensor's lie was shown to be about 39 billion pulses. The response of the sensor was investigated and found to be heavily influenced by both the thermal diffusivity of the gas present and the size of the microbridge sensor. It was found that for the Die 3 sensor, the smallest sensor fabricated, the time constant was that of about 9 μs in helium while operating at a power of 2 mW. The versatility of the sensor was also shown by the use of palladium and tin oxide as sensing films, while the microbridge itself acted as a heater which activated the films. Palladium and tin oxide were chosen due to their selectivity to hydrogen and methane respectively. The sensitivity of the palladium coating to hydrogen at 100°C was found to be 0.18 mΩ/ppm. The tin oxide coating was shown to selectively sense methane; at an operating power of 8.85 mW, about 450°C, a resistance change of 45 MΩ was observed for a gas composition of 5% methane. The microbridge TCD sensor not only proved to be robust and versatile, it also is the smallest and fastest microbridge TCD sensor today.

Much can still be achieved and learned with these sensors, more specifically the new sensors. If time permitted, several more experiments would have been conducted. First would be to characterize the new sensors with the new dimensions which have not been fully tested yet. Another experiment would be to run a three component mixture to see if the sensors can work under such conditions. Yet another would be to finalize the characterization of the metal films which are acting as the sensing element, and perhaps test different metal films. These experiments are left as future work.

APPENDIX A

SUPPLEMENTAL DATA

Table A.1: Tools used in the fabrication of the microbridges

Tool	Manufacturer and Model	Use
Furnace	Tystar	Nitride and polysilicon deposition; p-type doping
Mask Aligner	Karl Suss MA6	Align mask designs, expose patterns onto photoresist
Electron Beam Lithography System	JEOL JBX-9300FS	Write microbridge patterns onto photoresist; used for the smallest features
Inductively Coupled Plasma	Plasma-Therm	Etch polysilicon using Bosch process
Reactive Ion Etching	Vision	Etch nitride
Electron Beam Evaporator	CVC	Deposition of gold, platinum, and palladium

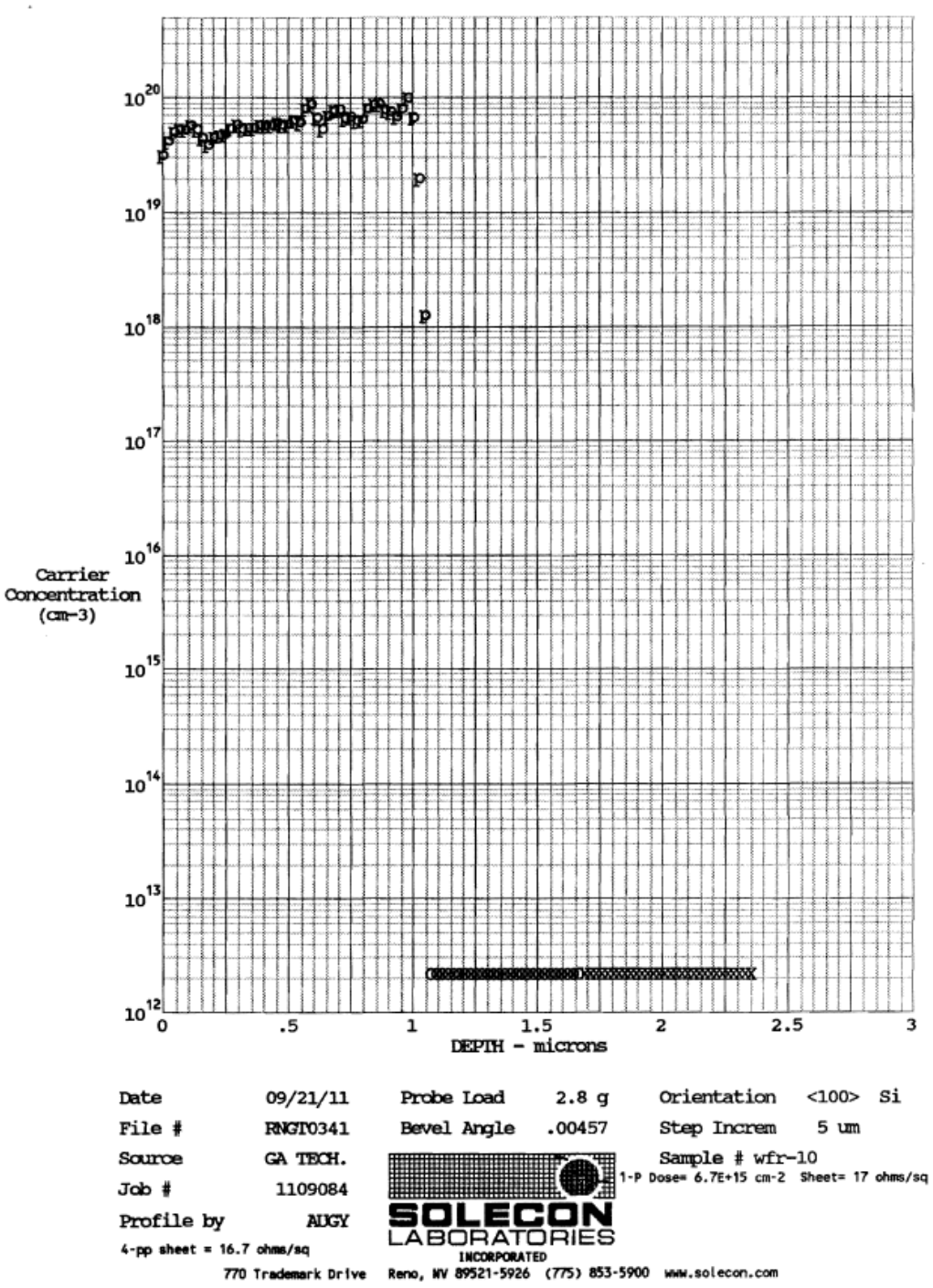

Figure A.1: Concentration of boron vs. depth into polysilicon layer

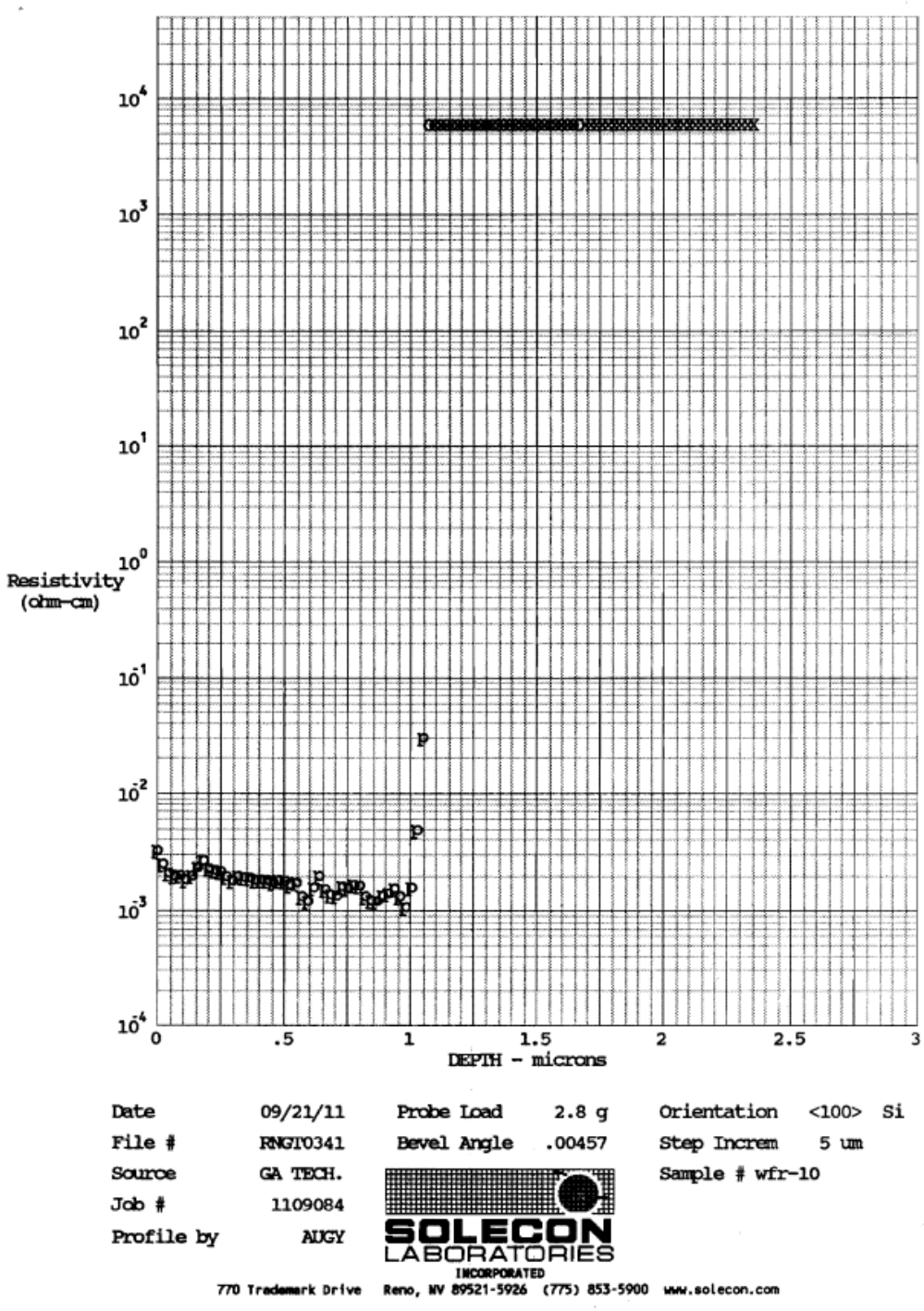

Figure A.2: Resistivity vs. depth into polysilicon film

REFERENCES

[1] E. Comini, G. Faglia and G. Sberveglieri, Solid State Gas Sensing, Springer, 2009.

[2] F. Ren and S. J. Pearton, Device-Based Sensors for Gas, Chemical, and Biomedical Applications, CRC Press, 2011.

[3] M. G. Jones and T. G. Nevell, "The Detection of Hydrogen Using Catalytic Flammable Gas Sensors," *Sensors and Actuators,* vol. 16, pp. 215-224, 1989.

[4] M. Engel, M. Baumbach, T. Kammerer and A. Schutze, "Preperation of Microstructured Pellistors and Their Application for Fast Fuel Vapor Discrimination," in *17th IEEE International Conference on MEMS*, 2004.

[5] C. Ducso, M. Adam, P. Furjes, M. Hirschfelder, S. Kulinyi and I. Barsony, "Explosion-proof monitoring of hydrocarbons by mechanically stabilised, integrable calorimetric microsensors," *Sensors and Actuators B,* vol. 95, pp. 189-194, 2003.

[6] M. Zanini, J. H. Visser, L. Rimai, R. E. Soltis, A. Kovalchuk, D. W. Hoffman, E. M. Logothetis, U. Bonne, L. Brewer, O. W. Bynum and M. A. Richard, "Fabrication and properties of a Si-based high-sensitivity microcalorimetric gas sensor," *Sensors and Actuators A,* vol. 48, pp. 187-192, 1995.

[7] J. Courbat, D. Briand, L. Yue, S. Raible and N. F. de Rooij, "Drop-coated metal-oxide gas sensor on polyimide foil with reduced power consumption for wireless applications," *Sensors and Actuators B: Chemical,* vol. 161, pp. 862-868, 2012.

[8] C.-W. Lin, H.-I. Chen, T.-Y. Chen, C.-C. Huang, C.-S. Hsu, R.-C. Liu and W.-C. Liu, "On an indium-tin-oxide thin film based ammonia gas sensor," *Sensors and Actuators B: Chemical,* vol. 160, pp. 1481-1484, 2011.

[9] A. Forleo, L. Francioso, S. Capone, F. Casino, P. Siciliano, O. K. Tan and H. Hui, "Fabrication at wafer level of miniaturized gas sensors based on SnO2 nanorods deposited by PECVD and gas sensing characteristics," *Sensors and Actuators B: Chemical,* vol. 154, pp. 283-287, 2011.

[10] B. Guo, A. Bermak, P. C. H. Chan and G.-Z. Yan, "A monolithic integrated 4 x 4 tin oxide gas sensor array with on-chip multiplexing and differential readout circuits," *Solid-State Electronics,* vol. 51, pp. 69-76, 2007.

[11] M. Watanabe, R. Inoue, D. Ichikawa and K. Furusaki, "Development of Thermal Conductivity Type Hydrogen Sensor," *ECS Transactions,* vol. 28, no. 20, pp. 31-42,

2010.

[12] R. P. Maginell, J. H. Smith, A. J. Ricoo, R. C. Hughes, D. J. Moreno and R. J. Huber, "Electro-thermal modeling of a microbridge gas sensor," in *Technical Digest of Solid-State Sensor and Actuator Workshop*, Hilton Head, SC, 1996.

[13] D. Cruz, J. P. Chang, S. K. Showalter, F. Gelbard, R. P. Manginell and M. G. Blain, "Microfabricated thermal conductivity detector for the micro-ChemLab," *Sensors and Actuators B,* vol. 121, pp. 414-422, 2007.

[14] D. Puente, J. Gracia and I. Ayerdi, "Thermal conductivity microsensor for determining the Methane Number of natural gas," *Sensors and Actuators B,* vol. 110, pp. 181-189, 2005.

[15] J. R. Stetter and e. al., "NanoTechnology-Enabled Sensing," Arlington, VA, 2009.

[16] J. R. Stetter, M. A. Ryan, A. V. Shevade, C. J. Taylor, M. L. Homer and M. Blanco, Computational Methods for Sensor Material Selection, Springer, 2010.

[17] T. Kawano, H. C. Chiamori, M. Suter, Q. Zhou, B. D. Sosnowchik and L. Lin, "An electrothermal carbon nanotube gas sensor," *Nano Letters,* vol. 7, no. 12, pp. 3686-3690, 2007.

[18] M. W. Ahn, K. S. Park, J. H. Heo, D. W. Kim, K. J. Choi and J. G. Park, "On-chip fabrication of ZnO-nanowire gas sensor with high gas sensitivity," *Sensors and Actuators B: Chemical,* vol. 138, no. 1, pp. 168-173, 2009.

[19] C. Yu, Q. Hao, S. Saha, L. Shi, X. Kong and Z. L. Wang, "Integration of Metal Oxide Nanobelts with Microsystems for Nerve Agent Detection," *Applied Physics Letters,* vol. 86, pp. 063101-3, 2005.

[20] G. Di Francia, B. Alfano and V. La Ferrara, "Conductometric Gas Nanosensors," *Journal of Sensors*, no. 659275, 2009.

[21] V. K. Jayatilaka and P. B. Espinasse, "MicroMagazine.com," PolarFab, [Online]. Available: http://www.micromagazine.com/archive/04/01/jayatilaka.html. [Accessed 2012].

[22] H. Rhee, H. Kwon, C.-K. Kim, H. Kim, J. Yoo and Y. W. Kim, "Comparison of deep silicon ething using SF6/C4F8 and SF6/C4F6 plasmas in the Bosch process," *Journal of Vacuum Science & Technology B,* vol. 26, no. 2, pp. 576-581, 2008.

[23] L. Palun and et al, "Fabrication of Single Electron Devices by hybrid (E-Beam/DUV) lithography," *Microelectronic Engineering,* vol. 53, pp. 167-170, 2000.

[24] R. Inanami, T. Nakasugi, S. Sato, S. Mimotogi, S. Tanaka and K. Sugihara, "Lithography Simulator for Electron Beam/Deep UV Intra-Level Mix & Match," *Japanese Journal of Applied Physics,* vol. 38, pp. 7035-7039, 1999.

[25] S. Landis, S. Pauliac, J. Saint-Pol, C. Gourgon, M. Akita, R. Hanawa and M. Suetsugu, "High-Resolution Hybrid Lithography with Negative Tone Chemically Amplified Resists," *Japanese Journal of Applied Physics,* vol. 43, pp. 3974-3980, 2004.

[26] L. Mollard, G. Cunge, S. Tedesco, B. Dal'zotto and J. Foucher, "HSQ hybrid lithography for 20 nm CMOS devices development," *Microelectronic Engineering,* Vols. 61-62, pp. 755-761, 2002.

[27] "ma-N 2400 — Negative Tone Photoresist Series," Micro Resist Technology, [Online]. Available: http://www.microresist.de/products/negative_photoresists/pdf/po_pi_man_2400_en_07062201_ls_neu.pdf. [Accessed 2011].

[28] VWR, [Online]. Available: https://us.vwr.com/store/catalog/product.jsp?catalog_number=36934-144. [Accessed 2012].

[29] Custom Sensor Solutions, Inc., [Online]. Available: http://www.customsensorsolutions.com/m1010.html. [Accessed 2012].

[30] Fluke Calibration, [Online]. Available: http://us.flukecal.com/products/data-acquisition-and-test-equipment/bench-multimeters/8845a8846a-65-digit-precision-multime?geoip=1. [Accessed 2012].

[31] "Resistivity, Conductivity and Temperature Coefficients for some Common Materials," The Engineering ToolBox, [Online]. Available: http://www.engineeringtoolbox.com/resistivity-conductivity-d_418.html. [Accessed 2012].

[32] "Thermal Conductivity: Silicon," Engineering Fundamentals, [Online]. Available: http://www.efunda.com/materials/elements/TC_Table.cfm?Element_ID=Si. [Accessed 2012].

[33] "Convective Heat Transfer," The Engineering ToolBox, [Online]. Available: http://www.engineeringtoolbox.com/convective-heat-transfer-d_430.html. [Accessed 2012].

[34] P. Tardy, J.-R. Coulon, C. Lucat and F. Menil, "Dynamic thermal conducitivity sensor for gas detection," *Sensors and Actuators B,* vol. 98, pp. 63-68, 2004.

[35] D. R. Lide, Ed., Handbook of Chemistry and Physics, 72nd ed., Boca Raton, Ann Arbor, Boston: CRC Press, 1992, pp. 6-154.

[36] "Thermal Conductivity of some common Materials and Gases," The Enginering ToolBox, [Online]. Available: http://www.engineeringtoolbox.com/thermal-conductivity-d_429.html. [Accessed 2012].

[37] R. Baierlein, Thermal Physics, Cambridge: Cambridge University Press, 1999, p. 372.

[38] B. L. Huy, S. Kumar and G.-H. Kim, "Manipulation of palladium nanoparticles in a 20 nm gap between electrodes for hydrogen sensor application," *Journal of Physics: Applied Physics*, vol. 44, pp. 1-5, 2011.

[39] S. Chakraborty, A. Sen and H. S. Maiti, "Selective detection of methane and butane by temperature modulation in iron doped tin oxide sensors," *Sensors and Actuators B*, vol. 115, pp. 610-613, 2006.

[40] F. P. Incropera, D. P. DeWitt, T. L. Bergman and A. S. Lavine, Fundamentals of Heat and Mass Transfer, 6th ed., John Wiley & Sons, Inc., 2007.